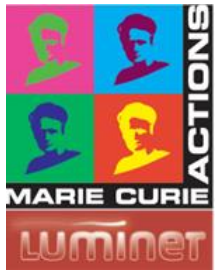

Universita' degli Studi di Verona

Department of Biotechnology

Graduate school of Natural Sciences and Engineering

Doctoral program in Nanoscience and Advanced Technologies

Cycle XXIX- year 2014

Fast emitting oxide scintillators and phosphors

S.S.D. CHIM/03

Coordinator: Prof. Franco Tagliaro

Tutor: Prof. Marco Bettinelli

Doctoral student: Irene Carrasco Ruiz

A mis padres

"Ultraviolet excitation compares to striking one key of the piano, cathode-ray or X-ray excitation compares to throwing the piano down the stairs."

H.A. Klasens

Summary

In this thesis, various luminescent materials have been prepared and their structural and spectroscopic characterization has been performed in order to test their possible application as phosphors and/or scintillators. The samples under study were oxide-based polycrystalline materials (silicates and phosphates) doped with different lanthanide ions.

The luminescence properties of Tb^{3+} and Eu^{3+} at room temperature and their evolution in the 8-330 K range have been studied in various Tb-based silicates with silico-carnotite-type structure. In the case of $Ca_3Tb_{2-x}Eu_xSi_3O_{12}$, efficient Tb^{3+}-Eu^{3+} energy transfer has been observed upon UV excitation. Fast energy migration among Tb^{3+} ions has been found in $Ca_3Tb_2Si_3O_{12}$ and $Ca_3Tb_{2-x}Eu_xSi_3O_{12}$. A different series of silico-carnotite-type compounds has been also studied at room temperature. In this case, samples were Gd- and Y-based materials co-doped with Tb^{3+} and Eu^{3+}. The resulting emission colour of these systems can be modified by controlling the Tb^{3+}/Eu^{3+} concentration ratio, leading to close-to-white emission in some of the analysed samples.

The effect of the structural changes of the host lattice on the luminescence of Pr^{3+} has been analysed in two families of phosphates. For the $Ca_9M(PO_4)_7$ (M = Al, Lu) powders it has been found that the optical properties of the Pr^{3+} 4f→4f transitions are quite insensitive to the nature of the M cation, but depend strongly on the dopant content: at high Pr^{3+} concentration the emission from the $^1D_2$ level is quenched due to the presence of cross relaxation processes, whereas no evident changes were observed in the transitions originated in the $^3P_0$ level. In the case of $K_3Lu_{1-x}Y_x(PO_4)_2:Pr^{3+}$ samples, it has been found that the emission upon UV excitation is dominated by the 5d→4f intraconfigurational transitions of Pr^{3+}, and that increasing Y content causes the blue shift of the emission band. This shift is linked to the structural changes induced in the host lattice because of the substitution of Lu by Y. Upon X-ray excitation the favourable overlap between the defect emission of the host and the Pr^{3+} 4f→4f transitions causes the progressive variation of the ratio between the 5d→4f and the 4f→4f transitions.

Sommario

In questa tesi sono stati preparati vari materiali luminescenti ed è stata eseguita la loro caratterizzazione strutturale e spettroscopica per testare la loro possibile applicazione come fosfori e/o scintillatori. I campioni studiati sono materiali policristallini a base di ossidi (silicati e fosfati) drogati con diversi tipi di ioni lantanidi.

Sono state studiate le proprietà di lumenescenza di Tb^{3+} e Eu^{3+} a temperatura ambiente e le loro evoluzioni nell'intervallo di 8-300 K, in vari silicati a base di Tb con una struttura di tipo silico-carnotite. Nel caso di $Ca_3Tb_{2-x}Eu_xSi_3O_{12}$ è stato osservato un efficiente trasferimento di energia Tb^{3+}-Eu^{3+} a seguito di eccitazione nell'UV. In $Ca_3Tb_2Si_3O_{12}$ e $Ca_3Tb_{2-x}Eu_xSi_3O_{12}$ è stata trovata una veloce migrazione di energia tra gli ioni Tb^{3+}. È stata studiata anche un'altra diversa serie di composti con struttura silico-carnotite a temperatura ambiente. In questo caso, i campioni sono materiali a base di Gd e Y, drogati con Tb^{3+} e Eu^{3+}. Il colore della emissione risultante di questi sistemi può essere modificato controllando il rapporto di concentrazione Tb^{3+}/Eu^{3+}, portando ad una emissione prossima al bianco nel caso di alcuni dei campioni analizzati.

L'effetto dei cambiamenti strutturali della matrice sulla luminescenza del Pr^{3+} è stato studiato in due famiglie di fosfati. Nel caso delle polveri di $Ca_9M(PO_4)_7$ (M = Al, Lu) è stato osservato che le proprietà ottiche delle transizioni 4f→4f del Pr^{3+} sono abbastanza insensibili alla natura del catione M, ma dipendono fortemente dalla quantitá di drogante: per un'alta concentrazione del Pr^{3+} l'emissione dal livello $^1D_2$ è spenta a causa della presenza di processi di cross relaxation, mentre nessun cambiamento evidente è stato osservato nelle transizioni originate nel livello $^3P_0$. Nel caso dei campioni $K_3Lu_{1-x}Y_x(PO_4)_2$:Pr^{3+}, è stato trovato che l'emissione a seguito di eccitazone UV è dominata dalle transizioni intraconfigurazionali 5d→4f del Pr^{3+} e che l'aumento della quantità di Y causa uno spostamento della banda di emissione verso il blu. Questo spostamento è collegato ai cambiamenti strutturali indotti nella matrice a causa della sostituzione del Lu con Y. Eccitando con raggi X la favorevole sovrapposizione tra l'emissione dovuta ai difetti della matrice e le transizioni 4f→4f del Pr^{3+} provoca una progressiva variazione del rapporto tra le transizioni 5d→4f e 4f→4f.

Contents

Chapter 1

Introduction

1.1. Background

The development during the 20th century of luminescence-based technologies has given rise to an intense research in the field of suitable luminescent materials. These are substances able to convert certain types of energy into electromagnetic radiation, with an emission that lies in the UV-IR range, mainly in the visible. Their technological applications are numerous and cover many areas: lighting, detectors, imaging, displays, medicine and many others.

Special attention has been paid to rare-earth based materials, thanks to their outstanding optical properties. In general, these ions exhibit sharp bands in their emission and excitation spectra, which correspond to electronic transitions within their incompletely filled 4f-shell. The 4f-shell is shielded from the environment by the 5s and 5p shells, which causes that the $4f^n$ valence electrons are weakly affected by the surrounding ions. As a result, the 4f energy levels of rare earth ions do not strongly depend on the host lattice, which results in the aforementioned sharp lines. On the contrary, the energy position of the $4f^{n-1}5d$ levels is strongly influenced by the surroundings, which gives broad absorption and emission bands instead of sharp lines. The majority of the Ln^{3+} ions do not show $5d \rightarrow 4f$ emission due to the presence of the $4f^n$ levels just below the lowest $4f^{n-1}5d$ state, which allows fast non radiative relaxation to the $4f^n$ states. In fact, only in few trivalent rare earth ions has been observed efficient $5d \rightarrow 4f$ emission.

An important area in the study of the luminescence properties of Ln^{3+} is energy transfer, which has been widely studied over the years [1, 2]. Energy transfer is crucial for the development of innovative scintillators, phosphors, nanothermometers, materials for solar cells and optical bioimaging, and many other luminescent materials and devices [3-6]. In concentrated lanthanide compounds the excitation energy absorbed in the

sensitizer can migrate over the Ln^{3+} sublattice via multi-step energy transfer. Migration can transport the energy to a killer centre (impurities, defects), which causes the quenching of the luminescence, or to a luminescent activator, which results in light emission. Avoiding luminescence quenching is a big issue in most applications, whereas energy transfer in pairs of ions and from the host to the activator is the basis of many luminescence-based technologies. It is clear from this that the knowledge of the energy transfer processes present in luminescent materials is very important, including also the role of energy migration.

Nowadays, new more efficient and brighter materials with emission in the visible range are required for electronics and lighting industries. The increasing demand on these fields, however, requires also new technologies that are environmentally friendly [7, 8]. In addition, during the last decade the need for improved radiation detectors began to grow rapidly, as a result of the new advances in different technological areas. The development of the new highly luminous accelerators for high energy physics, and the new medical diagnosis techniques based on imaging demanded new materials with better properties and faster response in order to improve their performance and results [9, 10].

Expanding our knowledge of the mechanisms and phenomena involved in the optical properties of the lanthanide ions is, then, interesting not only from a fundamental point of view but also for improving our technological perspectives.

1.2. Objectives

In the present thesis, different inorganic luminescent oxide-based materials have been synthesized and tested in order to evaluate their luminescence properties, and their possible use in phosphor and/or scintillator applications. The work presented can be divided into two main parts: the first one is focused on the study of the luminescent properties of materials doped with Tb^{3+} and Eu^{3+} ions, whereas in the second one the attention is given to materials doped with Pr^{3+} ions.

In chapters 3 and 4 the luminescence properties of Tb^{3+} and Eu^{3+} have been studied in several silicates having silico-carnotite-type structure. In chapter 3 special attention has been paid to the Tb^{3+}-Eu^{3+} energy transfer processes. The objective was to test the possibilities of using Tb^{3+} as a sensitizer of Eu^{3+} in order to improve its luminescent properties, as well as the overall emission performance of the material. Chapter 4, however, focuses on the possibility to tune the emission colour of the investigated materials from red to pinkish-whitish by changing the concentration of Tb^{3+} and Eu^{3+} ions. The aim in this case was to obtain a single-phase white-emitter material.

In chapter 5 the 4f→4f spectroscopy of Pr^{3+} is studied in various phosphates belonging to the whitlockite family. The objective was to analyse the structural characteristics of the hosts and their influence in the luminescent properties of Pr^{3+}.

Finally, in chapter 6 the 5d→4f emission of Pr^{3+} is studied in a series of double phosphates. In this case, the attention was paid to the structural effects of Y co-doping on the $K_3Lu_{1-x}Y_x(PO_4)_2:Pr^{3+}$ phosphors, with the objective of understanding their influence on the 5d→4f transitions of Pr^{3+}.

All these chapters have been adapted from already published work. The publications included in this thesis are the following:

Chapter 3. **Energy transfer processes in $Ca_3Tb_{2-x}Eu_xSi_3O_{12}$ (x = 0-2)**, I. Carrasco, K. Bartosiewicz, F. Piccinelli, M. Nikl, M. Bettinelli, *Opt. Mater*. 48 (2015) 252-257.

Chapter 4. **Tunable emission from silico-carnotite type double silicates doped with Tb^{3+} and Eu^{3+}**, I. Carrasco, F. Piccinelli, M. Bettinelli, *Opt. Mater.Express* Vol.6 No. 5 (2016) 1738-1746.

Chapter 5. **Structural and spectroscopic features of whitlockite $Ca_9M(PO_4)_7$ (M = Al^{3+}, Lu^{3+}) powders activated with Pr^{3+} ions**, A. Watras, I. Carrasco, R. Pazik, R.J. Wiglusz, F. Piccinelli, M. Bettinelli, P.J. Deren, *J. Alloys. Comp.*672 (2016) 45-51.

Chapter 6. **Structural effects and 5d→4f emission transition shifts induced by Y co-doping in Pr-doped $K_3Lu_{1-x}Y_x(PO_4)_2$,** I. Carrasco, K. Bartosiewicz, F. Piccinelli, M. Nikl, M. Bettinelli, *J.Lumin.* http://dx.doi.org/10.1016/j.lumin.2016.08.022 (in press)

References

[1] B. Di Bartolo, "Energy Transfer Processes in Condensed Matter", Plenum, New York and London, (1983).

[2] P. R. Selvin, *Nature Struct. Biol. 7* (2000) 730.

[3] V.B. Mikhailik, H. Kraus, P. Dorenbos, *Phys. Status Solidi RRL 3* (2009) 13.

[4] T. Sheng, Z. Fu, J. Wang, X. Fu, Y. Yu, S. Zhou, S. Zhang, Z. Dai, *RSC Adv. 2* (2012) 4697–4702.

[5] B. Zhou, B. Shi, D. Jin, X. Liu, *Nature Nanotech. 10* (2015) 924.

[6] M. Bettinelli, L. Carlos, X. Liu, *Physics Today 68* (2015) 38.

[7] European Commission (2011) Green Paper Lighting the Future: Accelerating the deployment of innovative lighting technologies.

[8] Lin, C. C., Liu, R.-S., *J. Phys. Chem. Lett. 2*, 1268 -1277 (2011).

[9] Lecoq P., Korzhik M., *IEEE Transactions on nuclear science* Vol. 47, No. 4, august (2000) 1311-1314.

[10] Rodnyi, P.A., *Radiation Measurements*, 33 (5) (2001) 605-614.

Chapter 2

Phosphors and scintillators

2.1. Phosphors

The development during the 20th century of luminescence-based technologies (lighting, displays and so on) has given rise to an intense research in the field of suitable luminescent materials in the visible range. The increasing demand in lighting over the last decades, made necessary to develop new efficient and environmentally friendly lighting devices able to replace the old technologies based on incandescent lamps (energetically inefficient) and gas discharge lamps (based on hazardous materials such as mercury). The invention of the blue LEDs (light emitting diodes) in the mid-1990s [1, 2] has led to the development of new efficient devices able to emit white light, based on inorganic phosphors [3]. Phosphor converted LEDs (pcLEDs) do not use mercury, have a longer life expectancy than conventional lamps and have higher energetic efficiency, among other characteristics.

The colour of light is an important issue in lighting applications. Standardization of colorimetry was carried out in 1931 by the Commission Internationale de l'Eclairage (International Commission for Illumination, or CIE) and is represented by the 1931 CIE diagram shown in Figure 2.1.

Any colour in the visible spectrum can be represented by its x and y coordinates. White light is in the centre of the diagram, with the equal energy point at the coordinates (1/3, 1/3). To any light source a correlated colour temperature (CCT) can be assigned, which is the temperature of an ideal black body with a hue similar to that of the source of interest. Light sources with high CCT values are perceived by the human eye as cold (bluish) lights, whereas those with low CCT values are perceived as warm (reddish) ones. The quality of light is characterized by its colour rendering index (CRI), which measures in a quantitative way the ability of a source to reproduce the true colours of various objects when compared with an ideal

natural light source. High values of CRI are required for high quality and comfortable lighting.

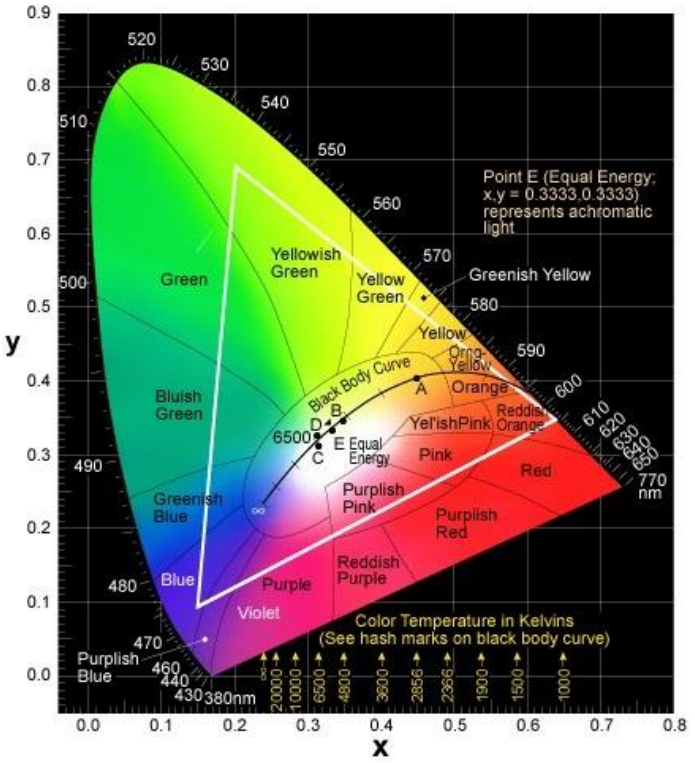

Fig. 2.1. CIE diagram [4].

There are three main strategies for obtaining white light with solid state lighting devices: multiple LED chips with emission at different wavelengths combined in a single device; a blue LED chip with a suitable phosphor (usually a yellow phosphor or a mixture of red and green (RG) phosphors); and a NUV (near ultraviolet) LED chip in combination with a mixture of red, green and blue (RGB) phosphors. The multiple-LEDs approach (usually a combination of red, green and blue LEDs) presents some technological and optical drawbacks (complex electronics, losses due to reabsorption in the interfaces, low CRI, among others). For these reasons, the currently used devices are based on the use of only one LED combined with suitable phosphors. Here, the strategy selected (blue chip + yellow or RG phosphors; or NUV LED + RGB phosphors) strongly depends on the desired application.

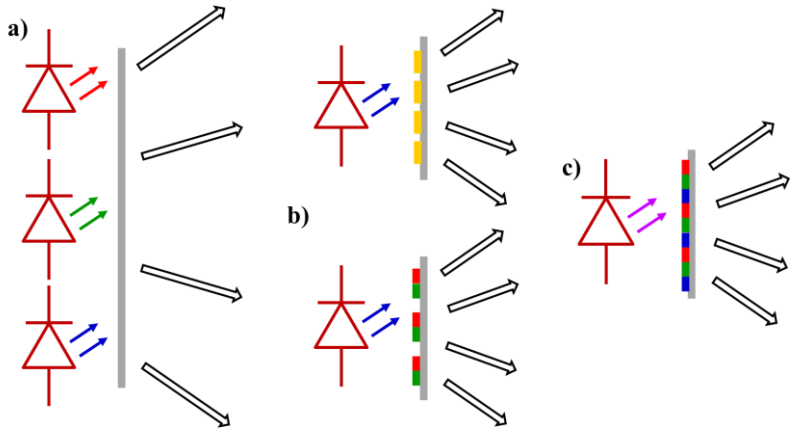

Fig. 2.2. Sketch of the three main WLEDs strategies: a) Three-LED strategy with RGB LED chips, b) approach with a blue LED and a yellow phosphor or RG phosphors and c) the multiple-phosphor strategy with a NUV LED with RGB phosphors.

Currently, the most common pcWLEDs are based on single-phosphor-converted blue LEDs using yellow phosphors. However, their CRI is low and their CCT is high due to the lack of red component, which makes them not good enough for certain applications, like residential lighting. Devices with a NUV LED and multiple phosphors present high CRI and stable emission colour, and are advantageous if the efficiency of the NUV LED is better than that of the blue LED. However, reabsorption in the different phosphors can take place, which reduces the overall efficiency of the system. In this direction, single-phase white-emitting materials are attracting a lot of interest in the last years.

Oxide-based materials attract a lot of attention because they are quite easy and safe to prepare, present a good structural flexibility, and can be employed in air atmosphere. Nevertheless, their cost is quite low if compared with other possible compounds as nitrides or sulphides, which make oxides competitive from a technological perspective.

The majority of phosphors are activated with lanthanide ions, although in some cases transition metal ions are also employed. Many systems are based on Ce^{3+} and Eu^{2+}, which present a broad an intense 5d→4f emission band in the blue-green region that can be shifted to longer wavelengths by selecting the appropriate host. Thanks to this behaviour, these two ions are

widely used in the fabrication of blue [5, 6, 7], yellow [8, 9] and green [10, 11] phosphors. Red phosphors are more complex since Ce^{3+} and Eu^{2+} present a poor red emission, and the requirements for inducing a red shift strong enough to achieve the desired wavelengths happen only in few materials. The alternative is to use ions with intraconfigurational transitions that emit in the red region, like Eu^{3+}. However, in this case the weakness of the involved transitions (parity-forbidden) has to be overcome for practical applications. An interesting approach to this problem is the use of sensitizers in order to overcome the weak absorption probability of the emitting ions, by terms of energy-transfer.

2.2. Scintillators

Inorganic scintillators are luminescent materials able to convert high energy radiation (α-, β-, γ-, X-rays, neutrons or high energetic particles,) into radiation in the UV-VIS spectral region. These materials are commonly used in radiation detectors for applications in medical imaging, security applications or high-energy physics among many others. In these applications, scintillators are the primary sensor that emits light when is struck by the high-energy photons.

The scintillation mechanism is a complex process that can be divided into three consecutive subprocesses: conversion, transport and luminescence. These three stages determine the overall scintillation efficiency, which is given by the number of photons produced per energy of incoming particle. Since transport and luminescent stages are slower than the initial conversion stage, these steps rule the kinetics of the light response. Retrapping processes during transport introduce slower non-exponential components, the so-called afterglow, that can last even at long times after cutting off the excitation. This emission cannot be used in the scintillation counting mode, so afterglow has to be suppressed for technological applications [12].

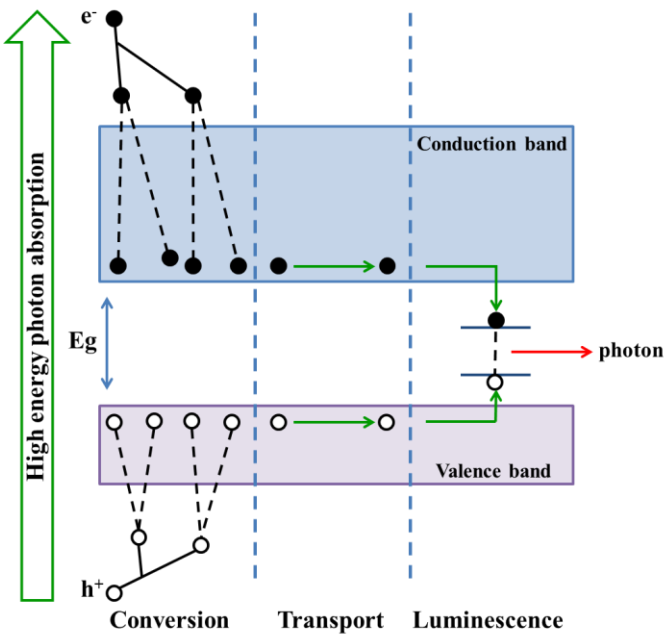

Fig. 2.3. Sketch of the scintillation mechanism.

The specific properties of a scintillator material strongly depend on its application, but in general scintillators with high light output, good attenuation power, low afterglow and a fast scintillating decay time are required. These properties are strongly related to the host lattice. Nowadays oxide-based materials doped with rare-earth ions are widely used for the development and improvement of scintillators [13, 14]. In particular, the 5d→4f emissions of Pr^{3+} in wide band-gap materials have been attracting a lot of attention during the last years, especially for applications that require fast emission decays [15].

In the case of Pr^{3+}, high energy excitation can lead to 5d→4f or 4f→4f emission transitions. The dominant transition is determined by the nature of the host lattice, and by the energetic position of the 4f5d levels with respect to the $^1S_0$ level of the $4f^2$ configuration (which is located at about 46500-46900 cm^{-1}) [16]. If the 4f5d states overlap with the $^1S_0$ level or are located at lower energies, radiative relaxation from the lowest state of the 4f5d configuration can occur. This emission is characterized by broad bands and short decay constants (tens of nanoseconds). On the other hand, if the

energy of the lowest state from 4f5d is higher than the energy of the $^1S_0$ level, efficient intraconfigurational emission within the 4f-shell can take place. In this case, emission is characterized by sharp bands and long decay times.

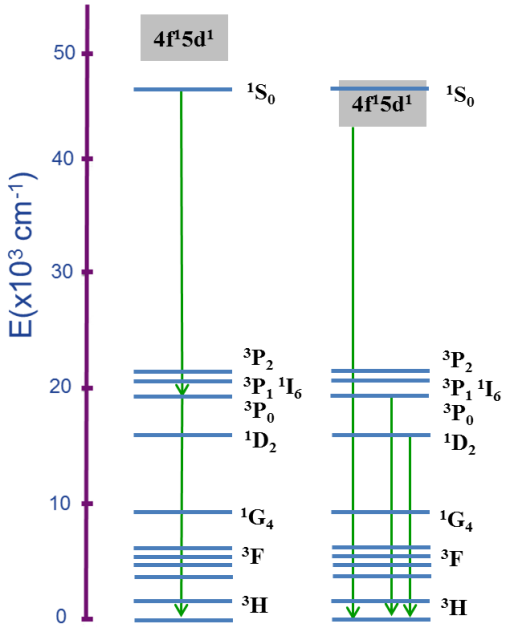

Fig. 2.4. Energy level scheme of Pr^{3+} showing the $4f^2$ levels and two possibilities for the position of the 4f5d states. On the left the lowest 4f5d level is above the $^1S_0$ level making 4f→4f transitions possible. On the right the 4f5d level is situated below the $^1S_0$ level and fast UV 5d→4f emission is possible.

References

[1] Nakamura S., Mukai, T., Senoh M., *Appl Phys Lett* 64 (1994) 1687-1689.

[2] Pimputkar S., Speck JS., DenBaars SP., Nakamura S., *Nat Photonics* 3 (2000) 180-182.

[3] George NC., Denault KA., Seshadri R., *Annu Rev Mat Res* 43 (2013) 481-501.

[4] Everredtronics http://www.everredtronics.com/images/CIE%201931.jpg

[5] Shang M., Li G., Geng D., Yang D., Kang X., Zhang Y., Lian H., Lin J., *J Phys Chem C* 116 (2012) 10222-10231.

[6] Zhou J., Xia Z., Yang M., Shen K., *J Mater Chem* 22 (2012) 21935-21941.

[7] Wang ZL., Cheah KW., Tam HL., Gong ML., *J Alloys Compd* 482 (2009) 437-439.

[8] Dorenbos P., *J Lumin* 134 (2013) 310-318.

[9] Xie R-J., Hirosaki N., Mitomo M., Takahashi K., Sakuma K., *Appl Phys Lett* 88 (2006) 101-104.

[10] Sun J., Zeng J., Sun Y., Du H., *J Alloys Compd* 540 (2012) 81-84.

[11] Shimomura Y., Honma T., Shigeiwa M., Akai T., Okamoto K., Kijima N., *J Electrochem Soc* 154 (2007) J35-J38.

[12] Nikl M., Vedda A. and Laguta V., "Single-crystal scintillator materials" in Springer Handbook of crystal growth. (2010) 1663-1700.

[13] Rétot H., Bessière A., Viana B., LaCourse B. and Mattmann E., *Opt Mater* 33 (2011) 1008-1011.

[14] Nikl M., Laguta V.V. and Vedda A., *Phys. Stat. Sol. (b)* 245, No. 9 (2008) 1721-1722.

[15] Trevisani M., Ivanovskikh K.V., Piccinelli F., Bettinelli M., *J Lumin* 152 (2014) 2-6.

[16] Srivastava A.M., Jennings M. and Collins J., *Opt Mater* 34 (2012) 1347-1352.

Chapter 3

Energy transfer processes in $Ca_3Tb_{2-x}Eu_xSi_3O_{12}$ (x = 0-2)

The luminescent properties of Tb^{3+} and Eu^{3+} have been studied in several silicates having a silico-carnotite-type structure. Fast energy migration among Tb^{3+} ions has been found in $Ca_3Tb_2Si_3O_{12}$ and $Ca_3Tb_{2-x}Eu_xSi_3O_{12}$ (x=0-0.1). In the case of $Ca_3Tb_{2-x}Eu_xSi_3O_{12}$, Tb^{3+}-Eu^{3+} energy transfer is observed upon excitation in the UV bands of Tb^{3+}. The transfer gives rise to strong emission from Eu^{3+} in the red spectral region at 612 nm. The efficiency of the transfer at room temperature in $Ca_3Tb_{1.9}Eu_{0.1}Si_3O_{12}$ has been evaluated. The temperature evolution of the luminescent properties of $Ca_3Tb_2Si_3O_{12}$ and $Ca_3Tb_{1.9}Eu_{0.1}Si_3O_{12}$ has been studied at temperatures ranging from 8 to 330 K.

3.1 Introduction

Despite numerous studies over the years, energy transfer processes are still interesting from both a fundamental and an applied point of view, as transfer processes in pairs of ions and from the host to luminescent ions are crucial for development of innovative luminescent materials and devices [1, 2, 3]. For this reason, it is interesting to consider sensitization process, which is a traditional manner for enhancing luminescence efficiency of phosphors, taking into account the increasing importance of near UV-LEDs (~370 nm) excited phosphors, given their potential application in the development of white LEDs **[**4]. It is well known that Tb^{3+} is a sensitizer for Eu^{3+} in the UV-VIS range [5, 6], making the materials containing Tb^{3+} and Eu^{3+} an interesting field in the search for novel efficient phosphors. [7, 8].

Among the large number of suitable hosts for Ln^{3+} luminescent ions, silicate compounds play an important role due to their good transparency in the UV-VIS region, chemical stability and relatively low price. Silicates $Ca_3M_2Si_3O_{12}$ ($M=Ln^{3+}$) exhibit a stable silico carnotite-like structure when M is a lanthanide ion in the range Eu-Lu [9]. These materials are of high interest from the spectroscopic point of view, and are to be considered as suitable hosts for doping with luminescent trivalent lanthanide ions [10].

In this chapter, the Tb^{3+}-Eu^{3+} energy transfer processes have been analyzed by systematically studying the room temperature luminescent properties of $Ca_3Tb_2Si_3O_{12}$, $Ca_3Eu_2Si_3O_{12}$ and $Ca_3Tb_{2-x}Eu_xSi_3O_{12}$ powders for various Eu^{3+} doping concentration, as well as the evolution with temperature of the luminescent properties of $Ca_3Tb_2Si_3O_{12}$ and $Ca_3Tb_{1.9}Eu_{0.1}Si_3O_{12}$ powders.

3.2 Experimental methods and structural characterization

Polycrystalline samples of $Ca_3Tb_2Si_3O_{12}$, $Ca_3Tb_{2-x}Eu_xSi_3O_{12}$ (x=0.02, 0.04, 0.08 and 0.1) and $Ca_3Eu_2Si_3O_{12}$ were synthesized by solid state reaction at high temperature. $CaCO_3$ (>99%), Tb_4O_7 (99.99%), SiO_2 (99.999%) and Eu_2O_3 (99.99%) powders were mixed and pressed into pellets under a load of 10 tons. The samples underwent three thermal

treatments at 1450 ^oC for 3 hours under air atmosphere, with intermediate grindings.

Powder X-ray diffraction (PXRD) measurements were performed to analyse the structure of the synthesized compounds. Experiments were carried out with a Thermo ARL X'TRA powder diffractometer, operating in the Bragg-Brentano geometry and equipped with a Cu-anode X-ray source (Kα, α =1.5418 Å), using a Peltier Si (Li) cooled solid state detector. The patterns were collected with a scan rate of $0.04^o/s$ in the $5\text{-}90^o$ 2θ range. The phase identification was performed with the PDF-4+2013 database provided by the International Centre for Diffraction Data (ICDD). Polycrystalline samples were ground in a mortar and then put in a low-background sample holder for the data collection. The collected PXRD patterns are presented in Figure 3.1. All the obtained materials are single phase and posses an orthorhombic crystal structure (space group, *Pnma*). They are isostructural with silico-carnotite $Ca_5(PO_4)_2SiO_4$ (orthorhombic) [11]. The structural formula can be represented as $AB_2C_2(EO_4)_3$ where A, B and C refer, respectively, to nine-,eight-, and seven-coordinate cationic sites, characterized by very low site symmetries (C_1 or C_s). In the case of $Ca_3Ln_2Si_3O_{12}$ the distribution of the cations on the three available crystal sites is strongly dependent on the nature of the rare earth ion. [12, 13].

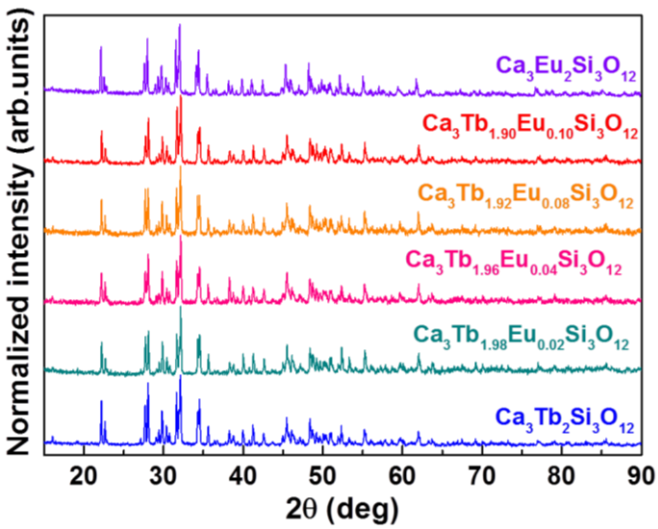

Fig. 3.1. Collected PXRD patterns of the $Ca_3Tb_{2-x}Eu_xSi_3O_{12}$ samples.

Room temperature luminescence was measured with a Fluorolog 3 (Horiba-Jobin Yvon) spectrofluorometer, equipped with a Xe lamp, a double excitation monochromator, a single emission monochromator (mod.HR320) and a photomultiplier in photon counting mode for the detection of the emitted signal. For the temperature dependent study, the luminescence and decay kinetics measurements were performed in the temperature range 8-330 K using the custom made 5000M Horiba Jobin Yvon fluorescence spectrometer. A Janis closed cycle cryostat was used in all the experiments. In the steady state spectra measurements, the sample was excited by deuterium lamp (Heraeus Gmbh). All the spectra were corrected for the spectral distortions of the setup. In decay kinetics measurements a xenon microsecond flashlamp was used and the signal was recorded by means of multichannel scaling method. True decay times were obtained using the convolution of the instrumental response function with an exponential function and the least-square-sum-based fitting program (SpectraSolve software package). For the $Ca_3Tb_2Si_3O_{12}$ and $Ca_3Tb_{1.9}Si_3O_{12}$ phosphors, room temperature radioluminescence was measured upon excitation with a conventional X-ray (40 kV, 15 mA) tube (Seifert Gmbh).

3.3 Results and discussion

3.3.1 Room temperature spectroscopy

Figure 3.2a shows the room temperature emission spectra of $Ca_3Tb_2Si_3O_{12}$ measured upon excitation at 377 nm (into the $^5D_3$ level of Tb^{3+}), and $Ca_3Eu_2Si_3O_{12}$ recorded upon excitation at 393 nm. For $Ca_3Tb_2Si_3O_{12}$ it is possible to observe strong $^5D_4$ emission and no significant $^5D_3$ emission, due to efficient cross relaxation processes that transfer population from $^5D_3$ to $^5D_4$, strongly reducing the $^5D_3$ lifetime and the blue luminescence intensity with the increase of Tb^{3+} concentration:

$$^5D_3 + {}^7F_6 \rightarrow {}^5D_4 + ({}^7F_0, {}^7F_1)$$

The occurrence of these processes is expected in fully concentrated Tb^{3+} materials [14, 15]. In the case of $Ca_3Eu_2Si_3O_{12}$ five bands corresponding to emission from $^5D_0$ level of Eu^{3+} are observed.

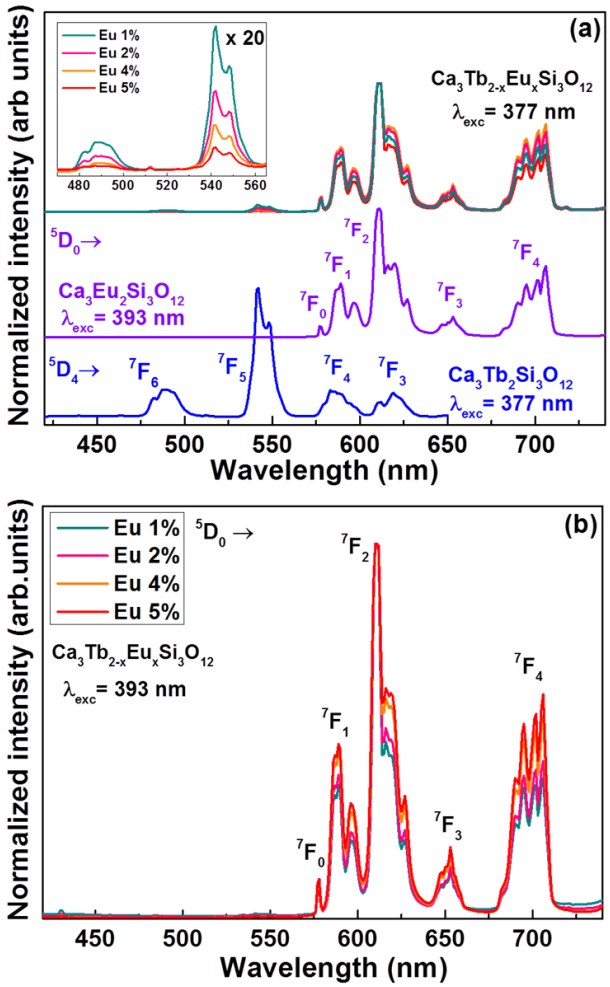

Fig. 3.2. (a) Room temperature emission spectra of $Ca_3Tb_2Si_3O_{12}$, $Ca_3Eu_2Si_3O_{12}$ and $Ca_3Tb_{2-x}Eu_xSi_3O_{12}$ measured upon excitation at 377, 377 and 393 nm respectively. The spectrum of $Ca_3Tb_2Si_3O_{12}$ is normalized to Tb^{3+} $^5D_4\rightarrow{}^7F_5$ emission, whereas the spectra of $Ca_3Eu_2Si_3O_{12}$ and $Ca_3Tb_{2-x}Eu_xSi_3O_{12}$ are normalized to Eu^{3+} $^5D_0\rightarrow{}^7F_2$ emission. Inset shows in detail the weak Tb^{3+} emission bands for $Ca_3Tb_{2-x}Eu_xSi_3O_{12}$. (b) Room temperature emission spectra of $Ca_3Tb_{2-x}Eu_xSi_3O_{12}$ measured upon excitation at 393 nm.

The emission spectra of $Ca_3Tb_{2-x}Eu_xSi_3O_{12}$ (x = 0.02, 0.04, 0.08 and 0.1) measured upon excitation at 377 nm are also presented in Figure 3.2a. All the spectra are normalized to the $^5D_0\rightarrow{}^7F_2$ band of Eu^{3+}. For these materials emission is dominated by strong bands originating from the $^5D_0$ level of Eu^{3+}, and only weak $^5D_4\rightarrow{}^7F_6$ and $^5D_4\rightarrow{}^7F_5$ emission bands of Tb^{3+}

are observed (in detail in the inset of Figure 3.2a). It is noticeable that the higher the Eu^{3+} concentration, the lower the intensity of the Tb^{3+} emission bands. All these features clearly indicate the existence of an energy transfer process from Tb^{3+} to Eu^{3+}. For all the compounds, the emission bands are relatively broad due to the high degree of disorder present in the host, as observed by Piccinelli *et al.* [9] in other silico-carnotite-type materials. Figure 3.2b presents the emission spectra of $Ca_3Tb_{2-x}Eu_xSi_3O_{12}$ (x = 0.02, 0.04, 0.08 and 0.1) measured upon direct excitation into Eu^{3+} at 393 nm. No Tb^{3+} emission has been observed in this case, confirming that no back transfer is present in the system.

The excitation spectra of all samples are shown in Figure 3.3. The energy level diagrams for Tb^{3+} and Eu^{3+} in the $Ca_3Tb_2Si_3O_{12}$:Eu^{3+} phosphors are presented in Figure 3.4 to help understanding the experimental results.

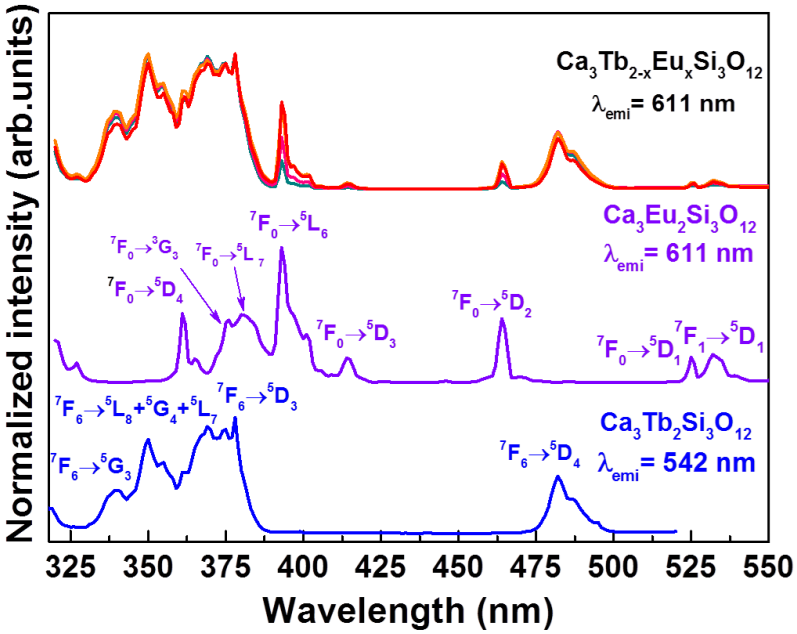

Fig. 3.3. Room temperature excitation spectra of $Ca_3Tb_2Si_3O_{12}$, $Ca_3Eu_2Si_3O_{12}$ and $Ca_3Tb_{2-x}Eu_xSi_3O_{12}$ monitoring emission at 542 nm (Tb^{3+}), 611 nm (Eu^{3+}) and 611 nm (Eu^{3+}) respectively.

In the case of $Ca_3Tb_2Si_3O_{12}$ the spectrum is composed of overlapping bands in the UV ranging from 300 nm to almost 400 nm, and of a weaker band at 480 nm. The transitions have been assigned as $^7F_6 \rightarrow {}^5G_3$ at 340 nm,

$^7F_6 \rightarrow {}^5L_8 + {}^5G_4$ at 350 nm, $^7F_6 \rightarrow {}^5D_3$ at 377 nm, which is the most intense, and $^7F_6 \rightarrow {}^5D_4$ at 480 nm. The spectrum of $Ca_3Eu_2Si_3O_{12}$ is composed of various bands ranging from 360 nm to 430 nm and other bands at 460 nm and 530 nm. In this case the transitions have been assigned as $^7F_0 \rightarrow {}^5D_4$ at 360 nm, $^7F_0 \rightarrow {}^3G_3$ and $^7F_0 \rightarrow {}^5L_7$ at 375 and 380 nm, $^7F_0 \rightarrow {}^5L_6$ at 393 nm, which is the most intense, $^7F_0 \rightarrow {}^5D_3$ at 412 nm, $^7F_0 \rightarrow {}^5D_2$ at 460 nm, $^7F_0 \rightarrow {}^5D_1$ at 525 nm and $^7F_1 \rightarrow {}^5D_1$ at 530 nm. In the case of Eu-doped samples, the excitation spectra when monitoring the $^5D_0$ emission of Eu^{3+} are dominated by Tb^{3+} bands in the UV region. Only a few Eu^{3+} excitation bands are observed. These results confirm the Tb^{3+}-Eu^{3+} energy transfer.

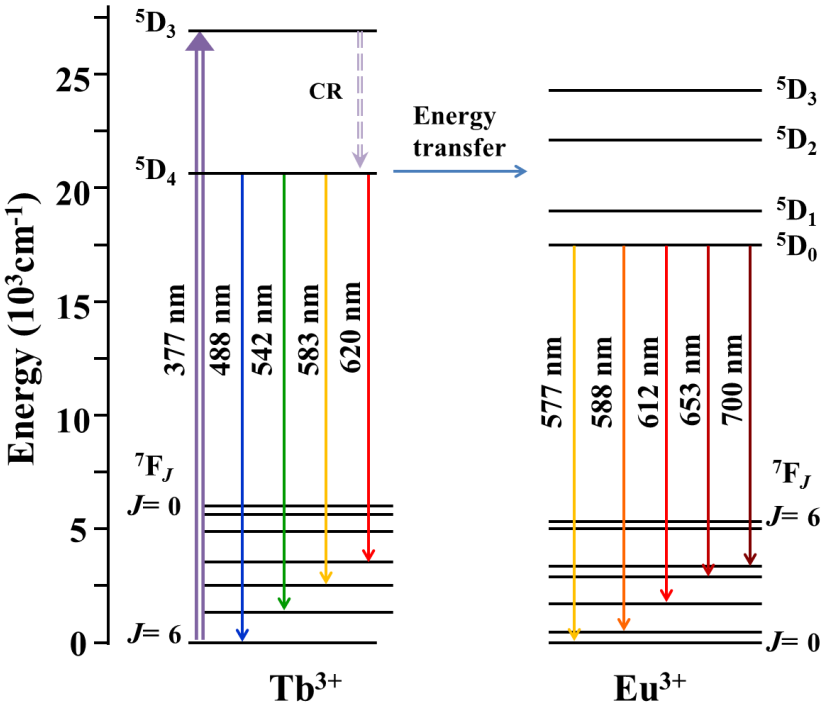

Fig. 3.4. Energy level diagram for Tb^{3+} and Eu^{3+} ions in $Ca_3Tb_2Si_3O_{12}$: Eu phosphors.

Various Tb^{3+}-Eu^{3+} phonon assisted energy transfer processes have been proposed in the literature [5, 16]; some of the most important are:

$$Tb^{3+}\,(^5D_4) + Eu^{3+}\,(^7F_0) + \Delta E_{ph} \rightarrow Tb^{3+}\,(^7F_4) + Eu^{3+}\,(^5D_0)$$

$$Tb^{3+}\,(^5D_3) + Eu^{3+}\,(^7F_0) \rightarrow Tb^{3+}\,(^7F_3) + Eu^{3+}\,(^5D_2) + \Delta E_{ph}$$

where the phonon energies involved (ΔE_{ph}) are relatively low (less than 500 cm^{-1}). Due to fast multiphonon relaxation in the host, energy transfer will lead in all cases only to emission from $^5D_0$, as discussed by Bettinelli *et al.* [6].

Decay curves for Tb^{3+} and Eu^{3+} emission were measured upon excitation at 377 and 393 nm. Figure 3.5a shows decay curves for Tb^{3+} emission from $^5D_4$ in Tb^{3+} in two concentrated compounds ($Ca_3Tb_2Si_3O_{12}$ and $Ca_3Tb_{1.9}Eu_{0.1}Si_3O_{12}$), and a diluted Tb^{3+} compound ($Ca_{2.97}Tb_{0.03}Y_{1.98}Si_3O_{12}$) to compare the differences in behaviour of this ion. The obtained time constants are reported in Table 3.1. In the diluted compound there is a clear rise at short times, whereas for the concentrated compounds the curves are well fitted to a single exponential function. This behaviour is explained on the basis of a fast migration regime among the donors, as an effect of the high Tb^{3+} concentration [16, 17]. According to Dexter's theory of energy transfer processes through multipolar interaction, the energy transfer probability from a sensitizer to an activator in a dipole-dipole interaction is given by the following formula [18]:

$$P_{SA} = \frac{3 \cdot 10^{12} f_d}{R^6 \tau_s} \int \frac{f_S(E) F_A(E)}{E^4} dE \qquad (3.1)$$

where f_d is the oscillator strength of the involved absorption transition of the activator, R is the sensitizer-activator distance, τ_s the radiative decay time for sensitizer, f_s and F_A represent the normalized absorption line shape of activator and emission line shape of sensitizer respectively, and E is the energy involved in the transfer. The distance for which the probability of energy transfer equals the probability of a radiative transition is define as the critical distance, and it can be calculated as follows:

$$R_c^6 = 3 \cdot 10^{12} f_d \int \frac{f_S(E) F_A(E)}{E^4} dE \qquad (3.2)$$

Using the calculated spectral overlap for $Ca_3Tb_2Si_3O_{12}$ and assuming that for Tb^{3+} transitions the oscillator strength is $3 \cdot 10^{-7}$ [19], the critical distance for dipole-dipole energy migration among Tb^{3+} ions is estimated to be 7.3 Å. It is interesting to compare this with the average Tb^{3+}-Tb^{3+} distance, which for nearest neighbours can be calculated with the following formula [20]:

$$d = \left(\frac{3V}{4\pi N}\right)^{1/3} \qquad (3.3)$$

where N is the number of Tb^{3+} atoms in the cell and V is the volume of the cell. The average distance has been found to be 3.1 Å, much smaller than the critical distance for dipole-dipole interaction, so that a fast energy migration among Tb^{3+} ions is predicted in this system. This result is in good agreement with the observed behaviour of the decay curves.

The Tb^{3+} decay constant for the 5% Eu^{3+}-doped sample is significantly shortened respect to the one obtained for $Ca_3Tb_2Si_3O_{12}$. The efficiency of the Tb^{3+}-Eu^{3+} transfer can be calculated according to [21, 22]:

$$\eta_T = 1 - \frac{\tau_{Tb-Eu}}{\tau_{Tb}} \qquad (3.4)$$

where τ_{Tb-Eu} and τ_{Tb} are the decay times of Tb^{3+} $^5D_4$ level in the europium-doped and undoped samples respectively. η_T is found to be 0.94, which indicates that in these conditions the Tb^{3+}-Eu^{3+} energy transfer is very efficient. This value is in good agreement with the results reported by Bettinelli *et al.* for $Sr_3Tb_{0.90}Eu_{0.10}(PO_4)_3$ (efficiency 0.93) [6], Zhou & Xia for $La_{2.65}GaGe_5O_{12}$:0.15Tb,0.20Eu (efficiency of 0.87) [8] or Xia *et al.* for $Ba_2Tb_{0.995}(BO_3)_2Cl$:0.005Eu (efficiency of 0.71) [7].

Figure 3.5b presents decay curves for Eu^{3+} $^5D_0$ emission for $Ca_3Tb_{2-x}Eu_xSi_3O_{12}$ and $Ca_3Eu_2Si_3O_{12}$ samples. The curves can be fitted by a single exponential function, and the time constants estimated from the decay curves are also reported in Table 3.1. The profile of the curves is approximatively exponential, which is explained on the basis of fast Tb^{3+}-Tb^{3+} (in the Eu^{3+}-doped samples) and Eu^{3+}-Eu^{3+} (in $Ca_3Eu_2Si_3O_{12}$) migration, as a result of the high concentration of terbium and europium ions respectively. It is possible to observe that there are no significant changes on decay curves when varying europium concentration in Eu^{3+}-doped samples, but the decay is shortened in the case of fully europium concentrated compound, probably due to concentration quenching as a result of energy migration to quenching impurities. Inset in Figure 3.5b presents a zoom on Eu^{3+} decay curves in $Ca_3Tb_{2-x}Eu_xSi_3O_{12}$, in which it is possible to observe a small buildup at short times. This rise is difficult to

identify clearly in the highly-doped samples, indicating that the transfer from Tb^{3+} to Eu^{3+} is fast.

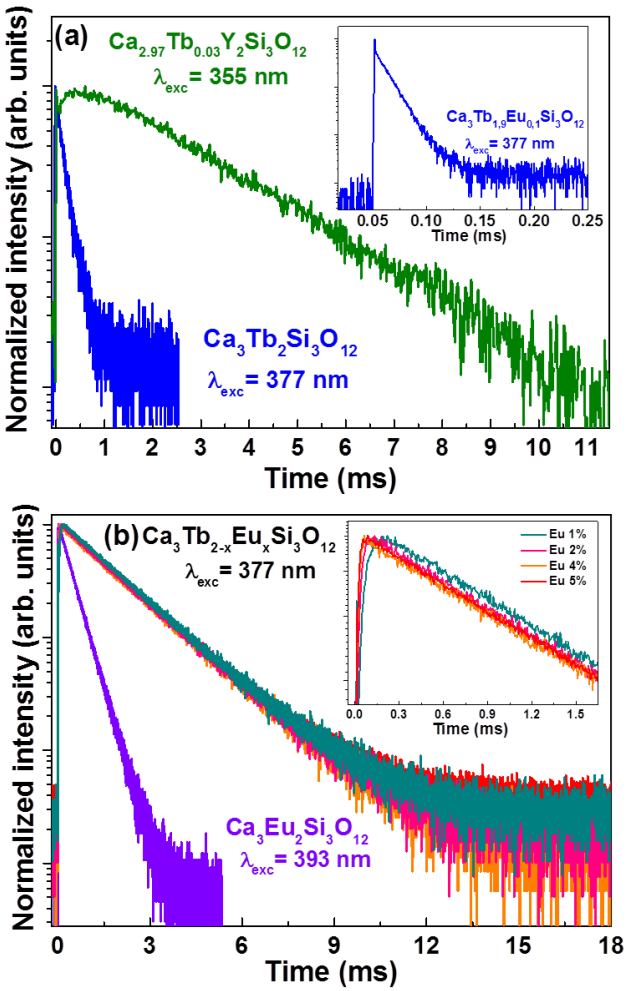

Fig. 3.5. (a) Room temperature decay curves of the $^5D_4$ Tb^{3+} emission excited at 377 nm in fully Tb-compounds ($Ca_3Tb_{1.9}Eu_{0.1}Si_3O_{12}$) and at 355 nm in a diluted compound ($Ca_{2.97}Tb_{0.03}Y_2Si_3O_{12}$). The inset shows the corresponding curve of the $^5D_4$ Tb^{3+} emission excited at 377 nm for $Ca_3Tb_2Si_3O_{12}$. (b) Room temperature decay curves of the $^5D_0$ Eu^{3+} emission excited at 377 nm ($Ca_3Tb_{2-x}Eu_xSi_3O_{12}$) and 393 nm ($Ca_3Eu_2Si_3O_{12}$).

Table 3.1

Decay data for the luminescent levels of Tb^{3+} and Eu^{3+} in several silico-carnotite hosts upon UV excitation.

Material	Excited state	Decay time (ms)
$Ca_{2.97}Tb_{0.03}Y_2Si_3O_{12}$	$^5D_4$ (Tb^{3+})	2.50 (rise)
$Ca_3Tb_2Si_3O_{12}$	$^5D_4$ (Tb^{3+})	0.18
$Ca_3Tb_{1.90}Eu_{0.10}Si_3O_{12}$	$^5D_4$ (Tb^{3+})	0.01
$Ca_3Tb_{1.90}Eu_{0.10}Si_3O_{12}$	$^5D_0$ (Eu^{3+})	1.78
$Ca_3Tb_{1.92}Eu_{0.08}Si_3O_{12}$	$^5D_0$ (Eu^{3+})	1.79
$Ca_3Tb_{1.96}Eu_{0.04}Si_3O_{12}$	$^5D_0$ (Eu^{3+})	1.78 (small rise)
$Ca_3Tb_{1.98}Eu_{0.02}Si_3O_{12}$	$^5D_0$ (Eu^{3+})	1.77 (small rise)
$Ca_3Eu_2Si_3O_{12}$	$^5D_0$ (Eu^{3+})	0.44

Figure 3.6 shows the CIE XYZ chromaticity coordinates diagram for $Ca_3Tb_2Si_3O_{12}$, $Ca_3Tb_{2-x}Eu_xSi_3O_{12}$ and $Ca_3Eu_2Si_3O_{12}$ and a typical picture of the phosphors when excited at 365 nm. As it can be observed, the addition of Eu^{3+} changes the emission colour of the material from green to red, even for low concentrations of activator. The obtained values of CIE coordinates are provided in Table 3.2.

Table 3.2

Values for CIE coordinates of $Ca_3Tb_2Si_3O_{12}$ and $Ca_3Tb_{2-x}Eu_xSi_3O_{12}$ excited at 377 nm and $Ca_3Eu_2Si_3O_{12}$ excited at 393 nm.

Material	x	y
$Ca_3Tb_2Si_3O_{12}$	0.37716	0.53879
$Ca_3Tb_{1.98}Eu_{0.02}Si_3O_{12}$	0.62257	0.36429
$Ca_3Tb_{1.96}Eu_{0.04}Si_3O_{12}$	0.62760	0.36021
$Ca_3Tb_{1.92}Eu_{0.08}Si_3O_{12}$	0.63223	0.35916
$Ca_3Tb_{1.90}Eu_{0.10}Si_3O_{12}$	0.63290	0.35484
$Ca_3Eu_2Si_3O_{12}$	0.63976	0.35515

The room temperature radioluminescence emission spectra of $Ca_3Tb_2Si_3O_{12}$ and $Ca_3Tb_{1.90}Eu_{0.10}Si_3O_{12}$ powders are presented in Figure 3.9. The samples were measured along with the reference BGOP ($Bi_4Ge_3O_{12}$, in powder form), and the spectra are mutually comparable in an absolute way.

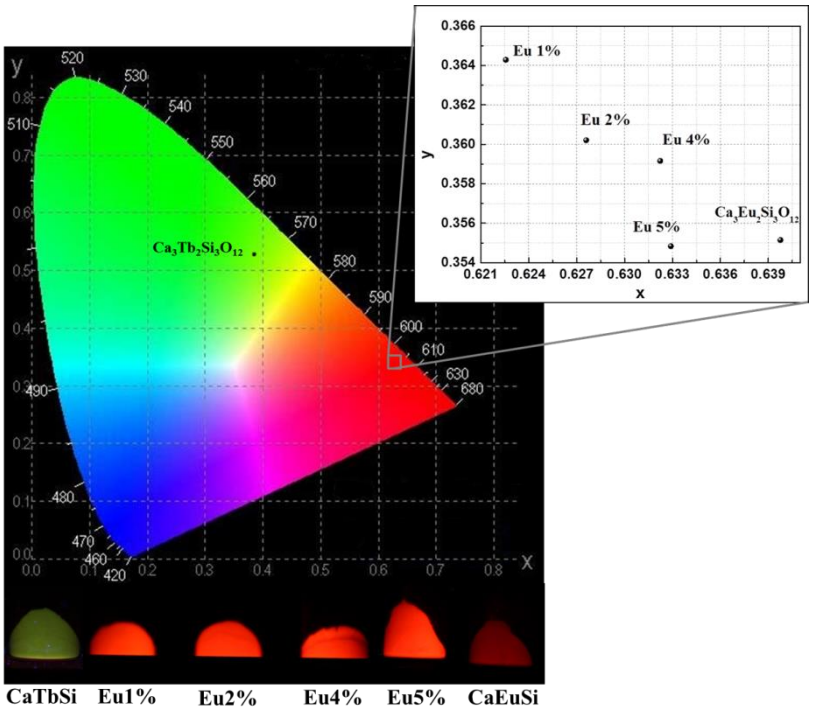

Fig. 3.6. CIE diagram coordinates of $Ca_3Tb_2Si_3O_{12}$ and $Ca_3Tb_{2-x}Eu_xSi_3O_{12}$ excited at 377 nm and $Ca_3Eu_2Si_3O_{12}$ excited at 393 nm, and typical picture of the phosphors when excited at 365 nm.

Radioluminescence emission spectra show clear 4f→4f bands for both $Ca_3Tb_2Si_3O_{12}$ and $Ca_3Tb_{1.90}Eu_{0.10}Si_3O_{12}$ samples. For the undoped sample, clear emission from the Tb^{3+} $^5D_4$ level to $^7F_6$, $^7F_5$, $^7F_4$ and $^7F_3$ levels is observed. In the case of $Ca_3Tb_{1.90}Eu_{0.10}Si_3O_{12}$ very intense emission from Eu^{3+} $^5D_0$ level to $^7F_1$, $^7F_2$, $^7F_3$ and $^7F_4$ levels is observed. Tb^{3+} emission in this sample is almost quenched, as observed previously in the case of UV-excited luminescence. Only a very weak emission peak that corresponds to the $^5D_4 \rightarrow {}^7F_5$ transition of Tb^{3+} can be observed, confirming the energy transfer between Tb^{3+} and Eu^{3+} ions. Moreover, the intensity of the radioluminescence emission of $Ca_3Tb_2Si_3O_{12}$ is quite low when compared to the BGOP standard. The fast migration in the Tb^{3+} sublattice described previously is in this case responsible of the emission quenching. In the case of the $Ca_3Tb_{1.90}Eu_{0.10}Si_3O_{12}$ sample, however, the intensity of the maximum is about five times the intensity of the maximum of the standard.

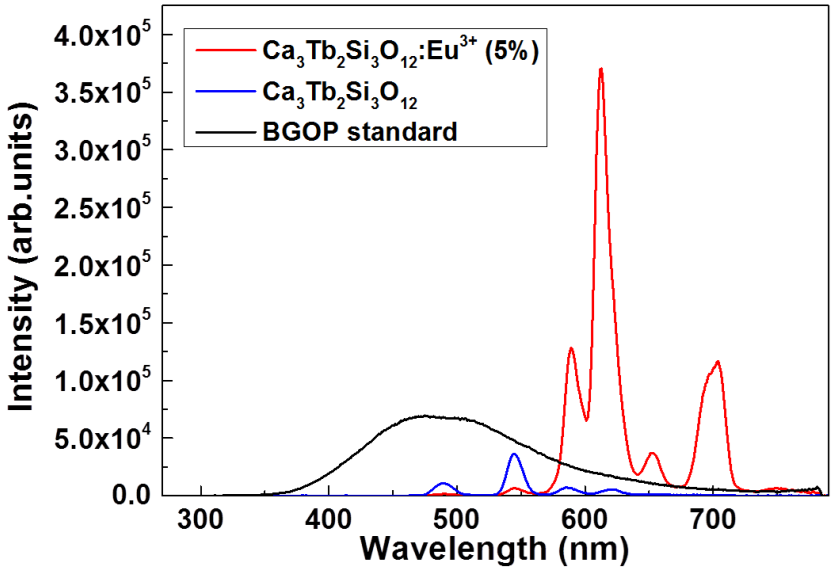

Fig. 3.7. Room temperature radioluminescence spectra of $Ca_3Tb_2Si_3O_{12}$ and $Ca_3Tb_{1.90}Eu_{0.10}Si_3O_{12}$ (X-ray excitation 40 kV, 15 mA, RT). Standard BGOP spectrum is also included as a reference.

3.3.2 Temperature dependent experiments

The temperature evolution in the range 8-330 K of photoluminescence emission and decay time has been studied for $Ca_3Tb_2Si_3O_{12}$ and $Ca_3Tb_{1.9}Eu_{0.1}Si_3O_{12}$. Figure 3.8a shows the temperature evolution of the decay constant for Tb^{3+} emission at 545 nm upon excitation at 370 nm in $Ca_3Tb_2Si_3O_{12}$. Figure 3.8b provides the spectral evolution for Tb^{3+} emission upon the same excitation. The spectrum is dominated by green Tb^{3+} emission at 545 nm, and it is possible to observe a clear decrease of intensity when increasing the temperature of the system, providing an evidence of the previously mentioned energy migration among Tb^{3+} ions. The measured decay curves are approximately exponential, and the obtained values of the decay constants are significantly shorter than the one obtained for an isolated Tb^{3+} ion, which indicates that migration is also present at low temperatures. The evolution of decay time presents a progressive shortening as temperature is increased, until it reaches half of its value when the system is at room temperature. This behaviour is explained on the basis of the

disordered nature of the host, which provides multiple sites available for Tb^{3+} ions, which implies that the energy migration is not completely resonant and has to be assisted by phonons.

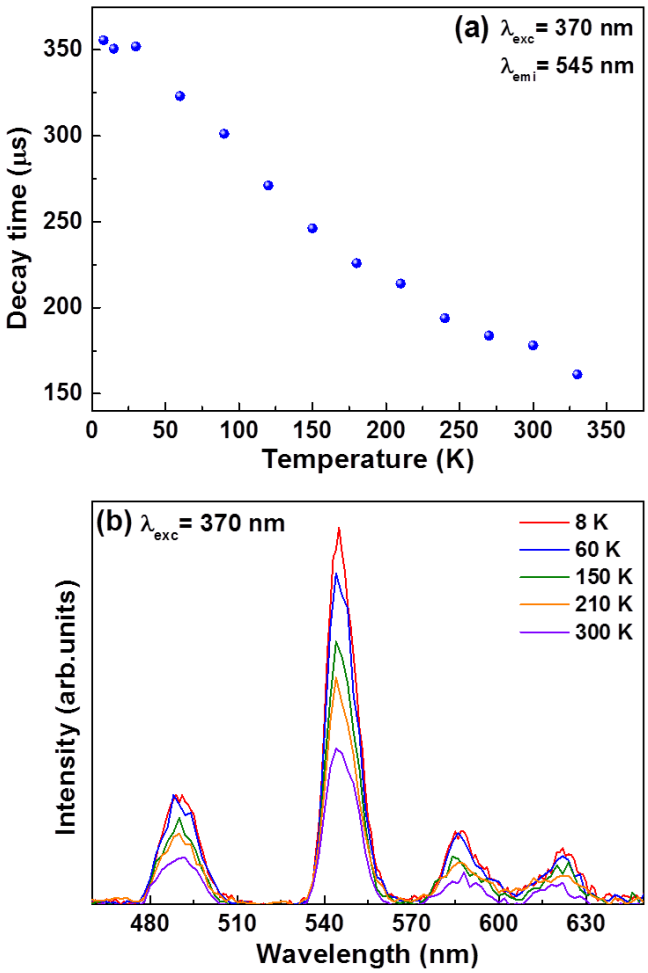

Fig. 3.8. Temperature evolution in the range 8-330 K upon excitation at 370 nm of Tb^{3+} decay time at 545 nm (a), and Tb^{3+} emission (b). The variation of decay constant is about 55%.

Figure 3.9a shows temperature evolution of Tb^{3+} decay time for emission at 540 nm and Eu^{3+} decay time for emission at 611 nm, both for $Ca_3Tb_{1.9}Eu_{0.1}Si_3O_{12}$ phosphor, upon excitation at 370 nm. In Figure 3.9b the evolution of the emission spectrum upon excitation at 370 nm is presented.

The spectrum is dominated at all temperatures by Eu^{3+} red emission at 611 nm, as observed previously at room temperature, with weak green emission bands coming from Tb^{3+}.

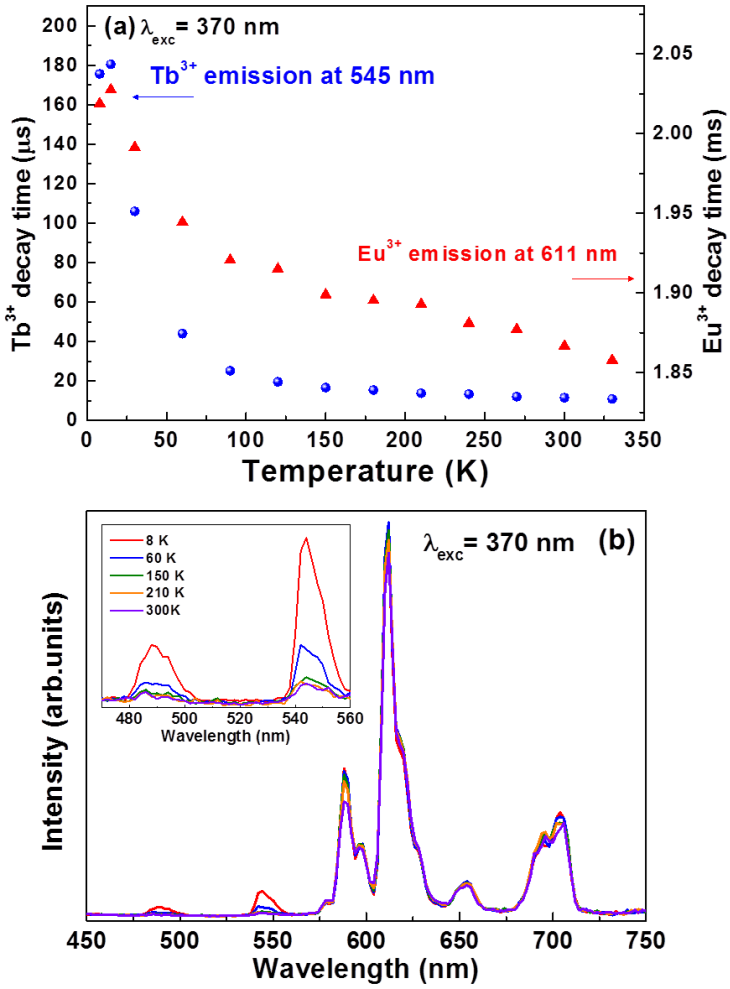

Fig. 3.9. (a) Temperature evolution in the range 8-330 K of Tb^{3+} decay time at 545 nm (dots) and Eu^{3+} decay time at 611 nm (triangles), upon excitation at 370 nm for $Ca_3Tb_{1.9}Eu_{0.1}Si_3O_{12}$ powders. The variation of decay constant is about 94% for Tb^{3+} and 9% for Eu^{3+}. (b) Evolution of $Ca_3Tb_{1.9}Eu_{0.1}Si_3O_{12}$ emission in the range 8-330 K upon excitation at 370 nm. The spectra are normalized to Eu^{3+} $^5D_0 \rightarrow {}^7F_2$ emission. Inset shows in detail Tb^{3+} emission bands.

The intensity of Eu^{3+} emission bands presents a small reduction as temperature is increased. On the contrary, Tb^{3+} emission is almost quenched

due to the combination of the processes of energy migration among Tb^{3+} ions and energy transfer from Tb^{3+} to Eu^{3+}. Decay constant for Eu^{3+} emission does not change significantly in the range studied, while for Tb^{3+} the decay constant is strongly reduced, from 180 μs at low temperature to 12 μs at room temperature. This shortening in time constant is sharp for temperatures up to 60 K, and then decreases slowly. This agrees with the non-resonant nature of the energy transfer, which needs phonon assistance.

Figure 3.10 presents the evolution of the efficiency of the energy transfer with temperature. Efficiency values have been obtained from the experimental data using equation (3.4). The efficiency is about 0.50 at low temperatures and rises up to 0.94 at room temperature. This increase takes place rapidly up to 100 K, at which value the efficiency remains stable.

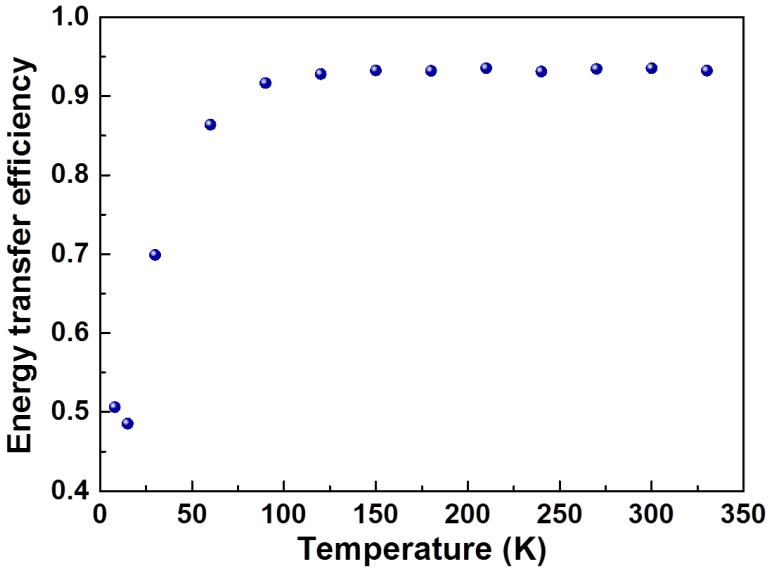

Fig. 3.10.Temperature evolution in the range 8-330 K of Tb-Eu energy transfer efficiency for $Ca_3Tb_{1.9}Eu_{0.1}Si_3O_{12}$ powders.

3.4 Conclusions

In this chapter the luminescent properties of $Ca_3Tb_2Si_3O_{12}$, $Ca_3Eu_2Si_3O_{12}$ and $Ca_3Tb_{2-x}Eu_xSi_3O_{12}$ powders have been systematically studied for various Eu^{3+} doping concentration. The temperature evolution of the luminescence of $Ca_3Tb_2Si_3O_{12}$ and $Ca_3Tb_{1.9}Eu_{0.1}Si_3O_{12}$ in the range 8-330 K has also been studied. The obtained results show that the addition of Eu^{3+} changes the colour emission of the material from green (Tb^{3+}) to red (Eu^{3+}), evidencing the existence of a very efficient Tb^{3+}-Eu^{3+} energy transfer process. The efficiency of the transfer at room temperature evaluated from the experimental decay times is 0.94 for $Ca_3Tb_{1.9}Eu_{0.1}Si_3O_{12}$, indicating that Tb^{3+} emission is almost quenched while Eu^{3+} emission is enhanced. A fast energy migration process among Tb^{3+} ions is found to be present in fully concentrated Tb^{3+} sample, and it has been observed that this process plays a relevant role in the Tb^{3+}-Eu^{3+} energy transfer, enhancing its efficiency.

Taking all these features into account, it is conceivable that it could be possible to synthesize phosphors with intermediate emission colours by adjusting the concentration of Tb^{3+} and Eu^{3+} ions.

References

[1] V.B. Mikhailik, H. Kraus, P. Dorenbos, *Phys Status Solidi RRL* 3 (2009) 13.

[2] T. Sheng, Z. Fu, J. Wang, X. Fu, Y. Yu, S. Zhou, S. Zhang, Z. Dai, *RSC Ad.* 2 (2012) 4697-4702.

[3] T.R. Shojaei, M.A.M. Salleh, K. Sijam, R.A. Rahim, A. Mohsenifar, R. Safarnejad, M. Tabatabaei, *Spectrochimica Acta Part A: Molecular and Biomolecular Spectroscopy* 169 (2016) 216-222.

[4] J. Dong, L.Wanga, C.Cuia, Y.Tiana, P. Huang, *Ceram Int* 41 (2015) 1341-1346.

[5] W. Holloway Jr., M. Kestigian, R. Newman, *Phys Rev Letters* 11 (1963) 458-460.

[6] M. Bettinelli, A. Speghini, F. Piccinelli, J. Ueda, S. Tanabe, *Opt Mater* 33 (2010) 119-122.

[7] Z. Xia, J. Zhuang, L. Liao, *Inorganic Chem* 51 (2012) 7202-7209.

[8] J. Zhou and Z. Xia, *J Mater Chem C* 2 (2014) 6978-6984.

[9] F. Piccinelli, A. Lausi and M. Bettinelli, *J Solid State Che.* 205 (2013) 190-196.

[10] F. Piccinelli, A. Speghini, G. Mariotto, L. Bovo, M. Bettinelli, *J Rare Earths* 27 (2009) 555-559.

[11] B. Dickens and W. E. Brown, *Tschermaks Mineral Petrog Mitt* 16 (1971) 1-27.

[12] G.A. Novak, G.V. Gibbs, *Am Mineral* 56 (1971) 791-825.

[13] F. Piccinelli, A. Lausi, A. Speghini, M. Bettinelli, *J Solid State Chem*. 194 (2012) 233-237.

[14] F. Auzel, J. Dexpert-Ghys, D. Morin, G. Dadoun, J. Ostorero, H. Makram, *Mater Res Bull* 16 (1981) 1521.

[15] J.F.M. dos Santos, I.A.A. Terra, N.G.C. Astrath, F.B. Guimaraes, M.L. Baesso, L.A.O. Nunes, T. Catunda, *J Appl Phys* 117 (2015) 053102.

[16] M. Bettinelli, C.D. Flint, *J Phys Condens Matter* 2 (1990) 8417-8426.

[17] R. K. Watts, *Optical Properties of Ions in Solids*, B. Di Bartolo ed, Plenum Press, New York and London, 1975, p. 307.

[18] D.L. Dexter, *J Chem Phys* 21 (5) (1953).

[19] J.M.P J. Verstegen, J.L. Sommerdijk, J.G. Verriet, *J Lumin* 6 (1973), 425-431.

[20] G. Blasse, *J Solid State Chem* 62 (1986) 207.

[21] J. Pisarska, A. Kos, W.A. Pisarski, *Spectrochim. Acta Part A: Mol. Biomol. Spectrosc*. 129 (2014) 649-653.

[22] E. Álvarez, M.E. Zayas, J. Alvarado-Rivera, F. Félix-Domínguez, R.P. Duarte-Zamorano , U. Caldiño, *J. Lumin*. 153 (2014) 198-202.

Chapter 4

Tunable emission from silico-carnotite type double silicates doped with Tb^{3+} and Eu^{3+}

This chapter presents the spectroscopic characterization of various double silicates with the silico-carnotite orthorhombic structure, co-doped with Tb^{3+} and Eu^{3+}. All the studied materials have been prepared by solid state reaction. Room temperature luminescence spectra and decay kinetics have been measured and analysed. Upon UV excitation at 378 nm, the emission colour varies from red to pinkish, depending on the doping level. The resulting colour can be adjusted by controlling the Tb^{3+}/Eu^{3+} concentration ratio. Control of the doping leads to close-to-white emission in some of the analysed samples upon excitation in the wavelength region useful for LED lighting.

4.1. Introduction

Inorganic phosphors doped with rare earth ions have drawn much interest because of their intense emission efficiencies due to 4f→4f and 5d→4f electronic transitions, and are currently used in many technological fields. Silicate phosphors present high interest from the spectroscopic point of view due to their good transparency in the UV-VIS region and chemical stability, and are to be considered as efficient hosts for doping with luminescent trivalent lanthanide ions [1, 2].

In this chapter, the room temperature luminescence spectra and decay kinetics of $Ca_3M_{1.98}Tb_{0.02}Si_3O_{12}$ (M = Gd, Y), $Ca_3M_{1.98}Eu_{0.02}Si_3O_{12}$ (M = Gd, Y), $Ca_3Gd_{2-x-y}Tb_xEu_ySi_3O_{12}$ and $Ca_3Y_{2-x-y}Tb_xEu_ySi_3O_{12}$ phosphors belonging to silico-carnotite family have been systematically studied for various Tb^{3+} and Eu^{3+} doping concentration, upon UV excitation.

4.2. Experimental methods and structural characterization

Polycrystalline samples of $Ca_3M_{1.98}Tb_{0.02}Si_3O_{12}$ (M = Gd, Y), $Ca_3M_{1.98}Eu_{0.02}Si_3O_{12}$ (M = Gd, Y), $Ca_3Gd_{2-x-y}Tb_xEu_ySi_3O_{12}$ (x = 0.02, y = 0.04; x = 0.02, y = 0.01; x = 0.01, y = 0.01 and x = 0.01, y = 0.005) and $Ca_3Y_{2-x-y}Tb_xEu_ySi_3O_{12}$ (x = 0.02, y = 0.005; x = 0.015, y = 0.003; and x = 0.01, y = 0.005) were prepared by solid state reaction at high temperature (1450 ° C), following the procedures previously described [3, 4].

Powder X-ray diffraction (PXRD) measurements were performed to analyse the structure of the synthesized compounds. Experiments were carried out with a Thermo ARL X'TRA powder diffractometer, operating in the Bragg-Brentano geometry and equipped with a Cu-anode X-ray source (Kα, λ =1.5418 Å), using a Peltier Si (Li) cooled solid state detector. The patterns were collected with a scan rate of 0.04^o/s in the 5-90^o 2θ range. The phase identification was performed with the PDF-4+2013 database provided by the International Centre for Diffraction Data (ICDD). Polycrystalline samples were ground in a mortar and then put in a low-background sample holder for the data collection. All the obtained materials are single phase. They are isostructural with silico-carnotite $Ca_5(PO_4)_2SiO_4$ (orthorhombic, space group, *Pnma*) [5]. The structural formula can be represented as

$AB_2C_2(EO_4)_3$ where A, B and C refer, respectively, to nine-, eight-, and seven-coordinate cationic sites, characterized by very low site symmetries (C_1 or C_S). E could be Si, P or both. It has been shown previously that the $Ca_3RE_2Si_3O_{12}$ (RE-rare earth ions) family of compounds possess orthorhombic *Pnma* crystal structure, and the distribution of the cations on the three available crystal sites is strongly dependent on the nature of the rare earth ion [6, 7].

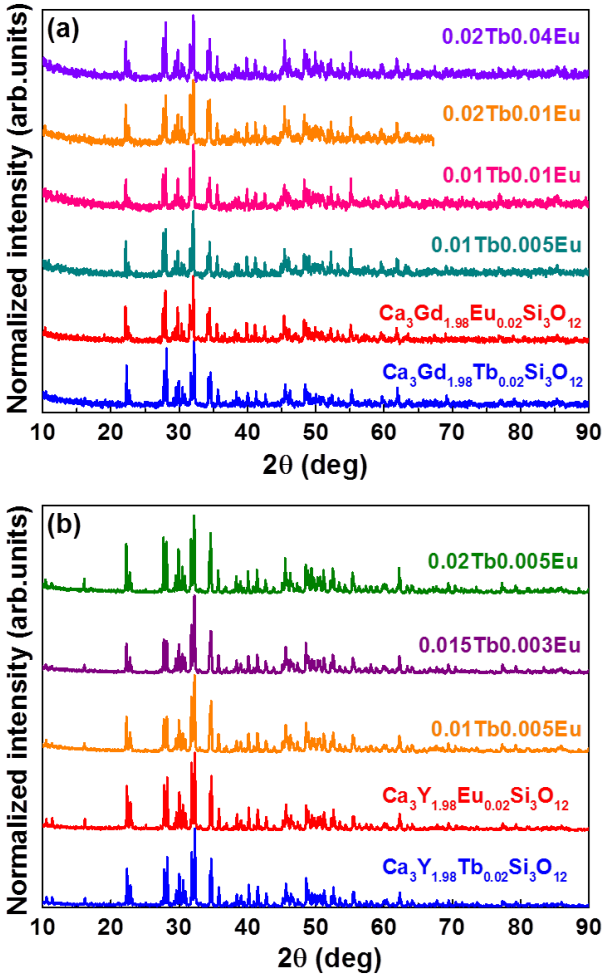

Fig. 4.1. Collected PXRD patterns of the $Ca_3Gd_{2-x-y}Tb_xEu_ySi_3O_{12}$ samples (a) and the $Ca_3Y_{2-x-y}Tb_xEu_ySi_3O_{12}$ samples (b).

Room temperature luminescence spectra and decay curves were measured with a Fluorolog 3 (Horiba-Jobin Yvon) spectrofluorometer, equipped with a Xe lamp, a double excitation monochromator, a single emission monochromator (mod.HR320) and a photomultiplier in photon counting mode for the detection of the emitted signal.

4.3. Results and discussion

4.3.1 $Ca_3Gd_{2-x-y}Tb_xEu_ySi_3O_{12}$

Figure 4.2a shows the room temperature emission spectra of $Ca_3Gd_{1.98}Tb_{0.02}Si_3O_{12}$ measured upon excitation at 377 nm (in $^5D_3$ level of Tb^{3+}) and of $Ca_3Gd_{1.98}Eu_{0.02}Si_3O_{12}$ recorded upon excitation at 393 nm. For $Ca_3Gd_{1.98}Tb_{0.02}Si_3O_{12}$ the emission presents various bands in the ranges 400-480 and 500-650 nm. These bands are due to the $^5D_3 \rightarrow {}^7F_J$ (J = 5, 4, 3) and $^5D_4 \rightarrow {}^7F_J$ (J = 6, 5, 4, 3) transitions. Among them, the $^5D_4 \rightarrow {}^7F_5$ green emission at 542 nm is the most intense. As expected in diluted terbium materials, no quenching of the blue emission is observed. This is because the cross relaxation processes (CR) that transfer population from $^5D_3$ to $^5D_4$, are concentration dependent [8-10], and therefore they are not efficient at low terbium concentration levels. Taking into account that the vibrational cut-off of the $Ca_3Y_2Si_3O_{12}$ silico-carnotite host is about 1050 cm^{-1}, and the energy gap between $^5D_3$ and $^5D_4$ levels is about 5750 cm^{-1} [2], the gap can be bridged by 4-5 phonons. Since for the $Ca_3Gd_2Si_3O_{12}$ host similar vibrational cut-off values are expected, in this system it is possible to populate $^5D_4$ from $^5D_3$ by multiphonon relaxation processes (MPR). The presence of these processes explains the origin of the green emission bands observed in the spectrum measured upon $^5D_3$ excitation. In the case of $Ca_3Gd_{1.98}Eu_{0.02}Si_3O_{12}$ five bands in the 590-730 nm range are observed upon excitation at 393 nm in the $^5L_6$ level. These emission bands correspond to the $^5D_0 \rightarrow {}^7F_J$ (J = 0, 1, 2, 3, 4) transitions of Eu^{3+}, the most intense being the hypersensitive $^5D_0 \rightarrow {}^7F_2$ red emission at 612 nm, as expected due to the distorted geometry of the sites accommodating the impurity [11].

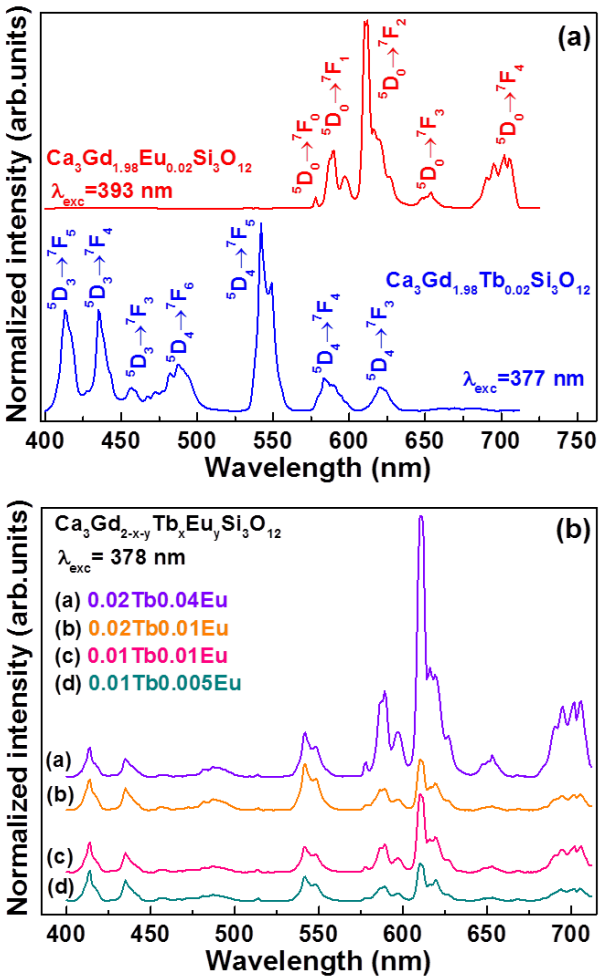

Fig. 4.2. (a) Room temperature emission spectra of $Ca_3Gd_{1.98}Tb_{0.02}Si_3O_{12}$ (λ_{exc} = 377 nm) and $Ca_3Gd_{1.98}Eu_{0.02}Si_3O_{12}$ (λ_{exc} = 393 nm). The spectra are normalized to Tb^{3+} $^5D_4 \rightarrow {}^7F_5$ emission, and Eu^{3+} $^5D_0 \rightarrow {}^7F_2$ emission respectively. (b) Room temperature emission spectra of $Ca_3Gd_{2-x-y}Tb_xEu_ySi_3O_{12}$ measured upon excitation at 378 nm. All spectra are normalized to Tb^{3+} $^5D_3 \rightarrow {}^7F_5$ emission.

In view of these results, it is interesting to consider the possibility of combining the blue, green and red emissions observed in the $Ca_3Gd_2Si_3O_{12}$ phosphors doped with Tb^{3+} and Eu^{3+}. In order to study this phenomenon, a series of $Ca_3Gd_{2-x-y}Tb_xEu_ySi_3O_{12}$ (x = 0.02, y = 0.04; x = 0.02, y = 0.01; x = 0.01, y = 0.01 and x = 0.01, y = 0.005) samples have been prepared. Excitation populates the $^5D_3$ and $^5L_7$ levels of Tb^{3+} and Eu^{3+}, respectively. The emission spectra of the powders (λ_{exc} = 378 nm) are presented in Figure

4.1b. The spectra present various emission bands originating from the $^5D_3$ and $^5D_4$ levels of Tb^{3+} (blue to yellow range), and from the $^5D_0$ level of Eu^{3+} (orange to red range). It is observed that the relative intensities of the $^5D_3 \rightarrow {}^7F_J$ and $^5D_4 \rightarrow {}^7F_J$ transitions do not vary significantly when modifying Tb^{3+} concentration. This is because, as discussed before, the doping levels are low (from 1 to 0.5% mol), so the non-radiative relaxation from $^5D_3$ to $^5D_4$ is not enhanced. The relative intensities of the blue-green bands respect to the red ones, however, are strongly affected by the Tb^{3+}-Eu^{3+} concentration ratio: it is observed that if the concentration of Tb^{3+} is equal or lower than the concentration of Eu^{3+}, the intensity of the red bands is almost double than for blue-green ones. On the contrary, if Tb^{3+} concentration is higher than Eu^{3+}, the relative intensities tend to be identical. Controlling the doping ratio thus allows changing the final emission colour of the material from red to pinkish-white. To clarify this point, the CIE XYZ chromaticity coordinate diagram is shown in Figure 4.3. The values of the CIE coordinates are provided in Table 4.1. For completeness, CIE values for $Ca_3Gd_{1.98}Tb_{0.02}Si_3O_{12}$ and $Ca_3Gd_{1.98}Eu_{0.02}Si_3O_{12}$ are also included.

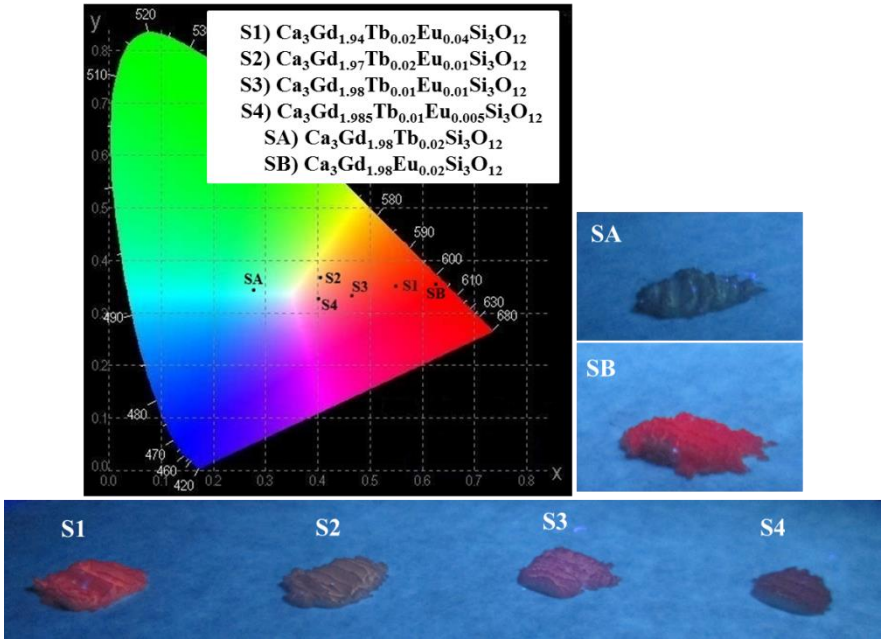

Fig. 4.3. CIE diagram coordinates of $Ca_3Gd_{1.98}Tb_{0.02}Si_3O_{12}$, $Ca_3Gd_{1.98}Tb_{0.02}Si_3O_{12}$ and $Ca_3Gd_{2-x-y}Tb_xEu_ySi_3O_{12}$ excited at 377, 378 and 393 nm respectively, and typical picture of the phosphors when excited at 365 nm with a UV lamp.

For all the compounds, the emission bands are relatively broad due to the structural disorder present in the host, as previously observed in other silico-carnotite materials doped with Tb^{3+} and Eu^{3+} [4].

Table 4.1

Experimental values for the CIE coordinates of $Ca_3Gd_{1.98}Tb_{0.02}Si_3O_{12}$ and $Ca_3Gd_{2-x-y}Tb_xEu_ySi_3O_{12}$ excited at 378 nm and $Ca_3Gd_{1.98}Eu_{0.02}Si_3O_{12}$ excited at 393 nm. Calculated value for CCT of $Ca_3Gd_{1.97}Tb_{0.02}Eu_{0.01}Si_3O_{12}$ powders is also included.

Material	x	y	CCT (K)
$Ca_3Gd_{1.98}Tb_{0.02}Si_3O_{12}$	0.2661	0.3240	--
$Ca_3Gd_{1.98}Eu_{0.02}Si_3O_{12}$	0.6303	0.3582	--
$Ca_3Gd_{1.94}Tb_{0.02}Eu_{0.04}Si_3O_{12}$	0.5502	0.3631	--
$Ca_3Gd_{1.97}Tb_{0.02}Eu_{0.01}Si_3O_{12}$	0.4133	0.3738	3192 (warm white)
$Ca_3Gd_{1.98}Tb_{0.01}Eu_{0.01}Si_3O_{12}$	0.4725	0.3448	--
$Ca_3Gd_{1.985}Tb_{0.01}Eu_{0.005}Si_3O_{12}$	0.4057	0.3300	--

The excitation spectra of all samples are shown in Figure 4.4. The spectrum of $Ca_3Gd_{1.98}Tb_{0.02}Si_3O_{12}$ is composed of overlapping bands in the UV ranging from 300 nm to almost 400 nm, and a band at 480 nm. The transitions have been assigned as $^7F_6 \rightarrow {}^5G_3$ at 340 nm, $^7F_6 \rightarrow {}^5L_8 + {}^5G_4$ at 350 nm, $^7F_6 \rightarrow {}^5D_3$ at 377 nm and $^7F_6 \rightarrow {}^5D_4$ at 480 nm. For the $Ca_3Gd_{2-x-y}Tb_xEu_ySi_3O_{12}$ phosphors, the excitation spectra when monitoring the emission of Tb^{3+} (λ_{emi} = 542 nm) are composed of the same bands observed for $Ca_3Gd_{1.98}Tb_{0.02}Si_3O_{12}$. In the case of the samples with less Tb^{3+} doping, it is possible to observe that the intensity of the $^7F_6 \rightarrow {}^5D_4$ band is comparable to the $^7F_6 \rightarrow {}^5D_3$ band.

The spectrum of $Ca_3Gd_{1.98}Eu_{0.02}Si_3O_{12}$ is composed of various bands ranging from 360 nm to 430 nm and other bands at 460 nm and 530 nm. In this case the transitions have been assigned as $^7F_0 \rightarrow {}^5D_4$ at 360 nm, $^7F_0 \rightarrow {}^3G_3$ and $^7F_0 \rightarrow {}^5L_7$ at 375 and 380 nm $^7F_0 \rightarrow {}^5L_6$ at 393 nm, which it is the most intense, $^7F_0 \rightarrow {}^5D_3$ at 412 nm, $^7F_0 \rightarrow {}^5D_2$ at 460 nm, $^7F_0 \rightarrow {}^5D_1$ at 525 nm and $^7F_1 \rightarrow {}^5D_1$ at 530 nm. In the case of the co-doped samples, the excitation spectra when monitoring the emission of Eu^{3+} (λ_{emi} = 611 nm) present no differences respect to the one observed for $Ca_3Gd_{1.98}Eu_{0.02}Si_3O_{12}$. No clear evidence of Tb^{3+}-Eu^{3+} energy transfer is found in the spectra of these

materials. This can be explained on the basis of the fact that in the co-doped systems the Tb^{3+} and the Eu^{3+} concentrations are low, and then the average distance between Ln^{3+} ions is estimated to lie between 10 and 16 Å, which is larger than the typical critical distance required for electric dipole-electric dipole energy transfer processes involving Tb^{3+} and Eu^{3+} (<10 Å) [12]. Moreover, this implies that there is no fast migration among Tb^{3+} ions. In Chapter 3 it was shown that in silico-carnotite materials, the energy migration in the Tb^{3+} subset plays a relevant role in the Tb^{3+}-Eu^{3+} energy transfer process. Since in the present case Tb^{3+}-Tb^{3+} energy migration is not efficient, the absence of Tb^{3+}-Eu^{3+} energy transfer can be also expected.

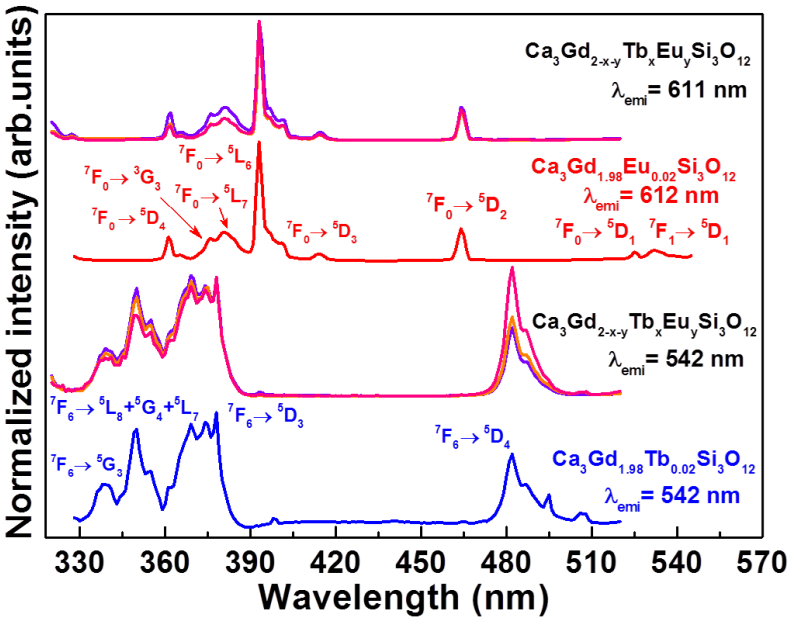

Fig. 4.4. Room temperature excitation spectra of $Ca_3Gd_{1.98}Tb_{0.02}Si_3O_{12}$ (λ_{emi} = 542 nm), $Ca_3Gd_{1.98}Eu_{0.02}Si_3O_{12}$ (λ_{emi} = 612 nm) and $Ca_3Gd_{2-x-y}Tb_xEu_ySi_3O_{12}$ monitoring both emission of Tb^{3+} and Eu^{3+} (λ_{emi}=542 nm, and λ_{emi} = 611 nm). The spectra are normalized to Tb^{3+} $^7F_6 \rightarrow {}^5D_3$ band, and Eu^{3+} $^7F_0 \rightarrow {}^5D_3$ bands respectively.

Decay curves for Tb^{3+} and Eu^{3+} emission were measured upon excitation at 378 nm. Figure 4.5a shows decay curves for Tb^{3+} emission from $^5D_4$ in the various co-doped phosphors (diluted compounds). All the curves are plotted together. To compare the differences, a concentrated Tb^{3+} compound ($Ca_3Tb_2Si_3O_{12}$) is also included. The obtained time constants are reported in Table 4.2, together with the decay constant for

$Ca_3Gd_{1.98}Tb_{0.02}Si_3O_{12}$. In the co-doped phosphors there is a clear rise at short times, which is not present in $Ca_3Tb_2Si_3O_{12}$. As indicated in Chapter 3, this behaviour of $Ca_3Tb_2Si_3O_{12}$ is an effect of the high Tb^{3+} concentration, which allows easy $^5D_3 \rightarrow {}^5D_4$ cross relaxation in Tb^{3+} ions. As it was explained previously, in the co-doped materials there is no migration among Tb^{3+} ions and therefore the observed decay in this case is slow, as energy transfer to killer centres does not occur.

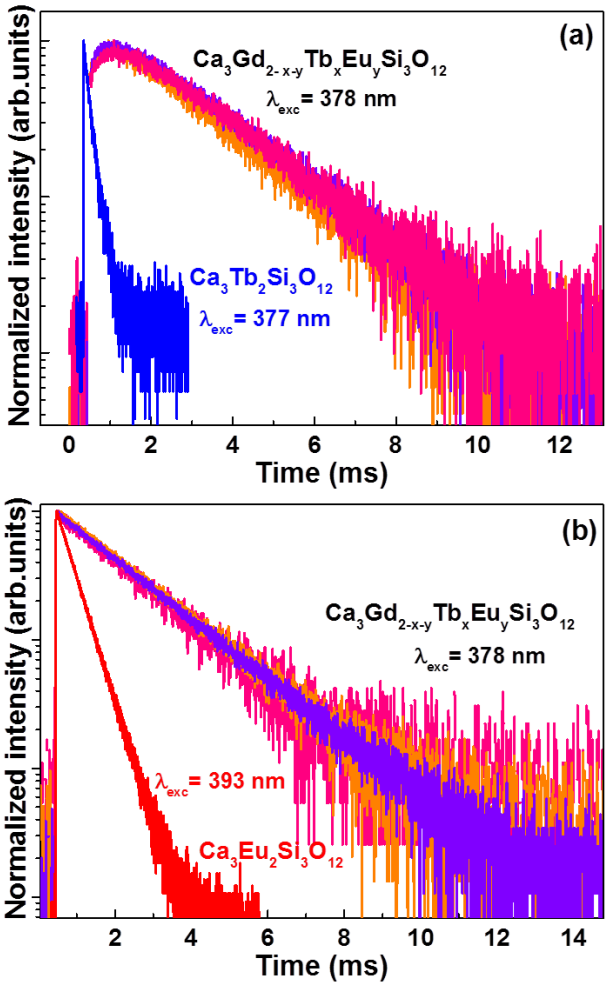

Fig. 4.5. (a) Room temperature decay curves of the $^5D_4$ Tb^{3+} emission excited at 377 nm ($Ca_3Tb_2Si_3O_{12}$) and at 378 nm ($Ca_3Gd_{2-x-y}Tb_xEu_ySi_3O_{12}$). (b) Room temperature decay curves of the $^5D_0$ Eu^{3+} emission excited at 378 nm ($Ca_3Gd_{2-x-y}Tb_xEu_ySi_3O_{12}$) and 393 nm ($Ca_3Eu_2Si_3O_{12}$).

The slow initial build up is due to the MPR processes involved in the population of $^5D_4$, that are slower than the CR processes that are present in $Ca_3Tb_2Si_3O_{12}$. Due to the low levels of doping, the shapes of the curves and the decay constants are not affected by Eu^{3+} concentration. This fact, together with the absence of energy migration in the Tb^{3+} subset and energy transfer from Tb^{3+} to Eu^{3+}, explains why the decay curves present an almost identical behaviour in all the different $Ca_3Gd_{2-x-y}Tb_xEu_ySi_3O_{12}$ phosphors. As a result, the curves appear superimposed in the graph. The decay curves for Tb^{3+} emission from $^5D_3$ (blue bands) have been also measured for $Ca_3Gd_{1.98}Tb_{0.02}Si_3O_{12}$ and the co-doped phosphors. The curves are not exponential due to the presence of structural disorder and possibly some weak energy transfer. Decay constant is in practice not affected by changes in Eu^{3+} concentration, and its value is about 1 ms for all the samples.

Table 4.2

Decay data for the luminescent levels of Tb^{3+} and Eu^{3+} in several oxide hosts upon UV excitation (377-393 nm).

Material	**Excited state (Tb^{3+})**	**Decay time (ms)**	**Excited state (Eu^{3+})**	**Decay time (ms)**
$Ca_3Tb_2Si_3O_{12}$	$^5D_4$	0.18	--	--
$Ca_3Eu_2Si_3O_{12}$	--	--	$^5D_0$	0.44
$Ca_3Gd_{1.98}Tb_{0.02}Si_3O_{12}$	$^5D_4$	2.32 (rise)	--	--
$Ca_3Gd_{1.98}Eu_{0.02}Si_3O_{12}$	--	--	$^5D_0$	1.79
$Ca_3Gd_{1.94}Tb_{0.02}Eu_{0.04}Si_3O_{12}$	$^5D_4$	2.09 (rise)	$^5D_0$	1.85
$Ca_3Gd_{1.97}Tb_{0.02}Eu_{0.01}Si_3O_{12}$	$^5D_4$	2.19 (rise)	$^5D_0$	1.85
$Ca_3Gd_{1.98}Tb_{0.01}Eu_{0.01}Si_3O_{12}$	$^5D_4$	2.25 (rise)	$^5D_0$	1.78
$Ca_3Gd_{1.985}Tb_{0.01}Eu_{0.005}Si_3O_{12}$	$^5D_4$	2.06 (rise)	$^5D_0$	1.80

Figure 4.5b presents the decay curves for the Eu^{3+} $^5D_0$ emission for the various co-doped samples. All the curves are plotted together. $Ca_3Eu_2Si_3O_{12}$ is also included to compare the behaviour of the ion. The time constants obtained from the decay curves are also reported in Table 4.2. For the Eu^{3+}-doped samples, the curves are well fitted by a single exponential function. This behaviour is explained because there is no energy transfer from Tb^{3+} to Eu^{3+} and thanks to the fast relaxation from the excited level ($^5L_7$ (λ_{exc} = 378 nm) for the diluted compounds, $^5L_6$ (λ_{exc} = 393 nm) for the concentrated sample) to $^5D_0$ due to the small energy gaps between the

intermediate levels, which require less than three phonons to be bridged. In the case of $Ca_3Eu_2Si_3O_{12}$, decay time is shortened, presumably due to concentration quenching as a result of energy migration to quenching impurities. No significant changes are observed when varying Eu^{3+} concentration in the diluted samples. All the curves present an almost identical behaviour, and therefore they appear superimposed in the graph.

Luminescence experiments upon excitation into Gd^{3+} have been also performed as a complementary tool in the study of the $Ca_3Gd_2Si_3O_{12}$:Tb-Eu system. Figure 4.6a presents the emission spectra of $Ca_3Gd_{1.98}Tb_{0.02}Si_3O_{12}$ and $Ca_3Gd_{1.98}Eu_{0.02}Si_3O_{12}$ upon excitation at 273 nm. For both materials the spectra are almost identical to those measured at 377 and 378 nm respectively, which indicates the existence of an efficient energy transfer process from Gd^{3+} to Tb^{3+} and Eu^{3+}. The emission spectra of the $Ca_3Gd_{2-x-y}Tb_xEu_ySi_3O_{12}$ powders upon 274 nm excitation are shown in Figure 4.6b. Also in this case, no significant differences on the shape or the position of the peaks can be observed with respect to the spectra presented in Figure 4.2. For the $Ca_3Gd_{1.98}Tb_{0.02}Si_3O_{12}$ and $Ca_3Gd_{2-x-y}Tb_xEu_ySi_3O_{12}$ powders it is possible to observe an additional band at 380 nm which corresponds to the $^5D_3 \rightarrow {}^7F_6$ Tb^{3+} transition. Energy transfer processes in Gd-based compounds that involve Tb^{3+} and Eu^{3+} are well known and documented [13, 14], and it is generally assumed that the excitation energy migrates through the gadolinium subnet until it reaches a dopant ion. With this idea, it is conceivable to think that in the materials under analysis there is a fast Gd^{3+}-Gd^{3+} migration, followed by energy transfer from gadolinium to high energy levels of terbium and europium. As discussed previously, fast relaxation from these high energy levels to the $^5D_3$ and $^5D_0$ emitting levels of Tb^{3+} and Eu^{3+} respectively, takes place due to the small energy gaps between the intermediate levels. In view of these facts, all the considerations discussed previously regarding the emission features of both Tb^{3+} and Eu^{3+} ions in these materials apply also in this case. The CIE XYZ chromaticity coordinate diagram is shown in Figure 4.7. The calculated values of CIE coordinates are provided in Table 4.3.

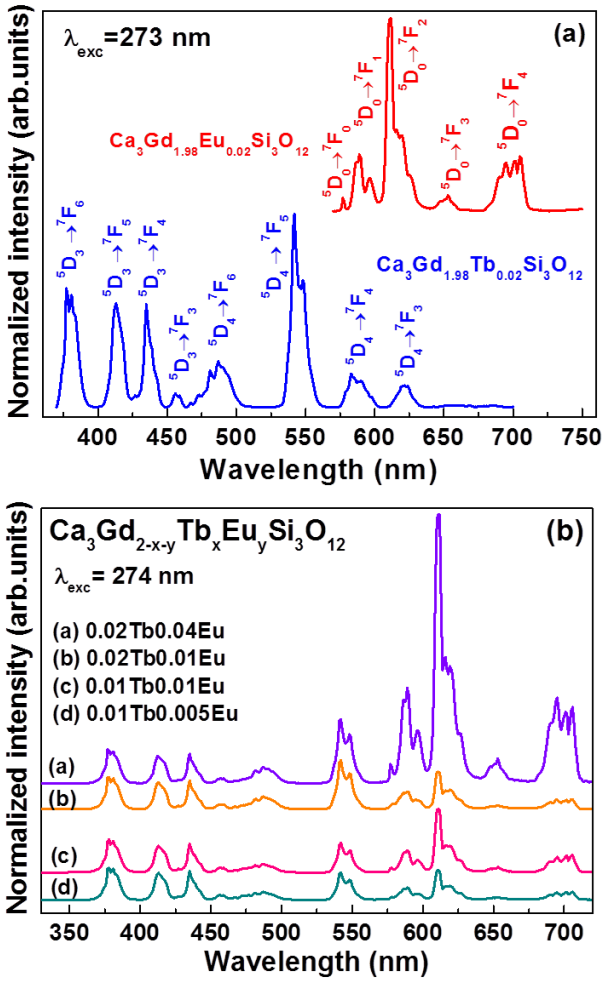

Fig. 4.6. (a) Room temperature emission spectra of $Ca_3Gd_{1.98}Tb_{0.02}Si_3O_{12}$ and $Ca_3Gd_{1.98}Eu_{0.02}Si_3O_{12}$ upon excitation at 273 nm. The spectra are normalized to Tb^{3+} $^5D_4 \rightarrow {}^7F_5$ emission, and Eu^{3+} $^5D_0 \rightarrow {}^7F_2$ emission respectively. (b) Room temperature emission spectra of $Ca_3Gd_{2-x-y}Tb_xEu_ySi_3O_{12}$ measured upon excitation at 274 nm. All spectra are normalized to Tb^{3+} $^5D_3 \rightarrow {}^7F_5$ emission.

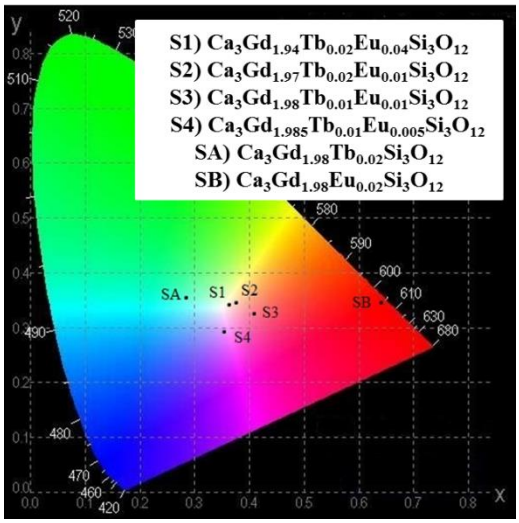

Fig. 4.7. CIE diagram coordinates of $Ca_3Gd_{1.98}Tb_{0.02}Si_3O_{12}$, $Ca_3Gd_{2-x-y}Tb_xEu_ySi_3O_{12}$ and $Ca_3Gd_{1.98}Eu_{0.02}Si_3O_{12}$ excited at 273, 274 and 273 nm respectively.

Table 4.3

Obtained values for the CIE coordinates of $Ca_3Gd_{1.98}Tb_{0.02}Si_3O_{12}$ and $Ca_3Gd_{1.98}Eu_{0.02}Si_3O_{12}$ excited at 273 nm $Ca_3Gd_{2-x-y}Tb_xEu_ySi_3O_{12}$ excited at 274 nm. Calculated value for the corresponding CCT of $Ca_3Gd_{1.97}Tb_{0.02}Eu_{0.01}Si_3O_{12}$ powders is also included.

Material	x	y	CCT (K)
$Ca_3Gd_{1.98}Tb_{0.02}Si_3O_{12}$	0.2815	0.3660	--
$Ca_3Gd_{1.98}Eu_{0.02}Si_3O_{12}$	0.6455	0.3545	--
$Ca_3Gd_{1.94}Tb_{0.02}Eu_{0.04}Si_3O_{12}$	0.3609	0.3526	4440 (cool white)
$Ca_3Gd_{1.97}Tb_{0.02}Eu_{0.01}Si_3O_{12}$	0.3723	0.3532	4077 (natural white)
$Ca_3Gd_{1.98}Tb_{0.01}Eu_{0.01}Si_3O_{12}$	0.4192	0.3150	--
$Ca_3Gd_{1.985}Tb_{0.01}Eu_{0.005}Si_3O_{12}$	0.3529	0.2961	--

Figure 4.8 presents the excitation spectra of all samples (including $Ca_3Gd_{1.98}Tb_{0.02}Si_3O_{12}$ and $Ca_3Gd_{1.98}Eu_{0.02}Si_3O_{12}$, even if it is not explicitly indicated) in the range 260-520 nm. Broadening the range with respect to the spectra of Figure 4.4 allows to observe two groups of sharp and intense bands at around 270 and 315 nm, that dominate the spectra in all cases. These bands are assigned to the $^8S_{7/2} \rightarrow {}^6I$ and $^8S_{7/2} \rightarrow {}^6P$ transitions of Gd^{3+}, as indicated in the figure. It is possible to notice that for the Tb^{3+} emission at

542 nm (Figure 4.8a) the intensity of terbium bands with respect to gadolinium ones is less than in the case of europium, which excitation bands are comparable or even higher in some cases than the corresponding $^8S_{7/2} \rightarrow {}^6P$ Gd^{3+} bands (Figure 4.8b). It is also possible to observe the tail of the europium charge-transfer band overlapping with the gadolinium excitation bands (instrumental limitations prevent measuring the complete band).

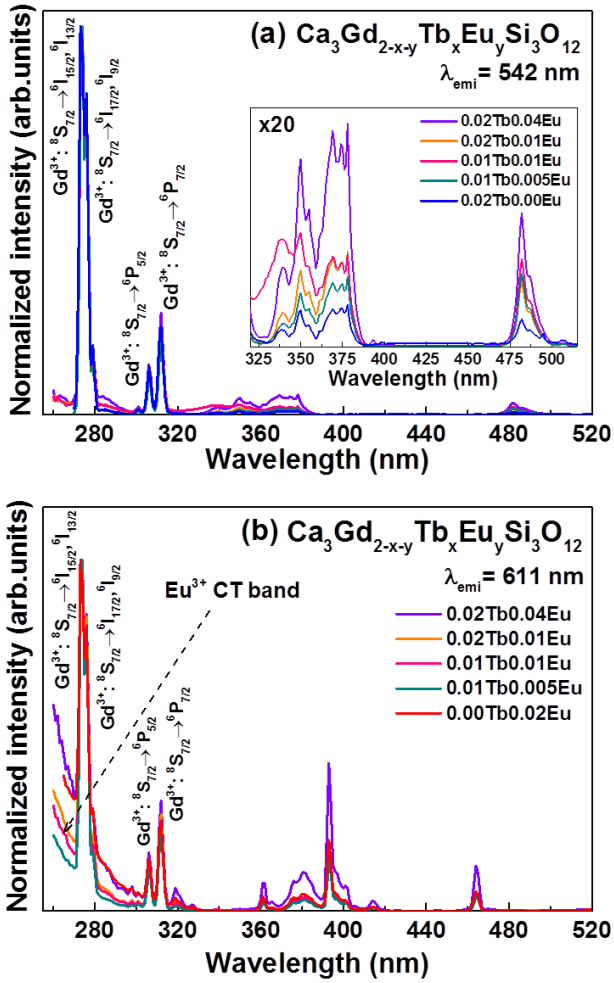

Fig. 4.8. Room temperature excitation spectra of the $Ca_3Gd_{2-x-y}Tb_xEu_ySi_3O_{12}$ powders monitoring emission of Tb^{3+} at 542 nm (a), and emission of Eu^{3+} at 611 nm. The spectra are normalized to Gd^{3+} $^8S_{7/2} \rightarrow {}^6I$.

Decay curves for Tb^{3+} and Eu^{3+} emission were measured for $Ca_3Gd_{1.98}Tb_{0.02}Si_3O_{12}$ and $Ca_3Gd_{1.98}Eu_{0.02}Si_3O_{12}$ samples upon excitation at 273 nm. Figure 4.9a shows decay curves for Tb^{3+} emission from $^5D_4$ and Eu^{3+} emission from $^5D_0$. As observed before, in the case of terbium there is a clear rise at short times as a result of the $^5D_3 \rightarrow {}^5D_4$ MPR process.

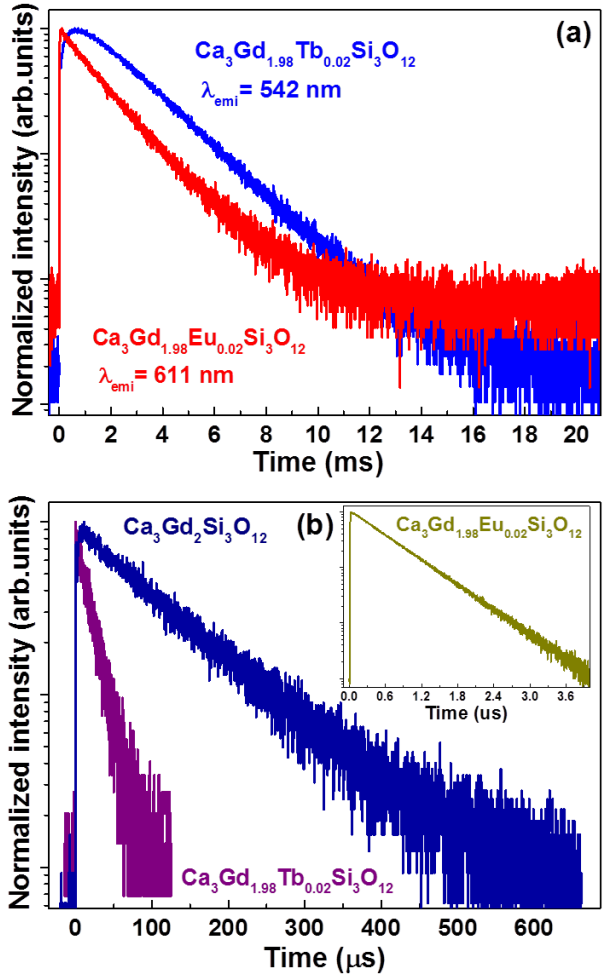

Fig. 4.9. (a) Room temperature decay curves of the $^5D_4$ Tb^{3+} emission and the $^5D_0$ Eu^{3+} excited at 273 nm for $Ca_3Gd_{1.98}Tb_{0.02}Si_3O_{12}$ and $Ca_3Gd_{1.98}Eu_{0.02}Si_3O_{12}$. (b) Room temperature decay curves of the $^6P_{7/2}$ Gd^{3+} emission excited at 273 nm in $Ca_3Gd_2Si_3O_{12}$, $Ca_3Gd_{1.98}Tb_{0.02}Si_3O_{12}$ and $Ca_3Gd_{1.98}Eu_{0.02}Si_3O_{12}$ (inset).

In the case of europium no build up is observed, which indicates that the Gd^{3+}-Eu^{3+} transfer and the subsequent relaxation from higher levels to

$^5D_0$ are fast. The time constants extracted from the curves are reported in Table 4.4. In this case, both the terbium and the europium curves are not exponential, possibly due to the presence of structural disorder. Moreover, it is conceivable that the distribution of Tb^{3+} and Eu^{3+} ions that are excited in this case is not the same respect to the case of direct excitation at 378 nm.

Figure 4.9b presents the decay curves of Gd^{3+} for the 312 nm emission in $Ca_3Gd_2Si_3O_{12}$, $Ca_3Gd_{1.98}Tb_{0.02}Si_3O_{12}$ and $Ca_3Gd_{1.98}Eu_{0.02}Si_3O_{12}$ (inset). The measured curves for the doped materials are well fitted by a single exponential function, whereas in the case of $Ca_3Gd_2Si_3O_{12}$ the curve is slightly non-exponential. The obtained time constants are also reported in Table 4.4. The decay constant for the Tb^{3+} and Eu^{3+}-doped samples are significantly shortened respect with the one calculated for the neat Gd compound, especially for the Eu^{3+}-doped sample.

Table 4.4

Decay data for the luminescent levels of Tb^{3+} and Eu^{3+} in several yttrium hosts upon UV excitation.

Material	Excited state	Decay time
$Ca_3Gd_{1.98}Tb_{0.02}Si_3O_{12}$	$^5D_4$ (Tb^{3+})	2.21 ms (rise)
$Ca_3Gd_{1.98}Eu_{0.02}Si_3O_{12}$	$^5D_0$ (Eu^{3+})	1.68 ms
$Ca_3Gd_2Si_3O_{12}$	$^6P_{7/2}$ (Tb^{3+})	107 μs
$Ca_3Gd_{1.98}Tb_{0.02}Si_3O_{12}$	$^6P_{7/2}$ (Tb^{3+})	19.7 μs
$Ca_3Gd_{1.98}Eu_{0.02}Si_3O_{12}$	$^6P_{7/2}$ (Tb^{3+})	0.6 μs

The efficiencies of the Gd^{3+}-Tb^{3+} and Gd^{3+}-Eu^{3+} energy transfer processes have been estimated from the experimental decay constants as described previously on Chapter 3 for the Tb^{3+}-Eu^{3+} energy transfer (equation 3.4). In both cases high values of the efficiency have been obtained.

4.3.2 $Ca_3Y_{2-x-y}Tb_xEu_ySi_3O_{12}$

Due to the interesting properties observed for the gadolinium-based phosphors, it is worth to explore other similar hosts starting from these

results. In the present section the luminescence of various yttrium-based silico-carnotite are discussed.

Figure 4.10a shows the room temperature emission spectra of $Ca_3Y_{1.98}Tb_{0.02}Si_3O_{12}$ measured upon excitation at 378 nm (in $^5D_3$ level of Tb^{3+}) and the emission spectrum of $Ca_3Y_{1.98}Eu_{0.02}Si_3O_{12}$ recorded upon excitation at 393 nm. In both cases, the spectra are similar to the ones presented in the previous section for the gadolinium-based samples. In the case of $Ca_3Y_{1.98}Tb_{0.02}Si_3O_{12}$, the emission spectrum presents various bands in the ranges of 400-480 and 500-650 nm, the most intense being the $^5D_4 \rightarrow {}^7F_5$ green emission at 542 nm. These results include the blue emission originating from the $^5D_3$ level, which was erroneously not shown and discussed in ref. [2]. In the case of $Ca_3Y_{1.98}Eu_{0.02}Si_3O_{12}$ five bands in the 590-730 nm range are observed. The most intense is the $^5D_0 \rightarrow {}^7F_2$ red emission at 612 nm. The changes of the structure due to the presence of one metal cation or another, *i.e.* the difference in the site distribution of Ca^{2+} and Ln^{3+} (including the luminescent dopant ones), lead to small differences of the average crystal field of the cations in each material [15]. These variations are responsible for the small changes observed in the blue/green (B/G) and orange/red (O/R) ratios of Tb^{3+} and Eu^{3+} emissions respectively, thus affecting the emission colour of the material. In Table 4.5 the B/G and O/R ratios estimated from the spectra for both gadolinium and yttrium-based compounds are presented.

Table 4.5

Experimental values for B/G and O/R ratios for the $Ca_3A_{1.98}Tb_{0.02}Si_3O_{12}$ (A = Gd, Y), $Ca_3A_{1.98}Eu_{0.02}Si_3O_{12}$ (A = Gd, Y) phosphors.

Material	B/G ratio	O/R ratio
$Ca_3Gd_{1.98}Tb_{0.02}Si_3O_{12}$	1.69	--
$Ca_3Gd_{1.98}Eu_{0.02}Si_3O_{12}$	--	0.54
$Ca_3Y_{1.98}Tb_{0.02}Si_3O_{12}$	0.91	--
$Ca_3Y_{1.98}Eu_{0.02}Si_3O_{12}$	--	0.36

Starting from the results obtained for the gadolinium silico-carnotite, a series of $Ca_3Y_{2-x-y}Tb_xEu_ySi_3O_{12}$ (x = 0.02, y = 0.005; x = 0.015, y = 0.003 and x = 0.01, y = 0.005) samples have been prepared. The emission spectra of the powders (λ_{exc} = 378 nm) are presented in Fig. 4.10b. As it was

observed for the gadolinium-based phosphors, the spectra present emission bands originating from the $^5D_3$ and $^5D_4$ levels of Tb^{3+} (blue to yellow range), and from the $^5D_0$ level of Eu^{3+} (orange to red range).

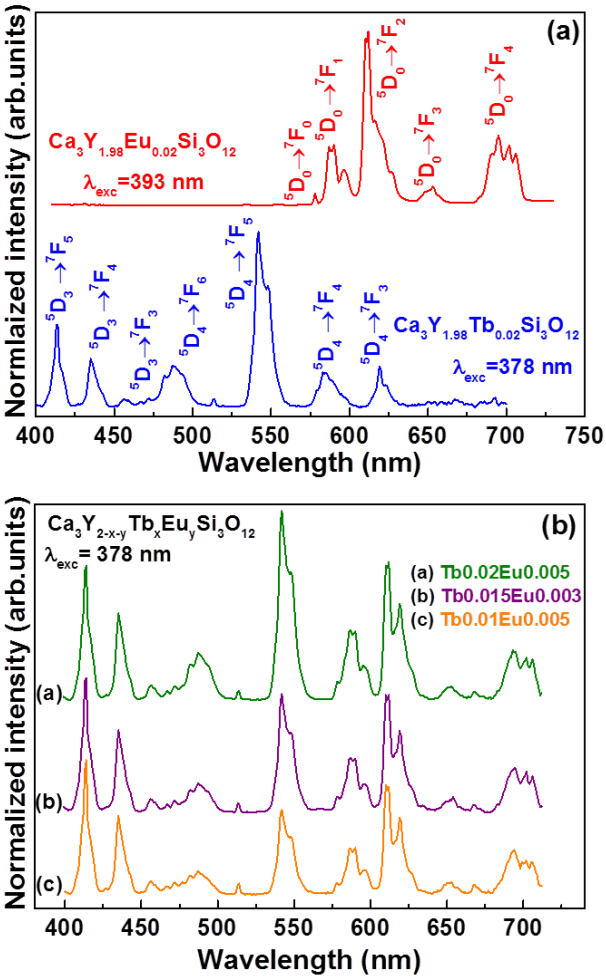

Fig. 4.10. (a) Room temperature emission spectra of $Ca_3Y_{1.98}Tb_{0.02}Si_3O_{12}$ (λ_{exc} = 377 nm) and $Ca_3Y_{1.98}Eu_{0.02}Si_3O_{12}$ (λ_{exc} = 393 nm). The spectra are normalized to Tb^{3+} $^5D_4 \rightarrow {}^7F_5$ emission, and Eu^{3+} $^5D_0 \rightarrow {}^7F_2$ emission respectively. (b) Room temperature emission spectra of $Ca_3Y_{2-x-y}Tb_xEu_ySi_3O_{12}$ measured upon excitation at 378 nm. All spectra are normalized to Tb^{3+} $^5D_3 \rightarrow {}^7F_5$ emission.

The CIE XYZ chromaticity coordinates diagram is shown in Figure 4.11. The values of the CIE coordinates are reported in Table 4.6. As done before and for completeness, CIE values for $Ca_3Y_{1.98}Tb_{0.02}Si_3O_{12}$ and

$Ca_3Y_{1.98}Eu_{0.02}Si_3O_{12}$ are also included in both diagram and table. In this case, control over the doping ratio allows obtaining a final emission colour that varies from pinkish-white to yellowish-white in the co-doped materials.

Table 4.6

Experimental values for the CIE coordinates of $Ca_3Y_{1.98}Tb_{0.02}Si_3O_{12}$ and $Ca_3Y_{2-x-y}Tb_xEu_ySi_3O_{12}$ excited at 378 nm and $Ca_3Y_{1.98}Eu_{0.02}Si_3O_{12}$ excited at 393 nm. Calculated values for the corresponding CCT of $Ca_3Y_{1.982}Tb_{0.015}Eu_{0.003}Si_3O_{12}$ and $Ca_3Y_{1.985}Tb_{0.01}Eu_{0.005}Si_3O_{12}$ powders are also included.

Material	x	y	CCT (K)
$Ca_3Y_{1.98}Tb_{0.02}Si_3O_{12}$	0.3164	0.4351	--
$Ca_3Y_{1.98}Eu_{0.02}Si_3O_{12}$	0.6007	0.3495	--
$Ca_3Y_{1.975}Tb_{0.02}Eu_{0.005}Si_3O_{12}$	0.3856	0.3751	--
$Ca_3Y_{1.982}Tb_{0.015}Eu_{0.003}Si_3O_{12}$	0.3900	0.3409	3438 (warm white)
$Ca_3Y_{1.985}Tb_{0.01}Eu_{0.005}Si_3O_{12}$	0.3891	0.3203	3226 (warm white)

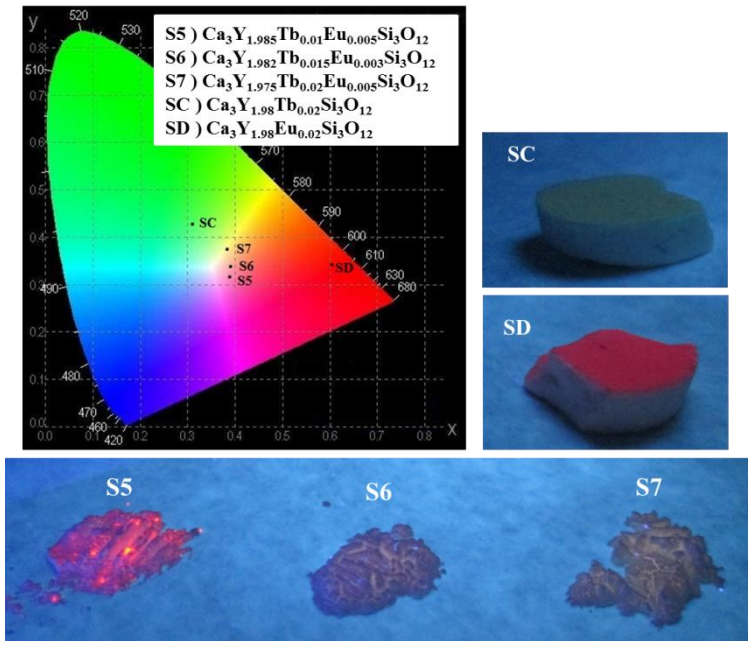

Fig. 4.11. CIE diagram coordinates of $Ca_3Y_{1.98}Tb_{0.02}Si_3O_{12}$, $Ca_3Y_{1.98}Tb_{0.02}Si_3O_{12}$ and $Ca_3Y_{2-x-y}Tb_xEu_ySi_3O_{12}$ excited at 377, 378 and 393 nm respectively, and typical picture of the phosphors when excited at 365 nm with a UV lamp.

Figure 4.12 shows the excitation spectra of all samples. As it can be observed, the spectra present no significant differences from the ones measured for the gadolinium-based materials. Also in this case, no clear evidence of Tb^{3+}-Eu^{3+} energy transfer process has been found. The same considerations made for the gadolinium phosphors apply here.

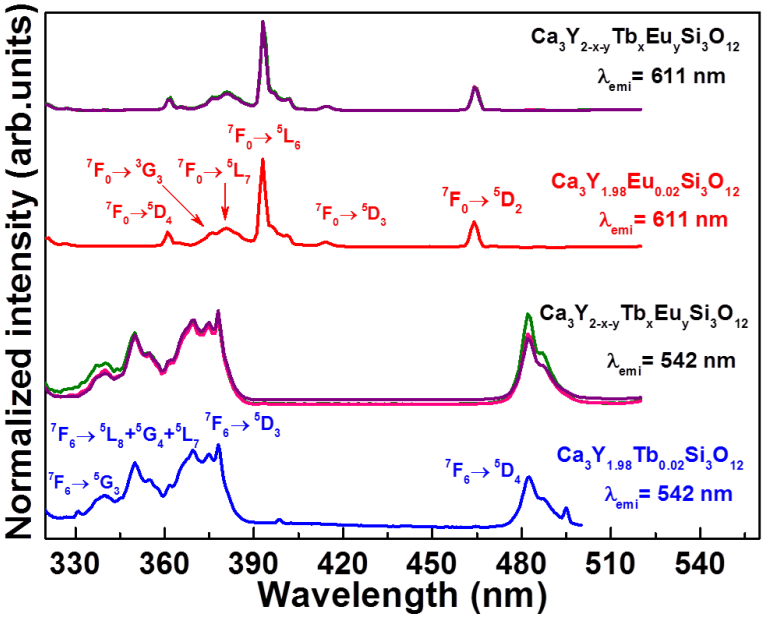

Fig. 4.12. Room temperature excitation spectra of $Ca_3Y_{1.98}Tb_{0.02}Si_3O_{12}$ (λ_{emi} = 542 nm), $Ca_3Y_{1.98}Eu_{0.02}Si_3O_{12}$ (λ_{emi} = 612 nm) and $Ca_3Y_{2-x-y}Tb_xEu_ySi_3O_{12}$ monitoring both emission of Tb^{3+} and Eu^{3+} (λ_{emi}=542 nm, and λ_{emi} = 611 nm). The spectra are normalized to Tb^{3+} $^7F_6 \rightarrow {}^5D_3$ band, and Eu^{3+} $^7F_0 \rightarrow {}^5D_3$ band respectively.

Figure 4.13 shows the decay curves for Tb^{3+} and Eu^{3+} emission measured upon excitation at 378 nm. Also in this case, concentrated Tb^{3+} and Eu^{3+} compounds are included in the graph. The obtained time constants are reported in Table 4.7. In the co-doped phosphors there is a clear rise at short times in the decay curves for Tb^{3+} emission from $^5D_4$, as observed in the gadolinium samples, and the decay constant is also much longer than in concentrated Tb^{3+} systems. Since in these compounds the Tb^{3+} concentration is also low, all the considerations discussed in the case of the gadolinium host apply in this case. The decay curves for Tb^{3+} emission from $^5D_3$ have been also measured. As observed previously for the gadolinium phosphors, curves are not exponential and the decay constant is

about 1 ms. Again, and due to the low levels of doping, decay constant is not affected by Eu^{3+} concentration (not for blue or green emission).

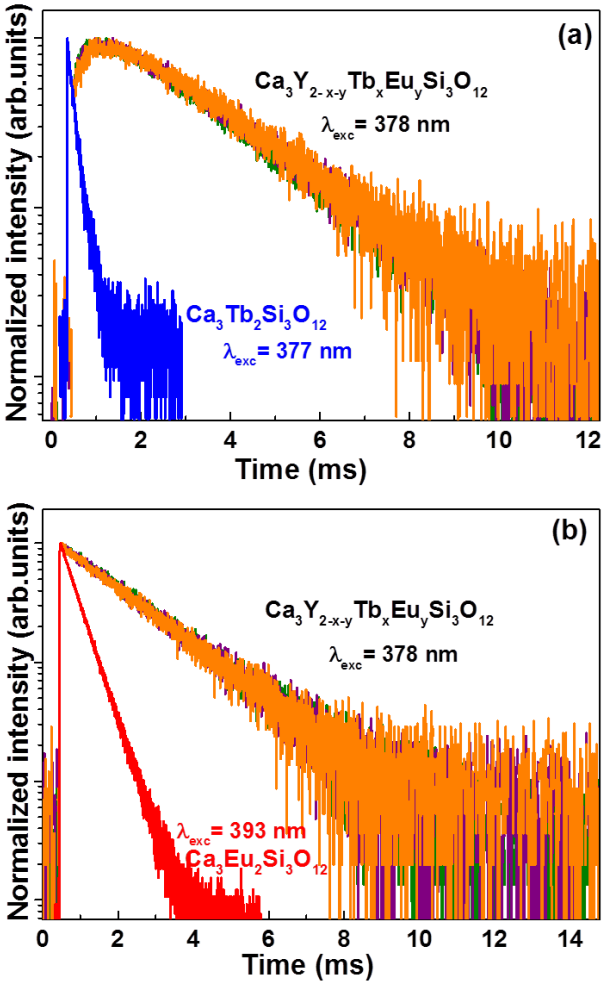

Fig. 4.13. (a) Room temperature decay curves of the $^5D_4$ Tb^{3+} emission excited at 377 nm ($Ca_3Tb_2Si_3O_{12}$) and at 378 nm ($Ca_3Y_{2-x-y}Tb_xEu_ySi_3O_{12}$). (b) Room temperature decay curves of the $^5D_0$ Eu^{3+} emission excited at 378 nm ($Ca_3Y_{2-x-y}Tb_xEu_ySi_3O_{12}$) and 393 nm ($Ca_3Eu_2Si_3O_{12}$).

Regarding decay curves for Eu^{3+} $^5D_0$ emission for the co-doped samples, the curves are also well fitted by a single exponential function, and the time constants extracted from them are similar to the obtained for the gadolinium phosphors. The values are reported in Table 4.7. As well as it

was observed before, there are no significant changes when varying Eu^{3+} concentration.

Table 4.7

Decay data for the luminescent levels of Tb^{3+} and Eu^{3+} in several yttrium hosts upon UV excitation.

Material	Excited state (Tb^{3+})	Decay time (ms)	Excited state (Eu^{3+})	Decay time (ms)
$Ca_3Y_{1.98}Tb_{0.02}Si_3O_{12}$	$^5D_4$	2.28 (rise)	--	--
$Ca_3Y_{1.98}Eu_{0.02}Si_3O_{12}$	--	--	$^5D_0$	1.88
$Ca_3Y_{1.94}Tb_{0.02}Eu_{0.05}Si_3O_{12}$	$^5D_4$	2.23 (rise)	$^5D_0$	1.87
$Ca_3Y_{1.982}Tb_{0.015}Eu_{0.003}Si_3O_{12}$	$^5D_4$	2.25 (rise)	$^5D_0$	1.85
$Ca_3Y_{1.98}Tb_{0.01}Eu_{0.05}Si_3O_{12}$	$^5D_4$	2.29 (rise)	$^5D_0$	1.85

4.4. Conclusions

In this chapter the luminescence spectra and decay curves of several $Ca_3Gd_{2-x-y}Tb_xEu_ySi_3O_{12}$ and $Ca_3Y_{2-x-y}Tb_xEu_ySi_3O_{12}$ powders have been systematically studied. Experiments for various Tb^{3+} and Eu^{3+} doping, and co-doping concentration have been performed. The obtained results indicate that the $^5D_4$ level can be populated from $^5D_3$ via a multiphonon relaxation process while $^5D_3$-$^5D_4$ cross relaxation does not pay a relevant role. Therefore, in this case quenching of blue emission is avoided. No evidence of Tb^{3+}-Eu^{3+} energy transfer process has been found in any of the co-doped systems as a result of the low doping levels, that do not favour the Tb^{3+}-Tb^{3+} energy migration, nor direct Tb^{3+}-Eu^{3+} transfer. However, evidence of efficient Gd^{3+}-Tb^{3+} and Gd^{3+}-Eu^{3+} energy transfer processes has been found in the $Ca_3Gd_{2-x-y}Tb_xEu_ySi_3O_{12}$ samples. The efficiency of the transfer at room temperature estimated from the experimental decay times is high for both Gd^{3+}-Tb^{3+} and Gd^{3+}-Eu^{3+} energy transfer processes. These features indicated that, in both cases, the Gd^{3+} emission is almost quenched while Tb^{3+} and Eu^{3+} emissions are enhanced.

The obtained results show that for the present samples the emission colour strongly depends on the Tb^{3+}-Eu^{3+} ratio, and not on the total doping

concentration of each ion. Controlling the doping ratio leads to close-to-white emission in various silico-carnotite compounds, opening an interesting opportunity in the search for novel phosphors for white-LED excited in the UV.

References

[1] Y. Liu, J. Zhang, C. Zhang, J. Jiang, H. Jiang, *J. Phys. Chem. C* 120, (2016) 2362-2370.

[2] F. Piccinelli, A. Speghini, G. Mariotto, L. Bovo, M. Bettinelli, *J. Rare Earths* 27 (2009) 555-559.

[3] F. Piccinelli, A. Lausi and M. Bettinelli, *J. Solid State Chem.* 205 (2013) 190-196.

[4] I. Carrasco, K. Bartosiewicz, M. Nikl, F. Piccinelli, M. Bettinelli, *Opt. Mater.* 48 (2015) 252-257.

[5] B. Dickens and W. E. Brown, *Tschermaks Mineral. Petrogr. Mitt.* 16 (1971) 1-27.

[6] G.A. Novak, G.V. Gibbs, *Am. Mineral.* 56 (1971) 791-825.

[7] F. Piccinelli, A. Lausi, A. Speghini, M. Bettinelli, *J. Solid State Chem.* 194 (2012) 233-237.

[8] F. Auzel, J. Dexpert-Ghys, D. Morin, G. Dadoun, J. Ostorero, H. Makram, *Mater. Res. Bull.* 16 (1981)1521.

[9] J.F.M. dos Santos, I.A.A. Terra, N.G.C. Astrath, F.B. Guimaraes, M.L. Baesso, L.A.O. Nunes, T. Catunda, *J. Appl. Phys.* 117 (2015) 053102.

[10] Z. Hao, J. Shang, X. Zhang, S. Lu, Z. Wang, *J. Electrochem. Soc.* 156 (3) (2009) H193-H196.

[11] F. Piccinelli, A. Speghini, M. Bettinelli, *Opt. Mat.* 35 (2013) 2027-2029.

[12] M. Bettinelli, F. Piccinelli, A. Speghini, J. Ueda, S. Tanabe, *J. Lum.* 132 (2012) 27-29.

[13] G. Blasse, G.P.M. Van den Heuvel, T. Van Dijk, *Chem. Phys. Lett* 62 (3) (1979) 600-602.

[14] M.L. Debasu, D. Ananias, J. Rocha, O.L. Malta, L.D. Carlos, *Phys. Chem. Chem. Phys*. 15 (2013) 15565.

[15] T. Hoshina, *Jap. J. Appl. Phys.* 6 (10) (1967) 1203-1211.

Chapter 5

Structural and spectroscopic features of whitlockite $Ca_9M(PO_4)_7$ ($M = Al^{3+}, Lu^{3+}$) powders activated with Pr^{3+} ions

In this chapter the structural and spectroscopic properties of $Ca_9M(PO_4)_7$ (M = Al, Lu) whitlockite compounds doped with Pr^{3+} ions are presented. The Al-based samples were prepared by the citrate route, while the Lu-based ones were prepared by standard solid state reaction. The structural properties were investigated by XRD measurements and Rietveld analysis. Detailed spectroscopic properties like emission and excitation spectra, luminescence kinetics and luminescence temperature quenching were measured to determine the influence of the different trivalent host metal cations on the Pr^{3+} ions. Pr^{3+} enters in the three Ca^{2+} sites in $Ca_9Al(PO_4)_7$, creating some defect to compensate the charge mismatch, whereas in $Ca_9Lu(PO_4)_7$ occupies four Ca^{2+}/Lu^{3+} sites, and no charge compensation is needed. The emission spectra are similar in both materials. Efficient quenching of the $^1D_2$ emission was observed, while the $^3P_0$ emission remains stable for all dopant concentrations. Decay times were found to be non-single exponential due to the occupation of different sites by Pr^{3+} ions. The luminescence temperature quenching measurements have revealed that two different mechanisms (multiphonon relaxation and cross relaxation processes) are responsible for the emission quenching.

5.1. Introduction

Phosphate-based inorganic compounds are still the subject of extensive research studies, particularly as hosts for luminescent ions. The rhombohedral $Ca_3(PO_4)_2$ with space group *R3c* is isostructural with all the materials possessing whitlockite structure. The number of formula units is 21 and in the hexagonal setting [1] five distinct Ca^{2+} sites (namely M1-M5) with coordination number ranging from 6 (for M4 and M5) to 8 (for M1, M2 and M3) are present. The distorted octahedral M5 sites are fully occupied by Ca^{2+} ions, whereas M4 positions are half occupied in a statistical way ($Ca^{2+}\square$, where □ is the vacancy position) [2]. The substitution of a proper amount of Ca^{2+} with R = RE^{3+}, Al^{3+}, Ga^{3+}, Bi^{3+} (RE^{3+} are rare earth ions), Mg^{2+} or Na^{+} ions leads to a similar cell with the same space group, but with six $Ca_9R(PO_4)_7$ (or $CaMgNa(PO_4)_7$ [3]) formula units. In these compounds, the M4 site must be empty for charge neutrality. Whitlockites, described by the general chemical formula $Ca_9R(PO_4)_7$ R = RE^{3+}, Al^{3+}, Ga^{3+}, Bi^{3+}, present outstanding luminescence properties when doped with optically active ions [4-8].

$Ca_9Al(PO_4)_7$ crystallizes in the trigonal *R3c* (161) space group [9]. The isolated units of $[PO_4]^{3-}$ are separated by $[CaO_9]^{16-}$, $[CaO_8]^{14-}$ or $[CaO_6]^{10-}$ polyhedra [8]. It is possible to distinguish three different calcium sites with the same point symmetry C_1, available for possible substitution with rare earth cations. M1 and M2 sites have eigth-fold coordination whereas M3 has nine-fold coordination. Du *et al*. [4] have shown that the distribution of the Eu^{3+} cations in the $Ca_9Al(PO_4)_7$ lattice is statistical among the three available sites. Since the Eu^{3+} is very useful as a structural probe, many of the structural features can be evaluated on the basis of only the emission spectra and the characteristic behavior of its intraconfigurational 4f→4f transitions. $Ca_9Lu(PO_4)_7$ is isostructural with $Ca_9Al(PO_4)_7$, but in this case Ca^{2+} and Lu^{3+} ions share four crystal sites: the above mentioned M1, M2, M3, and a six-fold coordination site (M5). Lu^{3+} ions show a preference for M5 and M1 (occupancy factors: M1 = 0.173, M5 = 0.237) [10].

The Pr^{3+} luminescence properties are extremely interesting in many optical applications. It is possible to obtain different optical emission spectra depending on the type of crystal host or the Pr^{3+} concentration. In particular, the interplay of the two main radiative transitions from $^1D_2$ and

$^3P_0$ to the $^3H_4$ ground level (red and greenish-blue emission), are strongly affected by non-radiative processes governed by the dopant concentration and the vibrational properties of the given host.

The present chapter is focused on the synthesis, structural and spectroscopic investigation of Pr^{3+}-doped $Ca_9Al(PO_4)_7$ and $Ca_9Lu(PO_4)_7$ compounds. The room temperature luminescence of $Ca_9Al(PO_4)_7:Pr^{3+}$ and $Ca_9Lu(PO_4)_7:Pr^{3+}$ powders have been systematically studied for various Pr^{3+} concentration. The evolution of luminescence with temperature has been also analyzed. The attention was put into the 4f→4f transitions. The 5d→4f spectroscopy of $Ca_9Lu(PO_4)_7$: Pr^{3+} has been presented elsewhere [11, 12].

5.2. Experimental

Pr^{3+}-doped $Ca_9Al(PO_4)_7$ powders were prepared by the citrate route as described elsewhere [5]. Six samples have been synthesized with different Pr^{3+} concentrations. For $Ca_9Al(PO_4)_7$ samples, Pr^{3+} % mol concentration is referred to Ca^{2+} ions concentration. This notation will be used from now on. $Ca_9Lu(PO_4)_7:Pr^{3+}$ powders were synthesized by solid state reaction at high temperature. $CaCO_3$ (>99%), $(NH_4)_2HPO_4$ (>99%), Pr_6O_{11} (99.999%) and Lu_2O_3 (99.99%) powders were mixed and pressed into pellets under a load of 10 tons. The samples underwent three thermal treatments under air atmosphere (350 ^oC for 16 hours, 750 ^oC for 5 hours and 1200 ^oC for 10 hours), with intermediate grindings. A total of three samples have been synthesized, with different Pr^{3+} concentrations. In this case, the Pr^{3+} % mol concentration is referred to Lu^{3+} ions concentration. This notation will be used from now on.

Powder X-ray diffraction (PXRD) patterns were collected in a 2θ range of 5-100^o with an X'Pert Pro PANalytical X-ray diffractometer (Cu, $K_{\alpha 1}$: 1.54060 Å). The scan rate was set to 0.026^o and the exposure time to three hours. For the Rietveld refinement [13] the isotropic approach [14] implemented in MAUD software [15]. For $Ca_9Lu(PO_4)_7$ the structural model proposed by Golubev *et al*. [16] was employed (PDF card No.04-001-9672). The OF's of the metal cations (Ca^{2+} and Lu^{3+}) in the four available crystal sites have been placed equal to the ones calculated by Bessière *et al*. for $Ca_9Lu(PO_4)_7$ [8]. The structural model for $Ca_9Al(PO_4)_7$

has been built from the previous one by constraining M1-M3 and M5 sites to be fully occupied by Ca^{2+} and Al^{3+} ions, respectively. As mentioned before the M4 site must be empty for charge neutrality. For the refinement the following steps were followed: (i) scale and background refinement (4 polynomial coefficients) and (ii) cell refinement after the determination of the instrumental 2θ offset by means of the standard LaB_6 SRM 660a provided by NIST.

The luminescence excitation spectra were recorded using a McPherson spectrometer with a 0.3 m Criss Cross Czerny-Turner monochromator equipped with a 150 W Xe lamp as excitation source and a Hamamatsu R928 photomultiplier for the signal detection. The emission spectra were measured by using a Ti:Sapphire laser (448 nm) pumped by the second harmonic of a YAG:Nd^{3+} pulsed laser (532 nm). As a detector a Hamamatsu PMA-12 photonic multichannel analyzer was used. Decay curves were collected on a LeCroy Wavesurfer oscilloscope under the same excitation condition as for emission spectra. The luminescence temperature quenching measurements were made with the help of a Linkam THMS-600 heating stage.

Complementary room temperature luminescence spectra and decay curves were measured with a Fluorolog 3 (Horiba-Jobin Yvon) spectrofluorometer, equipped with a Xe lamp, a double excitation monochromator, a single emission monochromator (mod.HR320) and a photomultiplier in photon counting mode for the detection of the emitted signal.

For the room temperature radioluminescence spectra measurements the samples were excited with an X-ray (40 kV, 15 mA) tube (Seifert Gmbh), and the signal detected with a custom made 5000 M Horiba Jobin Yvon fluorescence spectrometer.

5.3. Results and discussion

The collected XRD patterns of $Ca_9Al(PO_4)_7:Pr^{3+}$ are presented in Figure 5.1a. It is possible to observe that all peaks match well with the theoretical pattern from ICSD card No. 48-1192. The absence of additional

peaks confirms that for all dopant concentration pure phase samples were obtained. As discussed previously, $Ca_9Al(PO_4)_7$ crystallizes in the trigonal *R3c* space group (Figure 5.1b) [4]. The values for the unit cell parameters obtained by means of the Rietveld refinement are reported in Table 5.1.

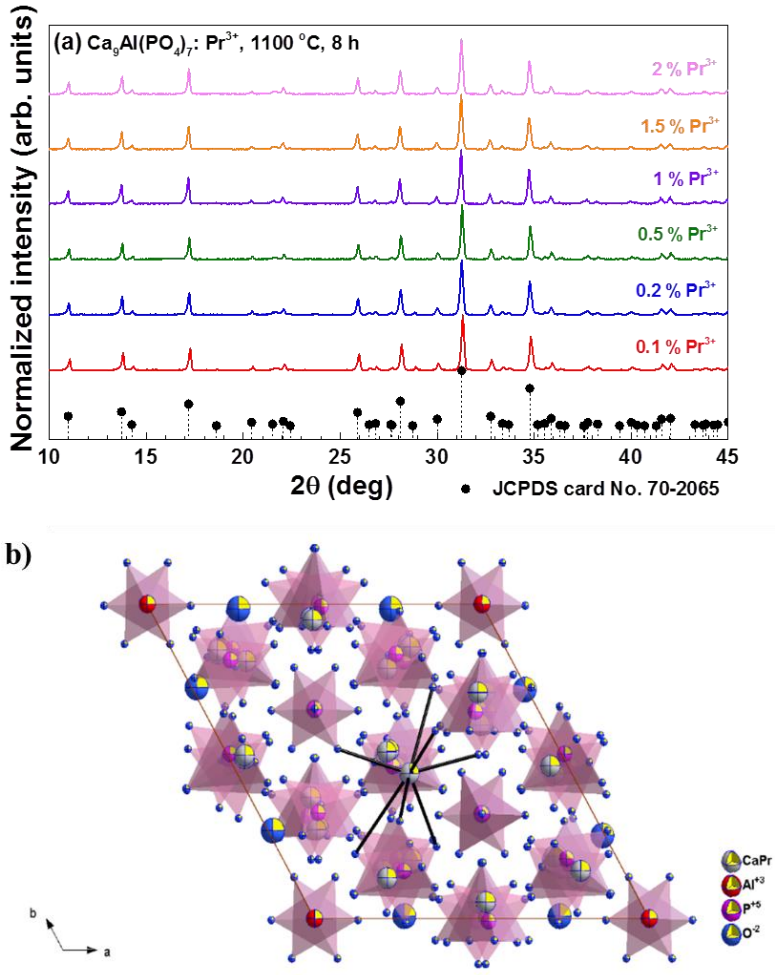

Fig. 5.1. (a) Collected PXRD patterns and (b) crystal structure of the $Ca_9Al(PO_4)_7:Pr^{3+}$ samples.

Figure 5.2a presents the collected X-ray diffraction patterns of the $Ca_9Lu(PO_4)_7:Pr^{3+}$ powders. Spectra show that the obtained materials are single phase with whitlockite-like structure. The values of the unit cell parameters were also obtained by means of the Rietveld refinement, and the

results are compared to the reference data of an undoped single crystal of $Ca_9Lu(PO_4)_7$ in Table 5.2.

Table 5.1

Unit cell parameters of the x Pr^{3+} % mol $Ca_9Al(PO_4)_7$ compounds obtained by the Rietveld method.

Sample	a (Å)	c (Å)	V (Å^3)	R_w (%)
$Ca_9Al(PO_4)_7$	10.3140(2)	37.253(1)	3432.00(6)	6.34
0.1% Pr^{3+}	10.3095(3)	37.243(1)	3428.07(6)	4.82
0.2% Pr^{3+}	10.3135(5)	37.256(6)	3432.02(7)	4.33
0.5% Pr^{3+}	10.3214(5)	37.278(3)	3439.22(4)	4.49
1.0% Pr^{3+}	10.3179(0)	37.238(0)	3433.20(4)	5.09
1.5% Pr^{3+}	10.3299(9)	37.301(2)	3447.01(6)	4.53
2.0% Pr^{3+}	10.3275(7)	37.289(7)	3444.44(7)	5.11

Table 5.2

Unit cell parameters of the x Pr^{3+} % mol $Ca_9Lu(PO_4)_7$ compounds obtained by the Rietveld method.

Sample	a (Å)	c (Å)	V (Å^3)	R_w (%)
$Ca_9Lu(PO_4)_7$ [15]	10.434	37.34	3520.52	--
1% Pr^{3+}	10.4390(2)	37.345(8)	3524.4(1)	6.65
2% Pr^{3+}	10.4391(3)	37.360(2)	3525.8(6)	7.08
10% Pr^{3+}	10.4399(3)	37.375(2)	3527.8(6)	8.61

After the inspection of Tables 5.1 and 5.2 it can be observed that the cell volume increases with the increase of Pr^{3+} concentration for both the aluminium and lutetium hosts. Since Pr^{3+} ion is much larger than Al^{3+} [17], Al^{3+}/Pr^{3+} substitution in $Ca_9Al(PO_4)_7$ is not possible and therefore only Ca^{2+}/Pr^{3+} substitution can take place. The valence mismatch between Pr^{3+} and Ca^{2+} ions possibly may create Pr^{3+}-□-Pr^{3+} entities in the Pr^{3+} doped $Ca_9Al(PO_4)_7$ samples, where □ denotes a calcium vacancy created to compensate the charge. On the contrary, Pr^{3+} ion is almost the same size as Ca^{2+} and slightly bigger than Lu^{3+} [17], and therefore the possibility of Ca^{2+}/Pr^{3+} and Lu^{3+}/Pr^{3+} substitutions in $Ca_9Lu(PO_4)_7$ has to be taken into account. Since in the Lu-based whitlockites, M1-M3 and M5 sites are shared by Ca^{2+} and Lu^{3+} [2] there is a much smaller probability of creating

Ca^{2+} vacancies, although defects are still present in these doped whitlockites [10].

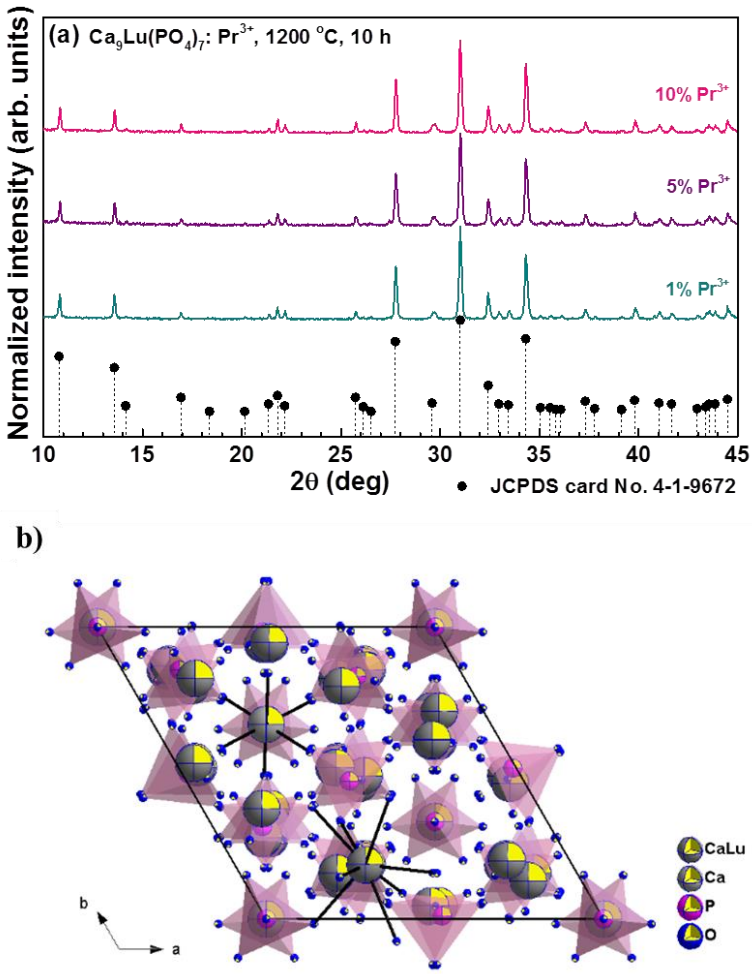

Fig. 5.2. (a) Collected PXRD patterns and (b) crystal structure of the $Ca_9Lu(PO_4)_7:Pr^{3+}$ samples.

Taking these features into account, it seems clear that for $Ca_9Al(PO_4)_7:Pr^{3+}$ the RE^{3+} ions enter into the host substituting for Ca^{2+} in M1, M2 and M3 crystal sites, whereas for $Ca_9Lu(PO_4)_7$ they can enter also into M5 site, even if a preference for three crystal sites (M1, M2 and M3) has been previously postulated for the sample having a doping level of 1% mol, by means of a combined theoretical and experimental study regarding the 5d→4f electronic transition of Pr^{3+} ion [10]. A detailed structural study on

$Ca_9Lu(PO_4)_7$ doped with different amount of Pr^{3+} seems to confirm this site distribution of the dopant ion [2].

It is interesting to determine the average distance between nearest Pr^{3+} ions in both Al and Lu samples. This value (R) can be calculated by the formula:

$$R = \sqrt[3]{\frac{3}{4\pi N}} \qquad (5.1)$$

where N is the ion concentration in ions/cm^3 [18]. Table 5.3 presents the values of the average distance for adjacent Pr^{3+} in $Ca_9Al(PO_4)_7$ and $Ca_9Lu(PO_4)_7$, estimated using equation 5.1.

Table 5.3

Estimated values for the average distance R of $Ca_9Al(PO_4)_7$ and $Ca_9Lu(PO_4)_7$ samples. The value of the ion concentration in ions/cm^3 is also included to help comparison between the two different hosts. It is possible to observe that for similar Pr^{3+} content (in ions/cm^3) distances are almost the same in both hosts.

	Pr^{3+} (%)	**N (ions/cm^3)**	**R (Å)**
$Ca_9Al(PO_4)_7$	0.1	$1.58\cdot10^{19}$	24.7
	0.2	$3.15\cdot10^{19}$	19.6
	0.5	$7.88\cdot10^{19}$	14.5
	1.0	$1.58\cdot10^{20}$	11.5
	1.5	$2.36\cdot10^{20}$	10.0
	2.0	$3.15\cdot10^{20}$	9.1
$Ca_9Lu(PO_4)_7$	1.0	$1.71\cdot10^{19}$	24.1
	5.0	$8.53\cdot10^{19}$	14.1
	10.0	$1.71\cdot10^{20}$	11.2

Figure 5.3a presents the room temperature excitation spectrum for the $Ca_9Al(PO_4)_7$:0.1% Pr^{3+} sample. For all Al-based compounds the spectrum consists of three bands, which can be assigned to the $^3H_4 \rightarrow {}^3P_2$, $^3H_4 \rightarrow {}^3P_1$ + $^1I_6$ and $^3H_4 \rightarrow {}^3P_0$ Pr^{3+} transitions, with maxima located at 448, 474 and 487 nm, respectively. The room temperature excitation spectra of the $Ca_9Lu(PO_4)_7$:1% Pr^{3+}-doped sample is presented in Figure 5.3b. For all

Lu-based samples, the spectrum is similar to the one recorded for the $Ca_9Al(PO_4)_7$: Pr^{3+} powders.

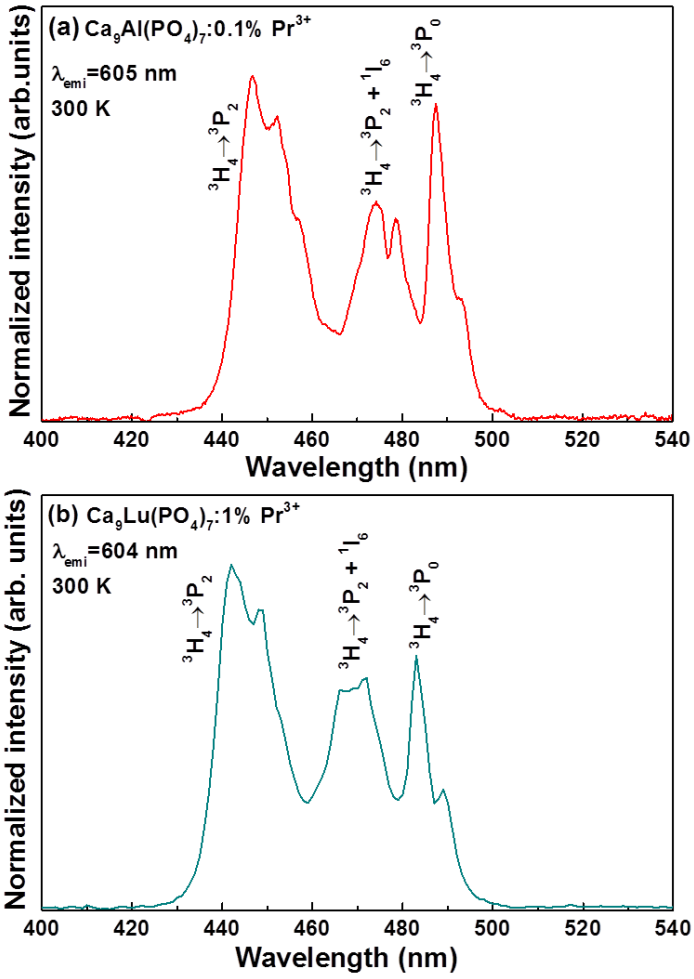

Fig. 5.3. Room temperature excitation spectra of (a) $Ca_9Al(PO_4)_7:Pr^{3+}$ and (b) $Ca_9Lu(PO_4)_7:Pr^{3+}$.

Figure 5.4 shows the emission spectra of all the Al-based and Lu-based samples measured at 77 and 300 K upon excitation at 448 nm. All spectra are normalized to the $^3P_0 \rightarrow {}^3H_4$ transition of Pr^{3+}. Figure 5.4a presents the 77 K spectra for the $Ca_9Al(PO_4)_7$ powders. For samples with 0.1-0.5% doping content the most intense band appears at 612 nm and is ascribed to the $^1D_2 \rightarrow {}^3H_4$ transition. For higher concentrations, however, the most intense band is located at 650 nm and is assigned to the $^3P_0 \rightarrow {}^3F_2$ transition. An

analogous behaviour is observed in the room temperature spectra (Figure 5.4b). The other bands are assigned to the $^3P_0 \rightarrow {}^3H_4$, $^3P_0 \rightarrow {}^3H_5$, $^1D_2 \rightarrow {}^3H_6$ and $^1D_2 \rightarrow {}^3F_3$ transitions, with maxima at 491, 529, 695 and 730 nm respectively. At room temperature all bands are broadened, which is presumably connected to the charge mismatch between Pr^{3+} and Ca^{2+} ions and to the multisite nature of the host, while at 77 K the bands are narrower and well separated.

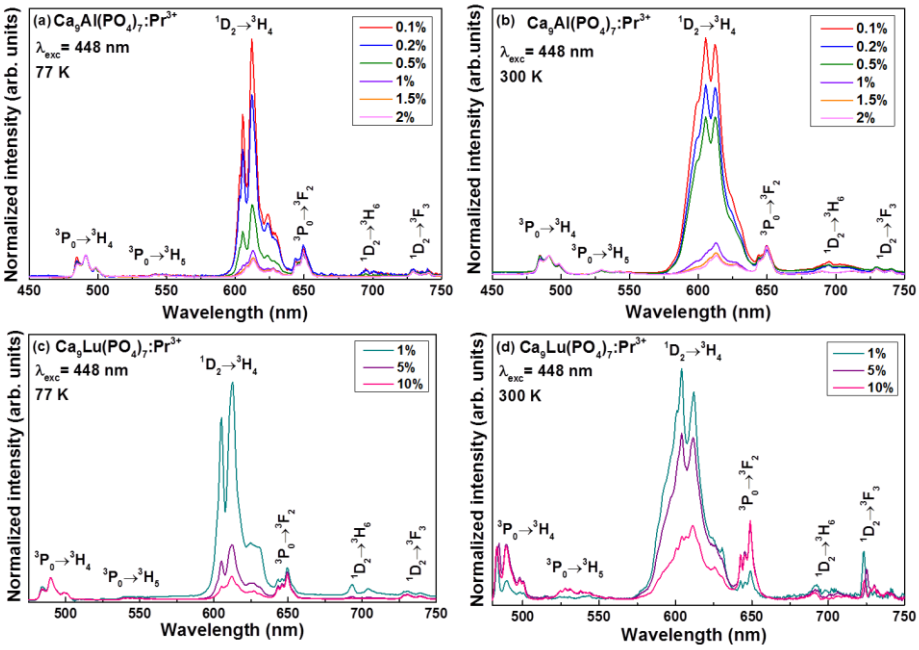

Fig. 5.4. Emission spectra of $Ca_9Al(PO_4)_7:Pr^{3+}$ (a) and (b) and $Ca_9Lu(PO_4)_7:Pr^{3+}$(c) and (d) measured at 77 and 300 K.

For the Lu-based samples, room temperature emission spectra were also measured for all dopant concentrations upon excitation at 448 nm (Figure 5.4d). For both the 1% and the 5% Pr^{3+}-samples the dominant line is located at 604 nm and corresponds to the $^1D_2 \rightarrow {}^3H_4$ transition, while for the 10%-sample two bands with almost the same intensity are observed. The most intense is the one located at 650 nm and is ascribed to the $^3P_0 \rightarrow {}^3F_2$ transition, whereas the other one, with maximum at 611 nm, corresponds to the $^1D_2 \rightarrow {}^3H_4$ transition. It is also possible to observe the $^3P_0 \rightarrow {}^3H_4$, $^3P_0 \rightarrow {}^3H_5$, $^1D_2 \rightarrow {}^3H_5$ and $^3P_0 \rightarrow {}^3F_4$ transitions, with maxima located at 485, 530, 692 and 720 nm respectively. Emission spectra at 77 K for all samples are

shown in Figure 5.4c. At low temperature the bands are narrower and better resolved. The spectral positions and assignments are the same as for the room temperature spectra.

It is possible to observe that the emission from the $^1D_2$ level is quenched with increasing dopant concentration. To explain this phenomenon the energy level scheme of Pr^{3+} ions is used (Figure 5.5). Excitation and emission paths are marked with colour solid arrows. After the excitation in the $^3P_2$ level there is a non-radiative relaxation to the $^3P_0$ level (short dashed pink arrow), from which emission takes place. The $^1D_2$ level can be populated via two different routes: the first one is by multiphonon relaxation (MPR) from the $^3P_0$ level (short dashed purple arrow); the second one is by the cross relaxation process $[^3P_0, {}^3H_4] \rightarrow [^3H_6, {}^1D_2]$ (CR1). The MPR rate can be estimated from the van Dijk and Schuurmans modified energy gap law [19]:

$$W_{MPR} = \beta_{el} exp[-\alpha(\Delta E - 2\hbar\omega_{max})] \qquad (5.2)$$

where $\alpha = 4.7 \cdot 10^{-3}$ and $\beta_{el} = 6.2 \cdot 10^7$ are constants suitable for phosphate hosts, ΔE is the energy gap to the next lower level and $\hbar\omega$ is the maximum phonon energy for the desired host. Using the appropriate values for $Ca_9Al(PO_4)_7$ and $Ca_9Lu(PO_4)_7$ (ΔE = 3800 cm^{-1} and $\hbar\omega$ = 1110 cm^{-1} [5]) a value of $3.7 \cdot 10^4$ s^{-1} is obtained, which makes the MPR process very probable since less than four phonons are needed to bridge the energy gap. On the other hand, increasing the concentration of dopant does not seem to affect strongly the decay times of the $^3P_0$ level (see Figure 5.6 and Table 5.3), therefore cross relaxation seems to be less probable than MPR in these conditions.

In the case of the emission observed at 605 nm, the situation is more complicated since the red band is a mixture of the $^3P_0$ and $^1D_2$ levels, and an accurate analysis in this case is impossible. It can be assumed that the MPR process for the $^1D_2$ level is less probable since the energy gap between next lower levels is more than 7000 cm^{-1}, and therefore at least seven phonons are required to bridge it ($W_{MPR} < 10^{-2}$ s^{-1}). It seems that the most probable mechanism is the $[^1D_2, {}^3H_4] \rightarrow [^1G_4, {}^3F_{3,4}]$ cross relaxation process (CR2), which is phonon assisted [20]. This is particularly true if a relatively short distance between nearest Pr^{3+} ions is taken into account. Moreover, if

$Ca_9Al(PO_4)_7$ and $Ca_9Lu(PO_4)_7$ are compared selecting samples with similar concentration of Pr^{3+} in ions/cm^3, the emission spectra are almost the same in shape and relative intensities. This indicates that possibly in $Ca_9Lu(PO_4)_7$ Pr^{3+} ions occupy mostly M(1)-M(3) sites, as in $Ca_9Al(PO_4)_7$, in agreement with previous studies [11].

Room and low temperature decay curves were measured for all samples monitoring emission from $^1D_2$ and $^3P_0$ levels. The $Ca_9Al(PO_4)_7$:Pr^{3+} curves recorded at 77 K are presented in Figure 5.6a (emission from $^1D_2$) and Figure 5.6b (emission from $^3P_0$), whereas the 77 K curves for $Ca_9Lu(PO_4)_7$:Pr^{3+} are presented in Figure 5.6c (emission from $^1D_2$) and Figure 5.6d (emission from $^3P_0$). Since almost all decay curves are not single exponential, we have calculated average decay constants using the equation:

$$\tau_{av} = \frac{\int I(t)\cdot t dt}{\int I(t) dt} \qquad (5.3)$$

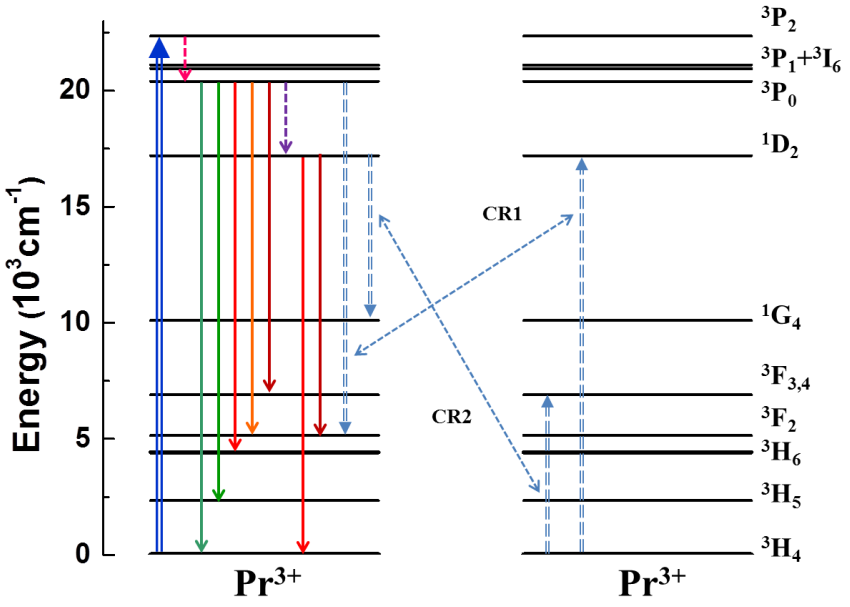

Fig. 5.5. Energy levels scheme of Pr^{3+} in $Ca_9Al(PO_4)_7$:Pr^{3+} and $Ca_9Lu(PO_4)_7$:Pr^3.

The values of the decay constants are listed in Table 5.4. It is possible to see that in both hosts, the decay constants of the $^1D_2$ level are

significantly reduced when increasing the dopant concentration, pointing out that the $^1D_2$ level is sensitive to concentration. This is true both at 77 and 300 K. When comparing the results for $Ca_9Al(PO_4)_7$: 0.1, 0.5 and 1% of Pr^{3+} with the ones for $Ca_9Lu(PO_4)_7$: 1, 5 and 10% of Pr^{3+}, it can be seen that the decay constant values are almost the same. For the transition from the $^3P_0$ level, emission has been monitored at 649 nm at temperatures of 77 and 300 K. It is easy to see that decay constant is more or less stable at $\tau_{av} \approx 0.9$ μs, and does not change with the temperature or the dopant concentration.

Table 5.4

Decay times of $Ca_9Al(PO_4)_7$ and $Ca_9Lu(PO_4)_7$ samples measured at low and room temperature. Emissions at 605 and 649 nm were monitored upon excitation at 448 nm.

	Pr^{3+}	**Decay time at 77K (μs)**		**Decay time at 300K (μs)**	
	(%)	**605 nm**	**649 nm**	**605 nm**	**649 nm**
$Ca_9Al(PO_4)_7$	0.1	128	0.960	133	1.00
	0.2	120	0.910	118	1.00
	0.5	58	0.770	53	0.81
	1.0	14	0.750	13	0.78
	1.5	11	0.820	19	0.82
	2.0	13	0.860	2	0.75
$Ca_9Lu(PO_4)_7$	1.0	163	0.831	172	0.91
	5.0	51	0.875	69	0.93
	10.0	16	0.850	13	0.84

Table 5.5 contains the values of the ratio between $^1D_2$ and $^3P_0$ emission bands for $Ca_9Al(PO_4)_7$ and $Ca_9Lu(PO_4)_7$ at room temperature. In both hosts it is possible to observe quenching of the $^1D_2$ emission as Pr^{3+} doping concentration is increased. The behaviour is not exactly the same in both materials. The detailed values for comparable ion concentrations are different in the two hosts presumably due to the different inter-manifold transition probabilities, induced by different Judd-Ofelt intensity parameters.

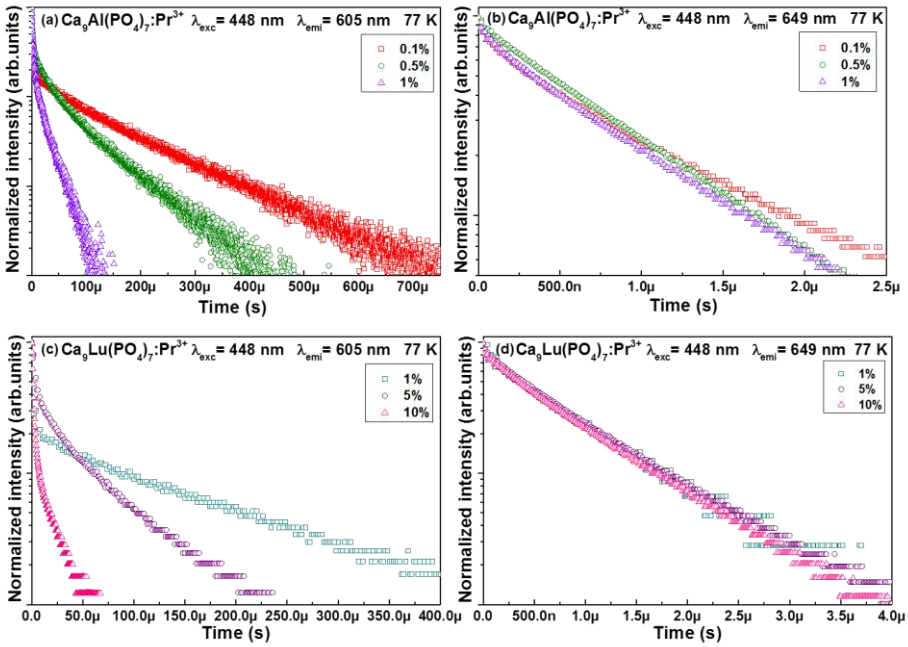

Fig. 5.6. Decay curves of $^1D_2$ and $^3P_0$ of $Ca_9Al(PO_4)_7:Pr^{3+}$ (a) and (b) and $Ca_9Lu(PO_4)_7:Pr^{3+}$(c) and (d) measured at 77 K.

Table 5.5

Ratio of the transitions from the $^1D_2$ and $^3P_0$ levels in $Ca_9Al(PO_4)_7$ and $Ca_9Lu(PO_4)_7$ samples.

	Pr^{3+} (%)	$^1D_2 \rightarrow {}^3H_4/{}^3P_0 \rightarrow {}^3H_4$	$^1D_2 \rightarrow {}^3H_4/{}^3P_0 \rightarrow {}^3F_2$
$Ca_9Al(PO_4)_7$	0.1	10.64	8.32
	0.2	8.15	5.72
	0.5	3.22	3.11
	1.0	1.17	1.08
	1.5	0.86	0.78
$Ca_9Lu(PO_4)_7$	1.0	4.36	1.76
	5.0	2.96	2.22
	10.0	1.39	0.94

The temperature evolution of emission has been analysed in the 77-800 K range. The results are presented in Figure 5.7. For the $Ca_9Al(PO_4)_7$ powders, samples with 0.1% (Figure 5.7a) and 2% (Figure 5.7b) of Pr^{3+} concentration were analysed. In the case of the $Ca_9Lu(PO_4)_7$ powders

samples with 1% (Figure 5.7c) and 10% (Figure 5.7d) of Pr^{3+} were studied. It is possible to observe that for the aluminium samples and the 10%-Pr^{3+} lutetium sample, the maximum of emission is reached at the lowest temperature (77 K), whereas for the $Ca_9Lu(PO_4)_7$:1% sample the emission intensity of the band increases with temperature achieving its maximum at 350 K, and then starts to decrease. The mechanisms responsible for this phenomenon depend on the level from which emission occurs, as discussed previously.

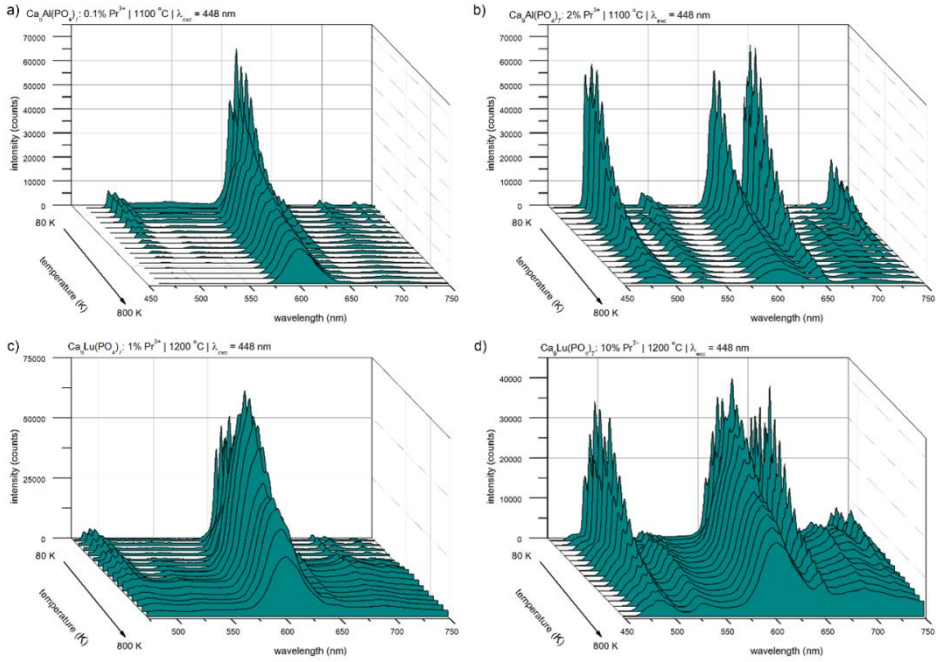

Fig. 5.7. Emission spectra of $Ca_9Al(PO_4)_7$:0.1 and 2% Pr^{3+} ((a) and (b) respectively) and $Ca_9Lu(PO_4)_7$:1 and 10% Pr^{3+}((c) and (d) respectively) as a function of temperature.

Room temperature radioluminescence spectra revealed no efficient host-to-impurity energy transfer in $Ca_9Lu(PO_4)_7:Pr^{3+}$. In fact, spectra show only very weak 4f→4f Pr^{3+} emission bands in the range 490-650 nm, whereas no 5d→4f bands are observed. A close inspection of the spectra shows the same concentration dependency on the emission bands ratio observed previously upon excitation at 448 nm. These results are in good agreement with the VUV-synchrotron measurements for $Ca_9Lu(PO_4)_7:Pr^{3+}$ reported by Trevisani *et al*. in [11]. Moreover, the authors discussed an

interesting model regarding the possible presence of a limiting factor for the host-to-impurity transfer for Pr^{3+} in the $Ca_9Lu(PO_4)_7$ host.

5.4. Conclusions

In the present chapter the synthesis, structural characterization and luminescence properties of $Ca_9Al(PO_4)_7$:Pr^{3+} and $Ca_9Lu(PO_4)_7$:Pr^{3+} powders have been presented for various Pr^{3+} doping concentrations. The obtained results show concentration quenching of Pr^{3+} emission from $^1D_2$ level at high doping content, due to the presence of cross relaxation processes, whereas no evident changes due to concentration are observed in the emission from $^3P_0$ level. Temperature quenching of emission has been observed in the case of transitions from $^1D_2$, and it is associated to cross relaxation de-excitation. For transitions from $^3P_0$ level no clear temperature quenching has been found, and the behaviour observed when increasing temperature can be explained on the basis of the presence of MPR processes. The measured decay times for Pr^{3+} in these hosts do not present single exponential behavior, and their concentration dependence reinforces the results extracted from the emission spectra. These results show clearly that for Pr^{3+} doping, the optical spectroscopy of the whitlockite $Ca_9M(PO_4)_7$ disordered host is relatively insensitive to the nature of the M trivalent cation, as previously observed in other disordered materials [21, 22].

References

[1] H. Ji, Z. Huang, Z. Xia, M.S. Molokeev, V.V. Atuchin, M. Fang, Y. Langai, *J. Phys. Chem. C* 119 (2015) 2038-2045.

[2] F. Piccinelli, M. Trevisani, J.R. Plaisier, M. Bettinelli, *J. Rare Earths* 33 (2015) 977-982.

[3] Z. Xia, H. Liu, X. Li, C. Liu, *Dalton Trans.* 42 (2013) 16588-16595.

[4] F. Du, Y. Nakai, T. Tsuboi, Y. Huang, H.J. Seo, *J. Mater. Chem.* 21 (2011) 4669-4678.

[5] R. Pazik, K. Zawisza, A. Watras, K. Maleszka-Baginska, P. Boutinaud, R. Mahiou, P. J. Dèren, *Mater. Res. Bull.* 48 (2013) 337-342.

[6] Q. Liu, Y. Liu, Z. Yang, X. Li, Y. Han, *Spectrochim. Acta Part A Mol. Biomol. Spectrosc*. 87 (2012) 190-193.

[7] J. Zhang, Z. Zhai, G. Chen, *J. Lumin* 154 (2014) 193-197.

[8] N. Guo, Y. Huang, H. You, M. Yang, Y. Song, K. Liu, Y. Zheng, *Inorg. Chem*. 49 (2010) 10907-10913,

[9] H. Yamamoto, *J. Electrochem. Soc*. 127 (1980) 694.

[10] A. Bessiere, R.A. Benhamou, G. Wallez, A. Lecointre, B. Viana, *Acta Mater* 60 (2012) 6641-6649.

[11] M. Trevisani, K.V. Ivanovskikh, F. Piccinelli, A. Speghini, M. Bettinelli, *J. Phys. Condens. Matter* 24 (2012) 489-501.

[12] C.-G. Ma, M. Trevisani, F. Piccinelli, K.V. Ivanovskikh, M. Bettinelli, M.G. Brik, *J. Phys. Condens. Matter* 25 (2013) 165503.

[13] H.M. Rietveld, *J. Appl. Crystallogr*. 2 (1969) 65-71.

[14] R.A. Young (Ed.), *The Rietveld Method*, Oxford Science, Oxford, United Kingdom, 1993.

[15] L. Lutterotti, S. Gialanella, *Acta Mater* 46 (1998) 101-110,.

[16] V.N. Golubev, B.I. Lazoryak, *Inorg. Mater*. (English Transl). 27 (1991) 480.

[17] R.D. Shannon, C.T. Prewitt, *Acta Crystallogr. Sect B Struct. Crystallogr. Cryst. Chem*. 25 (1969) 925-946.

[18] D.F. De Sousa, F. Batalioto, M.J.V. Bell, S.L. Oliveira, L.A.O. Nunes, *J. Appl. Phys*. 90 (2001) 3308-3313.

[19] J.M.F. van Dijk, M.F.H. Schuurmans, *J. Chem. Phys*. 78 (1983) 5317.

[20] J. Collins, M. Geen, M. Bettinelli, B. Di Bartolo, *J. Lumin* 132 (2012) 2626-2633.

[21] M.F. Hoogendorp, W.J. Schipper, G. Blasse, *J. Alloys Compd*. 205 (1994) 249-251.

[22] A.M. Srivastava, S.J. Camardello, H.A. Comanzo, M. Aycibin, U. Happek, *Opt. Mater*. 32 (2010) 936-940.

Chapter 6

Structural effects and 5d→4f emission transition shift induced by Y co-doping in Pr-doped $K_3Lu_{1-x}Y_x(PO_4)_2$

In the present chapter the structural and spectroscopic properties of several materials belonging to the $K_3Lu_{1-x}Y_x(PO_4)_2$ family and activated with 1% of Pr^{3+} have been studied in detail. The structural characterization has been performed by X-ray diffraction. The crystal structure of the host has been determined by means of Rietveld refinement of the powder diffraction pattern, in the case of $K_3Y(PO_4)_2$ doped with 1% of Pr^{3+}. The optical emission upon UV direct excitation into the dopant ion is dominated by the Pr^{3+} $4f^15d^1 \rightarrow 4f^2$ interconfigurational transitions; the substitution of Lu by Y causes the blue shift of the $4f^15d^1 \rightarrow 4f^2$ emission band. This is due to an important change of the Pr^{3+} local environment. Upon X-ray excitation it has been found that the ratio between the $4f^15d^1 \rightarrow 4f^2$ and 4f→4f emission intensities varies progressively when Y^{3+} concentration is increased. This behavior is explained in terms of the favorable overlap between the defect-related luminescence of the host and the Pr^{3+} 4f→4f interconfigurational transitions. No thermal quenching of the Pr^{3+} luminescence has been observed up to 500 K.

6.1. Introduction

In recent years, much attention has been devoted to the 5d→4f emission of Pr^{3+} ions in several wide band-gap hosts because of its shorter decay time, allowing for the development of new scintillators which are two or three times faster than those activated with Ce^{3+} ions [1, 2], and can, therefore, show better performances for some applications [3].

Among many possible hosts, double phosphates appear as a promising option. It has been found that in several double phosphates constituted of lanthanide ions, the absorption edge is located at rather high energy [4, 5]. Furthermore, these compounds exhibit a relatively short attenuation length, high effective atomic number, short fluorescence decay time and high luminous efficiency, which make them suitable for various optical applications including fast scintillators and vacuum ultraviolet phosphors. In particular, the $K_3Lu(PO_4)_2$ double phosphate is interesting due to the effective energy transfer from host-to-ion that it shows upon VUV synchrotron radiation excitation when doped with Ce^{3+} [6] and Pr^{3+} [7], which opens the possibility of its application as a fast scintillator. The room temperature phase of $K_3Lu(PO_4)_2$ (trigonal $P\bar{3}$) transforms at 130 K (on cooling) into a monoclinic ($P2_1/m$) structure. The transformation proceeds through an intermediate monoclinic phase observed at 230 K [8]. On the contrary, $K_3Y(PO_4)_2$ retains the monoclinic structure ($P2_1/m$ isostructural with the low temperature structure of $K_3Lu(PO4)_2$) until 513 K. From these results it is reasonable to suppose that the temperature stability of both the monoclinic and trigonal phase should, in principle, be tuned by changing both the temperature and the Y/Lu ratio within the compositions.

In this chapter, several materials belonging to the Pr^{3+}-doped $K_3Y_xLu_{1-x}(PO_4)_2$ (x = 0, 0.08, 0.16, 0.25, 0.5, 0.75, 1) crystal family have been studied. The crystal structure of this solid solution should be strongly dependent on the relative Y/Lu amount. The synthesis and structural characterization of these doped materials is described in detail and the crystal structure of monoclinic $K_3Y(PO_4)_2$ has been determined. The underlying idea is that Y^{3+} ions increase the stability of the monoclinic phase (*i.e.* no phase transitions take place up to high temperatures). The spectroscopic characterization of the samples (including the ones showing thermally induced phase transitions) has been performed by

photoluminescence excitation (PLE), emission (PL), and decay kinetics measurements in the temperature interval 8-500 K, as well as by radioluminescence spectra recorded at room temperature.

6.2. Experimental

Polycrystalline samples of $K_3Lu_{1-x}Y_x(PO_4)_2$ (x = 0, x = 0.08, x = 0.16, x = 0.25, x = 0.50, x = 0.75 and x = 1.00) doped with 1% mol of Pr^{3+} were prepared by solid state reaction. K_2CO_3 (99%), Y_2O_3 (99%), Lu_2O_3 (99%), $(NH_4)_2HPO_4$ (> 99%) and Pr_6O_{11} (99.999%) powders were mixed and pressed into pellets under a load of 10 tons. The samples underwent two thermal treatments under air atmosphere (600 ^oC for 4 hours and 950 ^oC for 1 hour), with intermediate grindings.

Powder X-ray diffraction (PXRD) measurements were carried out by means of a Thermo ARL X'TRA powder diffractometer, operating in the Bragg-Brentano geometry and equipped with a Cu-anode X-ray source (Kα, λ = 1.5418 Å), using a Peltier Si (Li) cooled solid state detector. The patterns of the 1% Pr^{3+}-doped $K_3Lu_{1-x}Y_x(PO_4)_2$ powders were collected with a scan rate of 0.04 ^{o}/s in the 5-90^o 2θ range for $K_3Lu(PO_4)_2$, $K_3Lu_{0.92}Y_{0.08}(PO_4)_2$, $K_3Lu_{0.84}Y_{0.16}(PO_4)_2$, $K_3Lu_{0.75}Y_{0.25}(PO_4)_2$, and a scan rate of 0.003 °/s in the 10-100° 2θ range for $K_3Y(PO_4)_2$ sample. The phase identification was performed with the PDF-4+2013 database provided by the International Centre for Diffraction Data (ICDD). Polycrystalline samples were ground in a mortar and then put in a low-background sample holder for the data collection. The General Structure Analysis System (GSAS) program was employed for the Rietveld refinement calculations [9, 10] on the powder pattern of 1% Pr^{3+}-doped $K_3Y(PO_4)_2$ sample.

The photoluminescence spectra and decay kinetics measurements were recorded in the temperature interval 8-500 K, whilst the radioluminescence spectra were measured only at room temperature. A custom made 5000 M Horiba Jobin Yvon fluorescence spectrometer was used in all the experiments. A Janis closed cycle cryostat was used in all the temperature dependent measurements. In the steady state photoluminescence and radioluminescence spectra measurements, the samples were excited with a deuterium lamp (Heraeus Gmbh) and an X-ray (40 kV, 15 mA) tube (Seifert

Gmbh), respectively. All spectra were corrected for the spectral distortion of the setup. In the decay kinetics measurements, a nanosecond hydrogen flash lamp was used as excitation source. The signal was recorded by means of multichannel scaling and time corrected single photon counting methods, respectively. True photoluminescence decay times were obtained using the convolution of the instrumental response function with an exponential function and the least-square-sum-based fitting program (Spectra Solve software package).

6.3. Results and discussion

6.3.1 Structural characterization

The symmetry and structure of the potassium rare-earth double phosphates with the general formula of $K_3RE(PO_4)_2$ (RE denotes rare earth element, or Y or Sc), depend on the relative size of the RE ion. In addition, any given composition typically exhibits one or more polymorphs as a function of temperature [8, 11, 12, 13]. Previous investigations have established that Pr^{3+} doped $K_3Lu(PO_4)_2$ undergoes various structural phase changes at low temperatures [7, 14]. This host crystallizes with a trigonal unit cell ($P\bar{3}$ space group) at RT [15], where the Lu^{3+} ions exhibit a six-fold coordination, with two non-equivalent sites in the crystal structure. Around 250 K, $K_3Lu(PO_4)_2$ undergoes the first transition and a monoclinic phase is obtained. The Lu^{3+} ion retains the six-fold coordination but it occupies only one crystal site. Around 140 K a second phase transition has the effect to change the coordination number of Lu^{3+} (from 6 to 7), whereas the monoclinic space group is retained [6, 7].

As far as the structural characterization of the $K_3Lu_{1-x}Y_x(PO_4)_2$ solid solution is concerned, the diffraction patterns of the samples are shown in Figure 6.1. At room temperature, the trigonal phase is stable up to a Y/Lu ratio around 0.1. For the sample with a Y^{3+} concentration of 0.16 an almost equimolar mixture of trigonal and monoclinic phases is observed. In the concentration range 0.25-1 of Y^{3+} ion, only the monoclinic phase is observed.

The crystal structure of $K_3Y(PO_4)_2$ has been already studied (PDF number 00-049-0497) [16] but the atomic fractional coordinates of the ions are not available. For these reason, we have decided to refine the crystal structure of the monoclinic $K_3Y(PO_4)_2$ doped with 1% of Pr^{3+}, by means of the Rietveld calculation on its powder pattern (Figure 6.2). From the inspection of the results, a single crystal site exhibiting 7-fold coordination and *m* point symmetry has been found for Y^{3+}. The calculated Y-O bond distances are as follows: Y(1)-O(1) = 2.457(3) Å, Y(1)-O(3) = 2.561(5) Å, Y(1)-O(4) = 2.398(3) Å, Y(1)-O(5) = 2.254 (3) Å(x2); Y(1)-O(6) = 2.314(5) Å(x2).

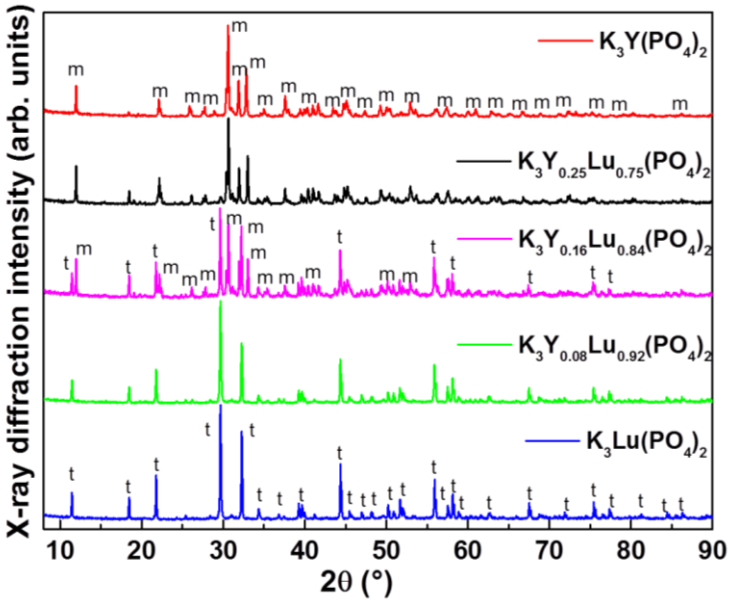

Fig. 6.1. Room temperature PXRD patterns of the $K_3Lu_{1-x}Y_x(PO_4)_2$ solid solution (x= 0, 0.08, 0.16, 0.25, 1). m= monoclinic phase ($P2_1/m$); t= trigonal phase ($P\bar{3}$).

In conclusion, we have confirmed our previous assumption: the crystal structure of the $K_3Lu_{1-x}Y_x(PO_4)_2$ solid solution can be tuned by changing the Y/Lu ratio. The samples with a low Y^{3+} content show a trigonal phase, whilst the ones with a high Y^{3+} content show a monoclinic structure. The local environment of the rare earth ion is strongly dependent on the crystal phase. In fact, in the trigonal structure it can occupy two 6-fold coordinated sites with C_3 and C_3i (S6) site symmetry, respectively. On the contrary, as mentioned above, in the monoclinic structure there is only one site available

for the rare earth ion with 7-fold coordination and Cs point symmetry. As the luminescent dopant Pr^{3+} ion substitutes for the rare earth ion of the matrix, and the 5d state of Pr^{3+} is very sensitive even to small variations in the local coordination, the energy of the 5d state should change with the Y^{3+} content in $K_3Lu_{1-x}Y_x(PO_4)_2:Pr^{3+}$. Also, the same transition from the trigonal to monoclinic phases observed by substituting Lu with Y in $K_3Lu_{1-x}Y_x(PO_4)_2:Pr^{3+}$ (Y/Lu above 0.30), can be obtained by lowering the temperature below 140 K in the case of $K_3Lu(PO_4)_2:Pr^{3+}$.

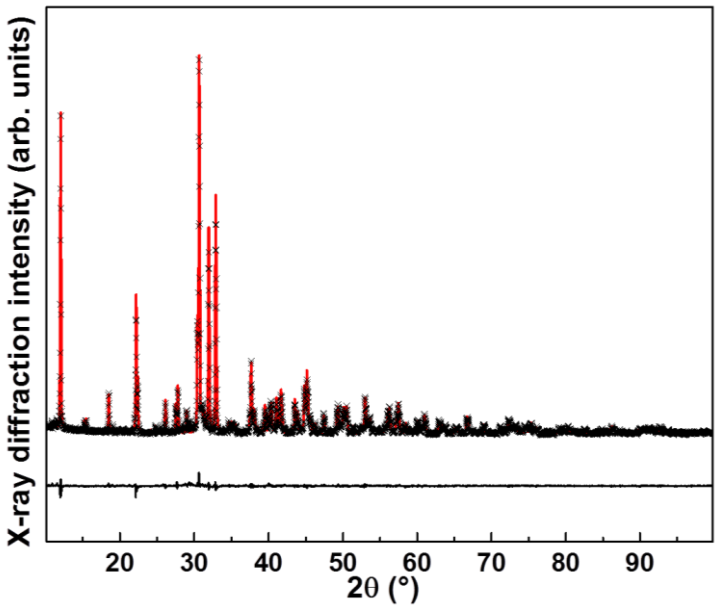

Fig. 6.2. XRD pattern (black crosses), Rietveld refinement (red solid line) and line of residuals (lower black line) of $K_3Y(PO_4)_2:Pr^{3+}$ (Rw=10.1%).

6.3.2 5d→4f transitions

6.3.2.1 $K_3Lu(PO_4)_2$: Pr^{3+}

The normalized low (8 K) and room temperature excitation spectra of $K_3Lu(PO_4)_2:Pr^{3+}$ are presented in Figure 6.3a The spectra were recorded for emission at 280 nm, corresponding to the 5d→4f transition of Pr^{3+} ion. For both phases the spectra present a similar shape, but the excitation band at

LT (low temperature) appears a shorter wavelength than at RT (room temperature).

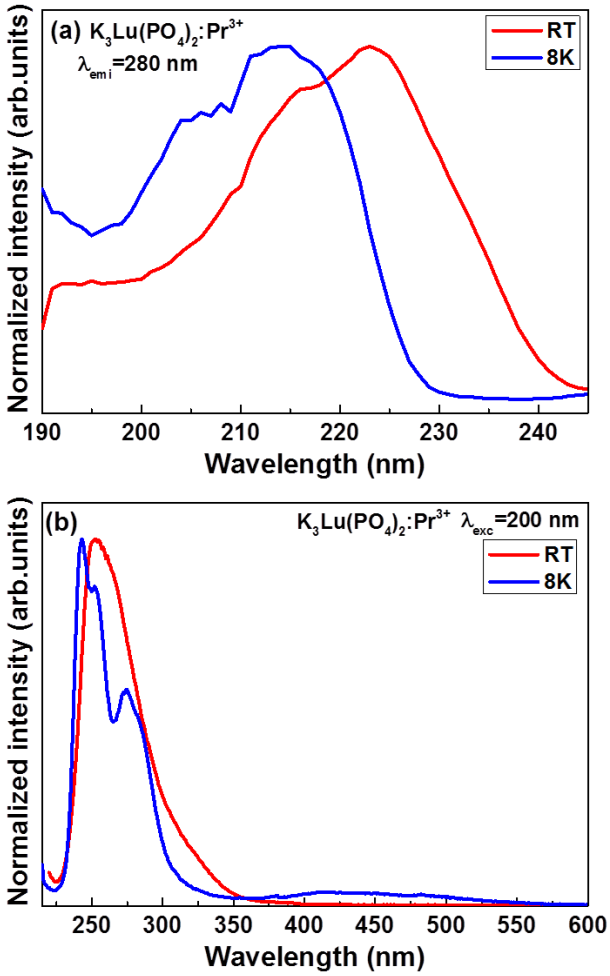

Fig. 6.3. Normalized of $K_3Lu(PO_4)_2:Pr^{3+}$ in both trigonal (RT) and monoclinic (8 K) phases. (a) Excitation spectra for emission at 280 nm and (b) emission spectra upon excitation at 200 nm.

Figure 6.3b shows the photoluminescence emission spectra of $K_3Lu(PO_4)_2:Pr^{3+}$ upon excitation at 200 nm, measured at low and room temperature. The low temperature (8 K) spectrum is dominated by the band with three maxima centered at 242, 253 and 274 nm, belonging to the $4f^15d^1 \rightarrow {}^3H_4$, ${}^3H_5$, and ${}^3H_6$ emission transitions, respectively. The RT spectrum is dominated by a broad band extending from 225 to 350 nm and

centered at around 275 nm. The tail observed at longer wavelengths (300-350 nm) probably indicates the presence of another emission overlapping with the dominant band, which is consistent with the availability of two distinct crystallographic sites for Pr^{3+} in the RT trigonal phase [6, 7, 14]. We would like also to highlight the presence of a very weak emission coming from the 4f→4f transitions, which is not visible in Figure 6.3b. This is due to the fact that the allowed 5d→4f emission significantly dominates over the forbidden 4f→4f, and the chosen scale on the Y axis precludes the observation of these very weak lines. The features regarding the behavior of the 4f→4f emission of Pr^{3+} in the present host will be discussed later in the text.

Since in $K_3Lu(PO_4)_2$ the dopant ions substitute only for the Lu^{3+} ions, the changes observed in the excitation and emission bands of Pr^{3+} when the system undergoes the phase transition from the trigonal to the monoclinic structure have to be linked with the crystal structure transformation of $K_3Lu(PO_4)_2$ and, consequently, to the local Lu^{3+} coordination and symmetry changes. As a matter of fact, the energy of the $4f^15d^1 \rightarrow 4f^2$ emission band strongly depends on both the covalency effect and the crystal field strength induced by the ligands. For an increasing covalency, the interaction between the electrons is reduced, since they spread out over wider orbitals. As a result, the 5d electron levels of Pr^{3+} shift to lower energy. This is known as the nephelauxetic effect [17]. The earlier investigations on the $K_3Lu(PO_4)_2$:Pr^{3+} system performed by Trevisani *et al*. [7] revealed that the average Lu-O bond length decreases when crystal structure changes from monoclinic to trigonal, since the coordination number decreases from 7 to 6. Thus, the red shift of the Pr^{3+} 5d→4f emission band observed with increasing temperature from 8 K to RT is linked to a possible increase of the covalency of the Lu-O (Pr-O) bonds moving from the LT phase (monoclinic) to the RT one (trigonal). Alternatively, when moving from coordination number 7 (LT) to coordination number 6 (RT) the Pr-O distances are reduced, so the crystal field splits more the 5d state of Pr^{3+} and a red shift is observed.

The evolution of the photoluminescence emission and decay time of Pr^{3+} has been studied in the range 8-500 K to gain insight into the temperature-dependent phase transitions. The position and the profile of the 5d→4f emission band become significantly different when increasing the

temperature (Figure 6.4); it is possible to identify three main regions: (i) In the temperature range 8-150 K both the profile and the position of the Pr^{3+} 5d→4f emission band do not change; (ii) in the range 150-250 K the profile of Pr^{3+} 5d→4f emission band remains unchanged, but the band slightly shifts towards lower energy; (iii) above 250 K both the band profile and its position change.

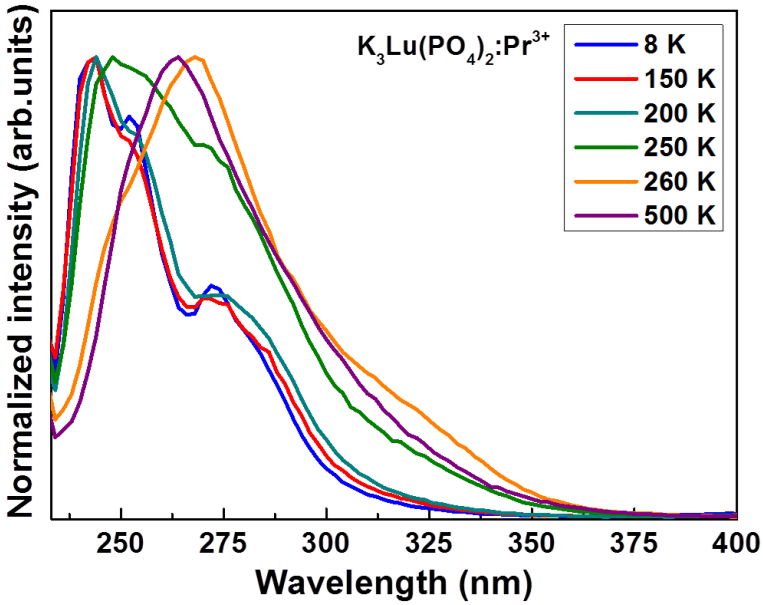

Fig. 6.4. Normalized emission spectra of $K_3Lu(PO_4)_2$: Pr^{3+} upon excitation at 220 nm as a function of temperature.

The decay curves for the 5d→4f emission transition have been studied upon intra-center excitation at 220 nm in the temperature range 8-500 K. Selected curves are presented in Figure 6.5. The curves have been recorded at the emission wavelengths corresponding to two different phases, *i.e.*, at λ_{em} = 244 nm in the monoclinic low temperature phase at 8 K (Figure 6.5a), and at λ_{em} = 268 nm in the trigonal phase at 500 K (Figure 6.5b).

All the decay curves show single exponential character, thus they can be fitted to a single exponential function according to the following expression:

$$I = I_0 \exp(-t/\tau) + B \qquad (6.1)$$

where I is the luminescence intensity, I_0 is the intensity at 0 ns, t is the time, τ is decay time, and B is the time independent background intensity.

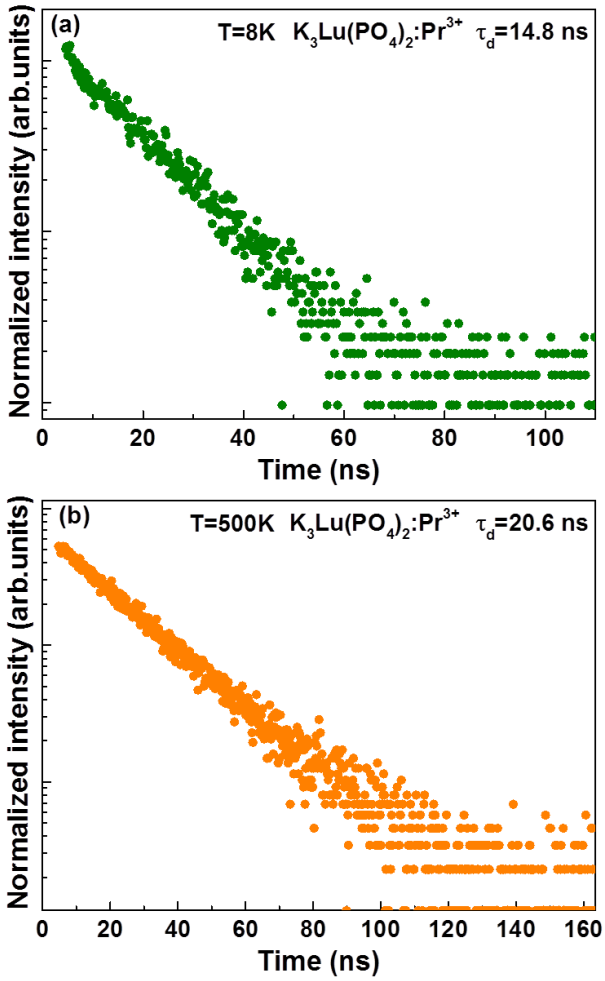

Fig. 6.5. Figure (a) presents the 5d→4f decay curve of Pr^{3+} luminescence in the monoclinic phase recorded at λ_{em}=244 nm upon excitation at 220 nm. Figure (b) presents the 5d→4f decay curve of Pr^{3+} luminescence in the trigonal phase recorded at λ_{em}=268 nm upon excitation at 220 nm.

The decay time for the 268 nm emission at 500 K (trigonal phase) is about 20.6 ns, whilst for the 244 nm emission at 8 K (monoclinic phase) is about 14.8 ns. In Figure 6.6 the value of the decay constant is plotted as a function of temperature. Up to 140 K (region A) the decay constant remains almost unchanged, with values around 14.8 ns. With increasing temperature,

the decay times slightly increase (region B), and above 260 K (region C) become significantly longer, with values about 20 ns. These changes are in good agreement with the previously observed red shift of the emission band (Figure 6.3), since it can be derived that for a given emission transition the decay time (τ) is proportional to the third power of the emission wavelength (λ): $\tau \sim \lambda^3$ [18].

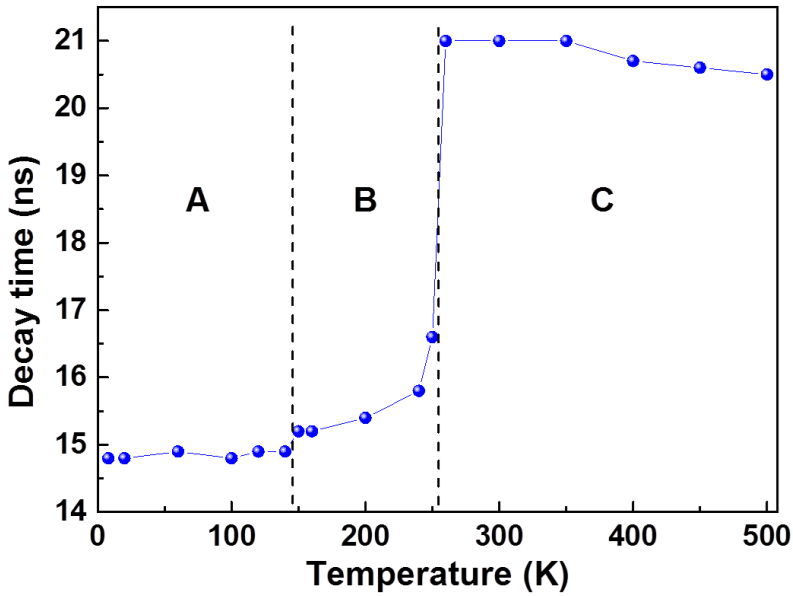

Fig. 6.6. Temperature dependence of the photoluminescence decay time of Pr^{3+} (5d→4f) emission in $K_3Lu(PO_4)_2$. Region A indicates the monoclinic phase in which Pr^{3+} ion retains seven fold coordination (λ_{em}=244 nm, λ_{ex}=220 nm). Region B indicates the monoclinic phase in which Pr^{3+} ion retains six fold coordination (λ_{em}=248 nm, λ_{ex}=220 nm). Region C indicates the trigonal phase (λ_{em}=268 nm, λ_{ex}=220 nm). Vertical lines and dash-line are only guides to the eye.

6.3.2.2 $K_3Lu_{1-x}Y_x(PO_4)_2:Pr^{3+}$

Figure 6.7a shows the normalized excitation spectra of the $K_3Lu_{1-x}Y_x(PO_4)_2:Pr^{3+}$ family recorded at room temperature for emissions at 280 nm (for x = 0-0.5) and 270 nm (x = 0.75-1), corresponding to the 5d→4f transition of Pr^{3+}. The spectra present a broad band centered in the far ultraviolet spectral region, assigned to the strong 4f→5d spin-allowed absorption transition, which corresponds to transitions to the lowest energy

5d level of the five crystal field components. It is possible to observe that increasing the Y concentration from 0% to 100% causes a change in the shape and a blue shift of the excitation band.

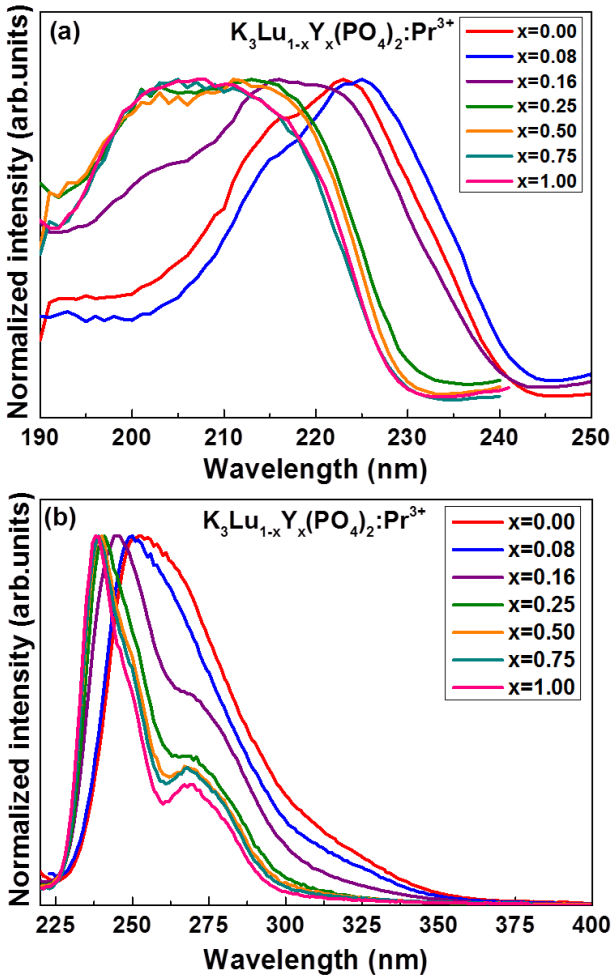

Fig. 6.7. Normalized spectra of the Pr^{3+} emission in $K_3Lu_{1-x}Y_x(PO_4)_2$ recorded at RT. (a) Excitation spectra were measured at λ_{em}=280 and λ_{em}=270 nm for x=0-0.5 and x=0.75-1 powders, respectively, and (b) emission spectra upon excitation at λ_{ex}=205 nm and λ_{ex}=192 nm for x=0-0.08 and x=0.16-1samples, respectively.

Figure 6.7b presents the emission spectra of the $K_3Lu_{1-x}Y_x(PO_4)_2:Pr^{3+}$ samples, recorded upon excitation into the 4f→5d absorption band of Pr^{3+} at 205 nm for x = 0-0.08, and at 192 nm for x = 0.16-1. As expected, for the pure Lu and slightly Y co-doped (x = 0.08) samples, the profile of the

emission band corresponds to the one observed for Pr^{3+} in the pure trigonal phase, with its maximum at about 255/260 nm. In the heavily doped Y samples, however, the spectra show a broad band in the near UV with four peaks that correspond with transitions from the 5d excited state into the $^3H_4$, $^3H_5$, $^3H_6$ and $^3F_3$ 4f multiplets. As observed for the excitation, increasing of Y content induces a blue shift on the bands originating from the 5d level. In the case of $K_3Lu_{0.84}Y_{0.16}(PO_4)_2:Pr^{3+}$, both the emission band of the pure trigonal samples and the monoclinic ones are observed, in agreement with the presence of a mixture of the two phases.

The room temperature decay curves for the 5d→4f emission of Pr^{3+} in the $K_3Lu_{1-x}Y_x(PO_4)_2:Pr^{3+}$ powders were recorded for all the samples except $K_3Y(PO_4)_2:Pr^{3+}$, since for this sample the intensity was too low. As observed previously for the case of $K_3Lu(PO_4)_2:Pr^{3+}$, all the curves were well fitted by a single exponential function. The obtained values for the decay constants are presented in Table 6.1. It is possible to observe that the effect in the decay times of changing the Y/Lu ratio in the solid solution is analogous to changing temperature in the $K_3Lu(PO_4)_2:Pr^{3+}$powders: in the monoclinic phase (high yttrium content) decay time is about 14-15 ns, for the sample with a mixture of phases (x = 0.16) is about 16 ns, and for the pure trigonal samples (low or zero yttrium content) the decay time is about 21 ns. These results are also in good agreement with the observed shift in the emission band (Figure 6.7b).

Table 6.1

Decay data for the 5d→4f emission of Pr^{3+} in the $K_3Lu_{1-x}Y_x(PO_4)_2:Pr^{3+}$ powders upon UV excitation (215-225 nm).

Host	λ_{exc} (nm)	λ_{emi} (nm)	Decay time (ns)
$K_3Lu(PO_4)_2$	225	273	20.8
$K_3Lu_{0.92}Y_{0.08}(PO_4)_2$	227	272	20.9
$K_3Lu_{0.84}Y_{0.16}(PO_4)_2$	220	270	16.1
$K_3Lu_{0.75}Y_{0.25}(PO_4)_2$	218	246	14.8
$K_3Lu_{0.50}Y_{0.50}(PO_4)_2$	219	240	14.2
$K_3Lu_{0.25}Y_{0.75}(PO_4)_2$	215	241	13.7

The blue shift observed when increasing the Y content and the differences in the decay time values, can be explained in the same way that

the effects observed when lowering the temperature below 140 K in the case of $K_3Lu(PO_4)_2:Pr^{3+}$: the coordination number changes from 6 to 7 as a consequence of the substitution of Lu by Y, and the distance between oxygen atoms and Pr^{3+} ions increases. Consequently, the crystal field splits less the 5d state of Pr^{3+} and a blue shift is observed. Alternatively, substitution of Lu by Y reduces the covalency of the Pr-O bonds, since the increase of the coordination number gives rise to a bond lengthening [19].

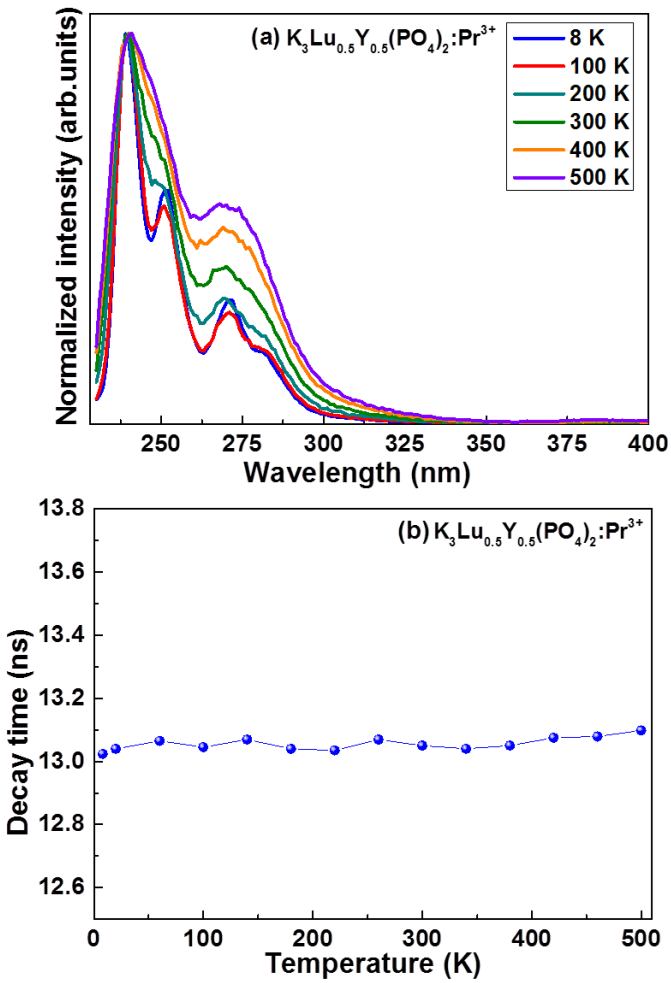

Fig. 6.8. Temperature dependence in the range 8 to 500 K of the luminescence properties of $K_3Lu_{0.5}Y_{0.5}(PO_4)_2:Pr^{3+}$. (a) Normalized emission spectra upon excitation at 210 nm. (b) Decay times of the Pr^{3+} emission at 240 nm upon excitation at 210 nm.

In conclusion, the high energy shift of the 5d energy level of Pr^{3+} (that causes the blue shift of the Pr^{3+} emission) can be obtained both by increasing the Y content in $K_3Lu_{1-x}Y_x(PO_4)_2:Pr^{3+}$ or cooling down in $K_3Lu(PO_4)_2:Pr^{3+}$.

The temperature evolution of luminescence intensity and decay time of Pr^{3+} in $K_3Lu_{0.5}Y_{0.5}(PO_4)_2$ has been also studied in the 8-500 K range. The results confirm that the Y co-doping stabilizes the monoclinic phase up to, at least, 500 K, since the profile and position of the maxima of the 5d→4f bands remain unchanged (Figure 6.8a), the decay curves are single exponential and the decay constant remains unchanged in the temperature range of study (Figure 6.8b).

It is also worth noticing the high quenching temperature for the 5d→4f Pr^{3+} emission in $K_3Lu_{1-x}Y_x(PO_4)_2$, which is caused by the small Stokes shift of the Pr^{3+} emission in these hosts.

6.3.3 4f→4f transitions

Upon excitation at 200 nm (into the 4f→5d absorption band) in the monoclinic phase a very weak 4f→4f emission band of Pr^{3+} has been observed. Generally, for a given temperature, there are two main factors that govern the occurrence (or absence) of the Pr^{3+} $4f^15d^1 \rightarrow 4f^2$ interconfigurational emission transition: (i) the energy location of the first (lowest energy) $4f^2 \rightarrow 4f^15d^1$ excitation transition; and (ii) the Stokes shift of the emission. In solids where the first Pr^{3+} $4f^2 \rightarrow 4f^15d^1$ excitation transition occurs at relatively low energy and the Stokes shift of the emission is large, the non-radiative $4f^15d^1 \rightarrow 4f^2$ relaxation can compete with the $4f^15d^1 \rightarrow 4f^2$ radiative relaxation [20]. In such materials, the emission is usually dominated by the Pr^{3+} intraconfigurational transitions (4f→4f sharp lines), but it can also be a mixture of inter- and intraconfigurational emission transitions. In a single configurational coordinate model, the low energy position and large offset of the $4f^15d^1$ level results in the crossing with the $^3P_{0,\,1,\,2}$ / $^1I_6$ levels and with the $^3H_4$ ground level, with a lower activation energy, increasing the rate of the non-radiative $4f^15d^1 \rightarrow 4f^2$ relaxation [14]. According to the model for Pr^{3+} emission proposed by Srivastava *et al*. [14], the 5d→4f emission dominates over the 4f→4f one when the Stokes shift is

lower than ~ 3200 cm^{-1}. In a previous work on Pr^{3+} doped $K_3Lu(PO_4)_2$, Trevisani *et al*. [7] reported that the Stokes shift for the Pr^{3+} 5d→4f emission in the trigonal phase (RT) is around 2800 cm^{-1}. It is clear from Figure 6.7 that the Stokes shift for Pr^{3+} emission does not change significantly when the content of Y increases. Furthermore, the 5d→4f emission dominates over the 4f→4f one thus, according to Srivastava's model, makes possible to conclude that the value of the Stokes shift in these materials is smaller than ~ 3200 cm^{-1}.

To illustrate the case, the room temperature emission spectra for $K_3Lu_{0.5}Y_{0.5}(PO_4)_2$ and $K_3Y(PO_4)_2$ upon 200 nm excitation are presented in Figure 6.9. Two broad emission bands centered at around 385 and 485 nm are observed as well as the characteristic narrow lines of the 4f→4f transitions of Pr^{3+} between 580 and 630 nm. The origin of the weak 4f→4f emission in the orange-red range is clear: the observed lines at 593 nm, 603 nm and 615 nm belong to the $^1D_2 \rightarrow {}^3H_4$, $^3P_1 \rightarrow {}^3H_6$ and $^3P_0 \rightarrow {}^3H_6$ emission transitions, respectively.

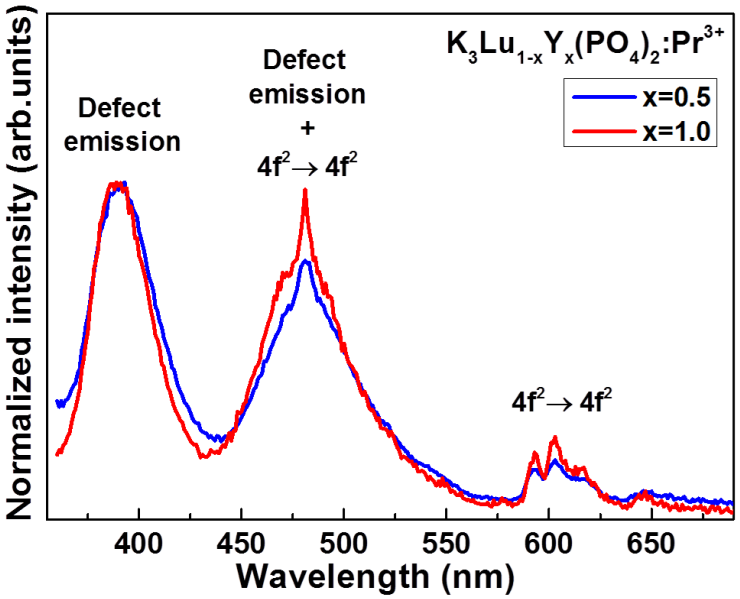

Fig. 6.9. Normalized spectra of Pr^{3+} emission in $K_3Lu_{0.5}Y_{0.5}(PO_4)_2$ and $K_3Y(PO_4)_2$ recorded at RT upon excitation at 200 nm.

On the contrary, the nature of the emission band centered at around 385 nm is unknown. Nevertheless, based on previous reports on Pr^{3+}-doped $Sr_3La(PO_4)_3$ and $Ba_3Lu(PO_4)_3$ [4], this band can be assigned to an emission from a defect. The origin of the second broad band in the 440-560 nm spectral range is also not clear. However, its profile and position can suggest that this band arises from the overlapping of a defect emission and the $^3P_1 \rightarrow {}^3H_4$ and $^3P_0 \rightarrow {}^3H_4$ emission transitions. Furthermore, this defect related emission can feed the ^3P_J / $^1I_6$ energy levels causing the emission from ^3P_J and $^1D_2$ observed in Fig 10. This latter hypothesis is supported by the radioluminescence spectra, which is presented in Figure 6.10.

6.3.4. Radioluminescence

The radioluminescence spectra presented on Figure 6.10 were measured along with the reference BGOP ($Bi_4Ge_3O_{12}$ in powder form) and the spectra are mutually comparable in an absolute way. All spectra show intense Pr^{3+} 5d→4f emission in the 240-350 nm spectral region, defect related emission bands centered around 385 and 485 nm, and less intense 4f→4f emission bands at around 485 and 605 nm. Both the position of the 5d→4f emission maxima and the band shape are affected by the phase of the host lattice. The two compounds that present trigonal structure at RT (*i.e.* $K_3Lu(PO_4)_2$, and $K_3Y_{0.08}Lu_{0.92}(PO_4)_2$) show an intense band located at around 300 nm with two and one clear maxima, respectively. All the others (monoclinic at RT) present two peaks, with maxima located at 245 and 280 nm. $K_3Y_{0.16}Lu_{0.84}(PO_4)_2$ shows also a shoulder around 320 nm, that is almost the same wavelength in which the two trigonal compounds have one of their maxima. This emission most probably comes from the Pr^{3+} ions in the trigonal phase, in view of the fact that this compound consist of the mixture of both trigonal and monoclinic phases, as it has been discussed above in the text. A different shape and low energy shift of the radioluminescence spectra in comparison to that for photoluminescence is noticeable, and occurs typically for the 5d→4f luminescence transition (Pr^{3+}, Ce^{3+}) in situations where a non-negligible concentration of somehow perturbed sites of these ions is present [21,22]. However, to better understand such effect further investigations are needed. By increasing yttrium concentration the 4f→4f emission intensity of Pr^{3+} is substantially increased, while the 5d→4f emission intensity is reduced, although this effect does not seem to be

totally linear with the increase of yttrium concentration. In the extreme case (*i.e.* $K_3Y(PO_4)_2$) both de 4f→4f and 4f→5d transition bands present almost the same intensity.

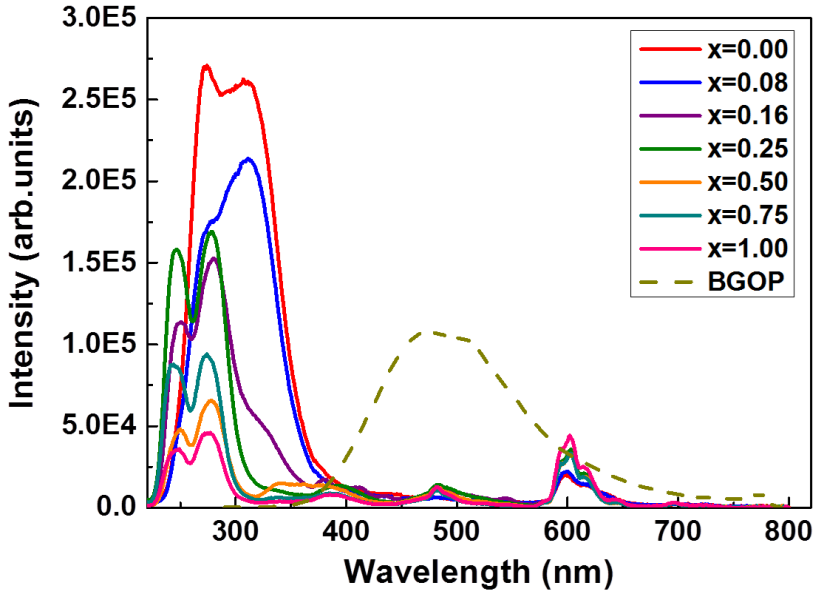

Fig. **6.10.** Radioluminescence spectra of $K_3Lu_{1-x}Y_x(PO_4)_2:Pr^{3+}$ (x=0, 0.08, 0.16, 0.25, 0.5, 0.75, 1) (X-ray excitation 40 kV, 15 mA, RT). Standard BGOP spectrum is also included as a reference.

There is a noticeable difference in the emission spectra depending if the excitation is into the Pr^{3+} $4f^2 \rightarrow 4f^15d^1$ transition band (λ_{ex} = 205 or 192 nm, see Figure 6.7b), or into the host lattice absorption band (X-ray, see Figure 6.10): upon X-ray excitation the 4f→4f emission in the 580-630 nm spectral range is more intense than upon direct excitation into the 4f→5d absorption transition band of Pr^{3+}. This behavior points out that the host lattice defects can easily capture the excitation energy, which is efficiently transferred to the Pr^{3+} ^3P_J / $^1I_6$ energy levels due to the spectral overlap, as it is discuss above, which explains the relatively intense bands of the 4f→4f intraconfigurational transitions in the radioluminescence spectra. It has been reported that in many systems the fast Pr^{3+} $4f^15d^1 \rightarrow 4f^2$ transition, which dominates the emission spectrum upon direct $4f^2 \rightarrow 4f^15d^1$ excitation, is quenched in favor of the slow Pr^{3+} 4f→4f transition upon excitation with X-ray or γ-ray. Illustrative examples include Pr^{3+} activated $LuCl_3$ [23], $LuBr_3$ [24], $SrCl_2$ and $BaCl_2$ [25]. It is also clear that the capture of electrons and

holes by Pr^{3+} becomes progressively less efficient with increasing the content of Y in the $K_3Lu_{1-x}Y_x(PO_4)_2$ solid solution. Furthermore, with increasing Y content, the 4f→4f emission becomes more intense. This observation can be explained as follows: when substituting Lu by Y (which is larger), the distortion of the host lattice becomes greater, increasing the content of the defects in the host lattice. As a consequence, the defect-related broad emission bands (centered at 385 and 485 nm) become more intense.

6.4. Conclusions

In this chapter several materials belonging to the $K_3Lu_{1-x}Y_x(PO_4)_2$ (x = 0, 0.08, 0.16, 0.25, 0.50, 0.75 and 1) family activated with 1% of Pr^{3+} have been studied in detail. All samples were synthesized by a solid state reaction at high temperature and their luminescence properties at RT (all the samples) and in the 8-500 K temperature range (only $K_3Lu(PO_4)_2$ and $K_3Lu_{0.50}Y_{0.50}(PO_4)_2$) have been investigated. The pure Lu and the slightly Y co-doped samples exist at RT in the trigonal phase, whilst heavily Y co-doped samples show stable monoclinic phase at 300 K. The monoclinic phase can be obtained increasing the Y^{3+} ion content (Y/Lu above 0.19) in the solid solution, but also by reducing the temperature below 250 K in the case of $K_3Lu(PO_4)_2$ sample. The emission is dominated by the Pr^{3+} $4f^15d^1 \rightarrow 4f^2$ interconfigurational transitions when excited directly into the $4f^15d^1$ band. Upon X-ray excitation, the $4f^15d^1 \rightarrow 4f^2$ and 4f→4f emission intensities progressively decrease and increase, respectively, when Y concentration is increased. This behavior is explained in terms of the favorable overlap between the defect-related luminescence of the host lattice and the Pr^{3+} 4f→4f interconfigurational transitions. The 5d→4f emission features are strongly related to the local environment of the Pr^{3+} ion. A significant red shift of the emission has been observed when the Pr^{3+} ion changes its location; in particular from one site with coordination number of 7 (monoclinic symmetry) to two sites with coordination number of 6 (trigonal symmetry). This can be explained in terms of the changes in the crystal field splitting of the 5d energy levels of Pr^{3+} and/or the changes of the covalency. Moreover, there is no thermal quenching of the Pr^{3+} luminescence up to 500 K.

References

[1] C. Ronda, J. Gondek, E. Goirand, T. Jüstel, M. Bettinelli, A. Meijerink, *Mater. Res. Soc. Symp. Proc.* 1111 (2009) 1111-D08-01.

[2] M. Korzhik, A. Fedorov, A. Annenkov, A. Borissevitch, A. Dossovitski, O.Missevitch, P. Lecoq, *Nucl. Instrum. & Meth. A.* 571 (2007) 122.

[3] C. W. E. van Eijk, P. Dorenbos, R. Visser, *IEEE Trans. Nucl. Sci*. 41(1994) 738.

[4] K. Ivanovskikh, A. Meijerink, C. Ronda, F. Piccinelli, A. Speghini, M. Bettinelli, *Opt. Mater*. 34 (2011) 419-423.

[5] L. Schwarz, B. Finke, M. Kloss, A. Rohmann, U. Sasum, D. Haberland, *J. Lumin.* 72-74 (1997) 257-259.

[6] D. Wisniewski, A. J. Wojtowicz, W. Drozdowski, J. M. Farmer, L. A. Boatner, *J. Alloys Compd*. 380 (2004) 191-195.

[7] M. Trevisani, K. V. Ivanovskikh, F. Piccinelli, M. Bettinelli, *J. Lum.* 152 (2014) 2-6.

[8] J. M. Farmer, L. Boatner, B. C. Chakoumakos, C. J. Rawn, D. Mandrus, R. Jin, J. C. Bryan, *J. Alloys Comp*. 588 (2014) 182-189.

[9] A. C. Larson and R. B. Von Dreele, *General Structure Analysis System (GSAS)*, Los Alamos National Laboratory Report LAUR (2004) 86-748.

[10] B. H. Toby, *J. Appl. Crystallogr*. 34 (2001) 210-213.

[11] M. Vlasse, C. Parent, R. Salmon, G. Le Flem, P. Hagenmuller, *J. Solid State Chem*. 35 (1980) 318-324.

[12] A. Matraszek, I. Szczygiel, *J. Therm. Anal. Calor*. 93 (2008) 689-692.

[13] L.N. Komissarova, M.G. Zhizhin, A.A. Filaretov, *Russ. Chem. Rev*. 71 (2002) 619-650.

[14] A. M. Srivastava, M. Jennings, J. Collins, *Opt. Mat*. 34 (2012) 1347-1352.

[15] V. A. Efremov, P. P. Melnikov, L. N. Komissarova, *Phase Transit*. 38 (1992) 127.

[16] Lazoryak, B. ICDD Grant-in-Aid (1998).

[17] G. Blasse, B. C. Grabmaier, *Luminescent Materials*, first ed., Springer-Verlag Berlin Heidelberg, 1994.

[18] A. Zych, M. de Lange, C. de Mello Donega, A. Meijerink, *J. Appl. Phys*. 112 (2012) 013536.

[19] F. Cotton, G. Wilkinson, *Advanced Inorganic Chemistry*, third ed., John Wiley & Sons Inc., New York, 1972.

[20] A.J. de Vries, G. Blasse, *Mater. Res. Bull*. 21 (1986) 683-694.

[21] L. Havlak, V. Jary, M. Nikl, P. Bohacek, J. Barta, *Acta Mater*. 59 (2011) 6219-6227.

[22] C. Pedrini, B. Moinet, J. C. Gacon, B. Jacquier, *J. Phys. Cond. Matter* 4 (1992) 5461-5470.

[23] A. M. Srivastava, U. Happek, P. Schmidt, *Opt. Mater*. 31 (2008) 213-217.

[24] A. M. Srivastava, J. S. Vartuli, S. J. Duclos, P. A. Schmidt, S. B. Chaney, U. Happek, *IEEE Trans. Nucl. Sci*. 56 (2009) 986-988.

[25] A. Zych, A. Leferink, K. Van Der Eerden, C. Donega De Mello, A. Meijerink, *J. Alloys Compos*. 509 (2011) 4445-4451.

Chapter 7

Concluding remarks

Luminescent materials are fundamental in many technological fields. For this reason, deep understanding of their properties and the phenomena involved in them is required for the developing of new better materials, which is crucial for improving applications and devices in many areas. In particular, systems based on energy transfer processes (from host-to-ion and in pairs of ions) attract a lot of interest due to their technological relevance.

The aim of this thesis was the study of various oxide-based materials doped with different trivalent lanthanide ions. Specific, various types of silicates doped with Tb^{3+} and Eu^{3+} ions, and various kinds of phosphates doped with Pr^{3+} were synthesized and analysed from the structural and the spectroscopic point of view. Their luminescence properties were carefully analysed in order to test their potential application as phosphors or fast scintillators.

It has been found that the presence or absence of Tb^{3+}-Tb^{3+} and Tb^{3+}-Eu^{3+} energy transfer processes in $Ca_3Tb_{2-x}Eu_xSi_3O_{12}$ and $Ca_3M_{2-x-y}Tb_xEu_ySi_3O_{12}$ (M = Gd, Y) determines the emission colour of the materials. The resulting colour can be effectively changed by modifying the doping levels and controlling the concentration ratio between the two ions. Moreover, it has been confirmed that the emission of Eu^{3+} can be enhanced by using Tb^{3+} as a sensitizer when the Tb^{3+} concentration is high enough to allow fast energy migration among terbium ions.

The low values of absorption of these materials prevent to considering them as potential systems for the developing of WLEDs, but their study has revealed interesting properties that can help in the comprehension of other compounds more competitive from a technological perspective.

In the case of $Ca_9M(PO_4)_7$:Pr^{3+} (M = Al, Lu) it has been observed that the Pr^{3+} optical properties are quite insensitive to the nature of the M cation, but depend on the dopant concentration. In particular, the interplay between

the $^1D_2 \rightarrow {}^3H_4$ and $^3P_0 \rightarrow {}^3H_4$ emissions is strongly affected by different non-radiative processes that depend on the Pr^{3+} concentration.

For the $K_3Lu_{1-x}Y_x(PO_4)_2:Pr^{3+}$ solid solution, the host-to-Pr^{3+} energy transfer is strongly related to the Y-content, since the 5d→4f features of Pr^{3+} are heavily affected by the surroundings. In the present case, a significant red shift of the emission is observed when the surroundings of Pr^{3+} are changed. This change is caused by the increasing of yttrium concentration in the solid solution that stabilizes the monoclinic phase at room temperature. Upon UV excitation into the $4f^15d^1$ band, emission is dominated by the interconfigurational transitions, whereas upon X-ray excitation the 4f→4f emission band becomes more intense as the Y-content is increased as a result of the favourable overlap between the defect-related emission of the host and the 4f→4f transitions.

Acknowledgments

I would like to thank the European Commission for funding through the Marie Curie Initial Training network LUMINET, grant agreement No. 316906.

There are some people I would like to personally thank:

My supervisor Prof. Marco Bettinelli, for giving me the opportunity of perform my PhD in his lab, for all the helpful discussions, his advice and his support. I would like to sincerely thank him for giving me the opportunity of undertake my studies in the frame of a Marie Curie project, with all the research, educational and scientific possibilities that this kind of projects provide.

My laboratory colleagues, especially Prof. Fabio Piccinelli and Erica Viviani, for all the help and the advice provided during these years, and for their patience when training me in new experimental techniques. I would like to stress my grateful to Fabio for performing the Rietveld refinement on the samples under study.

Dr. Martin Nikl (Dept. Optical Materials, Institute of Physics AS CR in Prague), for his hospitality and for providing me the opportunity of working in his lab during my secondment for the ITN-LUMINET project. Dr. Karol Bartosiewicz for all his experimental help and support during my stay in Prague, and also for our interesting scientific discussions and collaboration then and after.

Prof. Marco Kirm (Dept. of Physics, University of Tartu), for his hospitality and for giving me the opportunity of working in his lab during my secondment for the ITN-LUMINET project. Dr. Vitali Nagirnyi and Ivo Romet for all their help and supervision in the laboratory and Viktoriia Levushkina for her tips and support during my stay in Tartu.